BRNO UNIVERSITY OF TECHNOLOGY
VYSOKÉ UČENÍ TECHNICKÉ V BRNĚ

FACULTY OF CHEMISTRY
FAKULTA CHEMICKÁ

INSTITUTE OF MATERIALS SCIENCE
ÚSTAV CHEMIE MATERIÁLŮ

FUNCTIONAL FOAMS WITH DENSIT YGRADIENT
FUNKČNÍ PĚNY S GRADIENTEM HUSTOTY

MASTER'S THESIS
DIPLOMOVÁ PRÁCE

AUTHOR — **Bc. Juraj Svatík**
AUTOR PRÁCE

SUPERVISOR — **prof. RNDr. Josef Jančář, CSc.**
VEDOUCÍ PRÁCE

BRNO 2019

BRNO FACULTY UNIVERSITY OF CHEMISTRY OF TECHNOLOGY

Master's Thesis Assignment

Number of thesis:	FCH-DIP1389/2018	Academic year: 2018/19
Institute:	Institute of Materials Science	
Student:	**Bc. Juraj Svatík**	
Study programme:	Chemistry, Technology and Properties of Materials	
Study field:	Chemistry, Technology and Properties of Materials	
Head of thesis:	**prof. RNDr. Josef Jančář, CSc.**	

Title of Master's Thesis:

Functional foams with densit ygradient

Master's Thesis assignment:

The main goal of the Thesis is to prepare polymer foams with closed cells and prescribed porosity gradient mimicking nature materials such as bamboo exhibiting balance of high stiffness and fracture toughness at low density.

Deadline for Master's Thesis delivery: 10. 5. 2019

Master's Thesis is necessary to deliver to a secretary of institute in the number of copies defined by the dean. This assignment is part of Master's Thesis.

- - - - - - - - - - - - - - - -	- - - - - - - - - - - - - - - -	- - - - - - - - - - - - - - - -
Bc. Juraj Svatík	prof. RNDr. Josef Jančář, CSc.	doc. Ing. František Šoukal, Ph.D.
Student	Head of thesis	Head of institute

In Brno, 31. 1. 2019

- - - - - - - - - - - - - - - -
prof. Ing. Martin Weiter, Ph.D.
Dean

ABSTRACT

Inspired by lightweight natural materials, cellular materials with gradient porosity are expected to possess mechanical properties superior to conventional polymer foams due to their specific structural architecture. These properties could allow use of the lightweight materials in structural components. In this thesis, preparation of the gradient cellular materials is investigated employing the laminating and/or 3D printing. Static and dynamic mechanical tests were performed on both quasi homogenous and gradient porosity foams providing experimental support for the hypothesis of structural architecture driven deformation response. Experimental data were interpreted using existing theoretical models. Our results led to a conclusion that the existing theoretical models derived for regularly structured foams are not valid for foams with gradient porosity exhibiting mechanical properties substantially better than the foams with homogenous porosity.

ABSTRAKT

Vycházíme-li z lehčených přírodních materiálů, lze od porézních materiálů s gradientem porozity očekávat mechanické vlastnosti nadřazené konvenčním polymerním pěnám, a to díky jejich specifické architektuře. Tyto vlastnosti umožňují použití lehčených materiálů jako strukturních prvků. V této práci je popsaná příprava gradientních porézních materiálů pomocí laminování a/nebo 3D tisku. Provedeny byly statické a dynamické mechanické testy na obou kvazi homogenních a gradientně porézních pěnách poskytující experimentální podklad pro hypotézu deformační odezvy plynoucí ze strukturní architektury. Data se dále interpretovala užitím zavedených teoretických modelů. Naše výsledky vedly k závěru, že tyto teoretické modely odvozené od pěn s pravidelnou strukturou není vhodné aplikovat pro pěny s gradientem porozity, protože prokazují podstatně lepší mechanické vlastnosti než homogenně porézní pěny.

KEY WORDS

Functional foams, functionally graded foams, porosity gradient, PMMA, 3D printing

KLÍČOVÁ SLOVA

Funkční pěny, funkční gradientní pěny, gradient porozity, PMMA, 3D tisk

CITATION

SVATÍK, Juraj. *Funkční pěny s gradientem hustoty* [online]. Brno, 2019 [cit. 2019-05-08]. Dostupné z: https://www.vutbr.cz/studenti/zav-prace/detail/112884. Diplomová práce. Vysoké učení technické v Brně, Fakulta chemická, Ústav chemie materiálů. Vedoucí práce Josef Jančář.

DECLARATION

I declare that the diploma thesis has been worked out by myself and that all the quotations from the used literary sources are accurate and complete. The content of the diploma thesis is the property of the Faculty of Chemistry of Brno University of Technology and all commercial uses are allowed only if approved by both the supervisor and the dean of the Faculty of Chemistry, BUT.

……..

student´s signature

ACKNOWLEDGMENT

Here, I would like to thank my supervisor of the diploma thesis prof. RNDr. Josef Jančar, CSc. for his advices and leadership in my work. I would like to thank my consultant Ing. Klára Zárybnická for her supervising, advices and help in laboratory as well as with writing of the thesis. Also, I would like to thank my colleagues in the office, especially for help from Ing. Marek Zbončák, PhD. with mechanical tests measurements and for help from Ing. Petr Lepcio, PhD. with printing of 3D samples. For the design of the density gradient 3D structures, I would like to thank Ing. Přemysl Menčík and Mgr. Radek Přikryl, PhD. At last, my thanks belong to my friends and family for their support and help.

CONTENT

1 INTRODUCTION

Porous materials are intensively investigated for multiple reasons [1; 2; 3; 4]. At first, scientists were fascinated by cellular materials in nature, such as wood, cork or structure of the bamboo stem. These natural materials are still widely used, in plywood or in oriented strand boards, cork as bung for wine bottles and bamboo as scaffolding mainly in Asian countries. However, man-made porous materials play also an important role in our everyday life, too. They can be found in energy management, vibration suppression, sound absorption, heat insulation, fluid filtration or as mechanically protecting packaging. Due to their low-density, utilization of these materials brings also economic benefits [5].

Utilization of advanced cellular materials is the focus of current research focusing on engineering the pore structure more precisely to enhance their mechanical properties and introduce novel function. There are proofs that pore size and shape, number of pores and most recently porosity gradient have significant impact on mechanical performance of these materials. Wall material selection is often less important than the structural architecture of the cellular material. Widespread polymeric based foams include foamed polystyrene, polyethylene, polyurethane or recently developed biodegradable polymers contributing to the reduction of the environmental impact of packaging. Functional polymer-based foams are also envisioned in advanced application as mobile hydrogen storage, in chemical and mechanical sensors or EMI shielding. The selection of the type of polymer is very important when the cellular material is intended for biological applications, due to the required biocompatibility and at least partial resorbability.

At the end of the 20th century, there were discovered the metal-organic frameworks (MOFs), which possess the advantage of forming regular porous structure via fundamental building blocks in a bottom-up manner. Over time, MOFs were developed so much, that nowadays they are used as high-efficiency storage units, separators with extremely high selectivity and catalytic activity.

With the need for new functional lightweight materials, new techniques are also needed for the production and fabrication of parts out of them. Basic foaming techniques using physical or chemical blowing agents do not offer any control over the number, size, connectivity or spatial organisation of pores. Therefore, new technologies were developed, where gradient structures are produced with techniques like layer-by-layer casting or various 3D printing techniques with great promise for the future lightweight cellular materials [6; 7; 8; 9; 5; 10].

2 THEORETICAL PART

2.1 Polymeric foams

Polymeric foams are essentially porous materials consisting of solid phase, in our case polymer, and gas phase with a specific cellular structure. In principle, any polymer material can be foamed, however polystyrene, polypropylene, polyethylene and polyurethane are the most frequently utilized. Multiple variables can be used to sort polymeric foams, however, the type of matrix and the connectivity of pores are the two primary ones. The difference between thermoplastic and thermosetting foams originates from the different nature of the wall material. Similarly to solid polymers, thermosets are hard to recycle by re-using them since their structure is held together by covalent intermolecular bonds. Another way to sort polymer foams is to divide them to rigid and flexible depending on their cell structure. Open cell foam structure provides pores or cells, which are connected throughout the material, thus permeable for fluid and, thus, are flexible. On the other hand, closed cell foam structure, where pores are roughly spherical and separated from each other, provides rigid and non-permeable foams. Applications of those two types of foams are quite wide – bedding, car seats or packaging are served by the flexible open cell foams and the rigid closed cell foams are suitable for insulating materials (Fig. 1:) or small shock protection [11; 12]. Polymer foams can be also divided according to the size of the cells as macrocellular (>100 μm), microcellular (1–100 μm), ultramicrocellular (0,1–1 μm) and nanocellular (0,1–100 nm) [13].

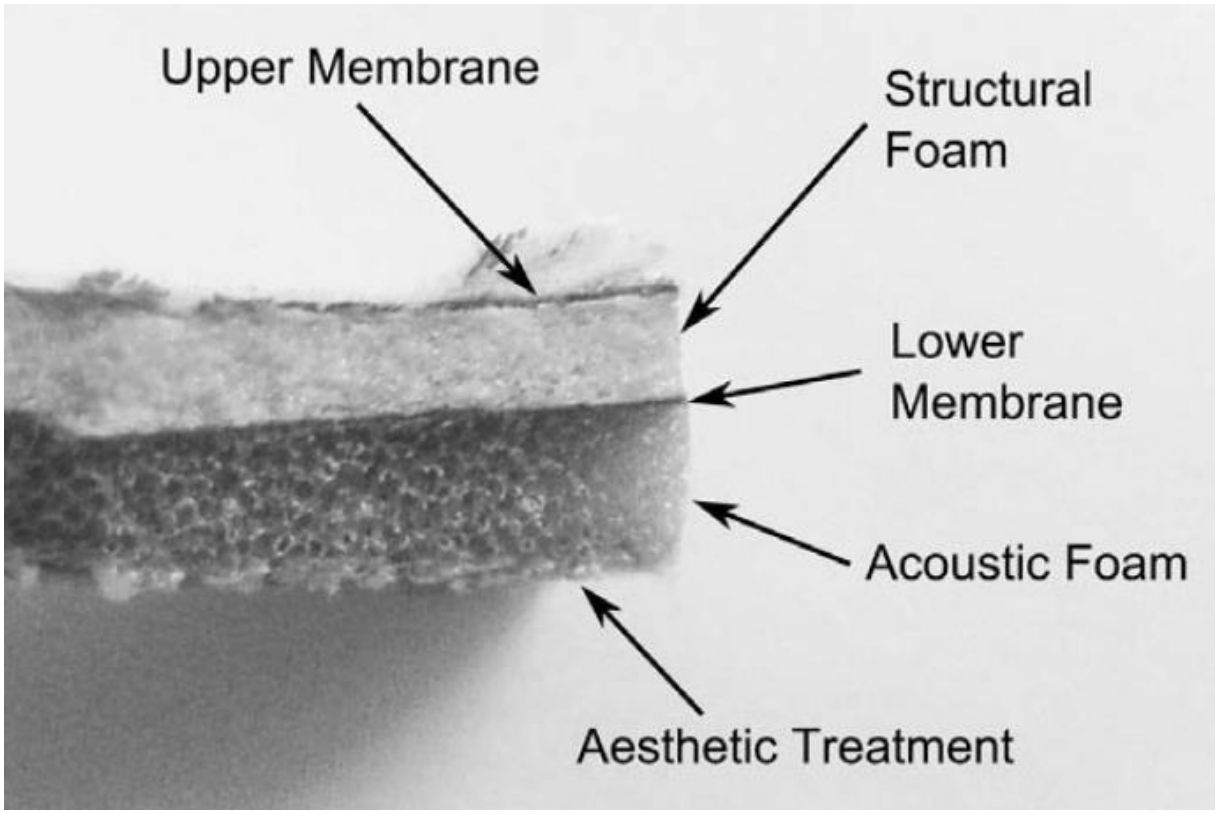

Fig. 1: Photograph of a layered polymer foam consisting of foams with different cellular structure laminated for excellent sound insulation [14]

2.2 Blowing agents

Blowing agent is usually a low molecular weight substance producing gas upon thermal degradation resulting in forming bubbles in the molten solid polymer. The blowing agents are selected to control the foam structure considering the actual foaming process used for the given polymer and/or the

intended product. Ways of introducing blowing agents into a matrix are either physical (PBA) or chemical (CBA). Baking soda is the simplest chemical blowing agent producing CO_2 upon thermal decomposition while super critical CO_2 is the most favourable physical blowing agent due to its environmentally benign effect.

CBA is used when a cellular structure is created by a chemical reaction and the required heat is produced/supplied during the plasticization process. Most common gases produced upon thermal decomposition of blowing agents are CO_2 and N_2. Gas diffusion rate is slow and gas expansion is rapid and robust. CBA can be divided according to the sign of the reaction enthalpy producing the blowing gas into exothermic or endothermic. Exothermic CBA releases heat while producing the gas further increasing temperature of the foamed system resulting in larger cells. Typical representative of this group is azodicarbonamide, which creates nitrogen and ammonia during the thermal decomposition. Endothermic CBA needs heat for releasing the gas causing cooling the system and making larger number of smaller cells. The structure is usually better, gas diffusion rate is rapid and gas expansion is controlled (slower). Among typical representatives belong sodium carbonate [15; 16; 17].

2.3 Foaming process

Generally, formation of porous polymer structure is controlled by cell nucleation and growth of bubbles in polymer. The foaming process for typical polymer consists of several steps (Fig. 2:):

- preparation of molten polymer
- dissolution of a physical/chemical blowing agent in molten polymer under elevated pressure
- nucleation of bubbles upon reducing the pressure to the ambient pressure
- growth of nucleated bubbles in the polymer until their equilibrium size

A control of the foaming process is required as further properties of the foam are determined in this step. Density of foam depends on the amount of released foaming (CBA) or gas dissolved in the polymer matrix (PBA), the depressurization rate and losses of the gas to the ambient environment. The size of cells and their connectivity and spatial distribution are influenced by the kinetics of cell nucleation, bubble growth kinetics after nucleation and the coalescence of growing cells during their expansion.

When investigating the foaming process using PBA, such as SC-CO_2 various steps have to be considered. Creating a single-phase supersaturated solution is achieved by high-pressure dissolution of the gas in a polymer controlled mainly by pressure and temperature. Next, formation of pores requires evolution of thermodynamic instability in the polymer/gas solution by lowering the solubility with reducing pressure or temperature. Bubble formation requires presence of critical nucleus, which is defined by a minimum radius for the bubble to grow. That is controlled by the increase in the free energy of the system, when small bubbles are created, causing instability between the bubbles and the surrounding environment. Thus, nucleated cells with size smaller than the critical nucleus will collapse, while the bigger ones will grow.

Critical issues of cells growth include *cell coarsening* as the process, when larger bubbles grow at the expense of smaller bubbles resulting in formation of one big bubble reducing cell-population density. This phenomenon is usually caused by higher gas pressure in smaller bubbles. *Cell coalescence* occurs in a foaming polymer melt, when two adjacent growing cells combine in one big cell, because of the cell wall rupture. This process is favoured, since it reduces the total free energy as the adjacent cells coalesce, however, leads to reduced cell-population density, again. The weak melt strength of molten polymer is the main reason of cell wall rupture, thus processing temperature, which have a great impact on the strength of the molten polymer, is kept as low as possible. *Cell collapse* is caused by escape of the blowing gas into the surrounding atmosphere instead of expanding

the growing cells. This can occur when SC-CO_2 is used as the blowing agent, since the diffused gas can be released in the atmosphere and the minimum free energy of the polymer/gas system is reached by phase separation. This results in very low foam expansion and can be prevented by proper temperature control to obtain foams with high expansion ratio.

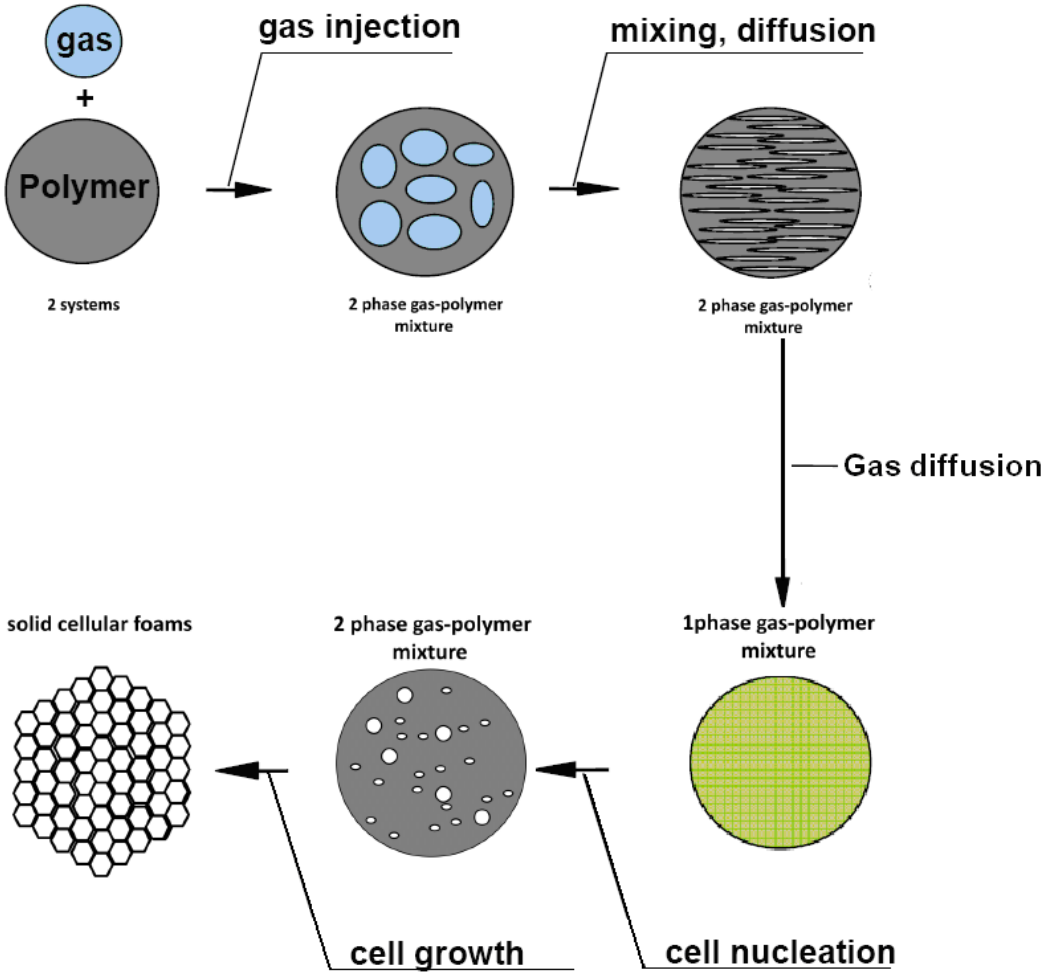

Fig. 2: Scheme of typical general foaming process with physical blowing agent used [18]

The last step of cell growth by a diffusion of dissolved gas into growing bubbles, is governed by the time allowed the cells to growth prior foam solidification, temperature and pressure regime of the process. Also, diffusion rate and rheology of the polymer/gas solution influence the bubbles growth rate [19].

The process of bubble formation creates several mechanical stresses, which can be divided into static and dynamic stresses. The static stresses include surface tension and gravitational stresses and do not need fluid motion to originate. Very important contribution is the surface tension (γ):

$$\sigma_y = \Delta p = 2\gamma \cdot \kappa \tag{1}$$

Equation (1) is called Young-Laplace law, where normal stress (σ_y) and pressure drop (Δp) across a curved surface of mean curvature (κ) are caused by surface tension. Another important contribution involves hydrostatic pressure difference (p_H), where buoyance force (F_B) rises on a bubble with certain volume (V_B) and significantly affect bubble detachment and compaction:

$$F_B = \Delta p_H g V_B \tag{2}$$

Among the dynamic stress contributions, tangential viscous stress (σ_v) is of importance depending on the deformation rate of the fluid (dU/dL) and the fluid viscosity (η_L). It arises from the viscous shear flow at the interface and is described by an approximation expressed in the form:

$$\sigma_v = \eta_L \cdot \frac{U}{L} \tag{3}$$

where U is the characteristic flow velocity and L is the characteristic length scale of the flow. However, two viscous contributions are present, because one is from gas and the other one from liquid phase. Other contributions to interfacial stresses may also arise from presence of stabilizing agents, which interfere with bubble generation [20].

2.4 Types of foams

Origin of foam

Basically, porous materials can be divided into two big groups – natural and artificial. Materials as wood, cork, bamboo stem or human bone (Fig. 3:) have very specific cellular structure, which is often mimicked in engineering artificial porous materials.

Honeycomb cellular materials with prismatic cells (hexagonal) like wood or cork or foam-like cellular materials with polyhedral cells like trabecular bone or plant stems are examples of microstructure found in natural materials. These materials can contain both solid and cellular components, for example human skull has a sandwich structure, where core is light, foam-like material surrounded by two outer layers of nearly compact material. Such structures can be also found in iris leaf, which provides an excellent resistance to bending and buckling. Widely studied feature of natural cellular materials is the gradient in density (or porosity). Such structure is possessed by bamboo plant, which increases the volume fraction of dense fibres radially towards the periphery and endows the unsurpassed balance between stiffness and strength of these materials. [5; 21]

Artificial foams mimicking natural materials and fabricated by using current advanced technologies attempt to improve mechanical, insulation or electromagnetic shielding properties, etc. Various foam types exist like polymer nanocomposites foams [13], syntactic foams [22] or foams with a porosity gradient [10].

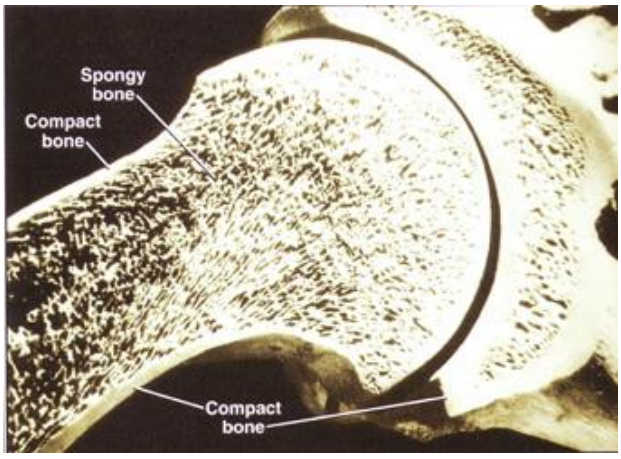

Fig. 3: Structure of bone where skin is compact, and the core is porous [23]

Thermoset foams

There is a variety of thermoset foams with polyurethane (PUR) being used the most. PUR foams are made by reacting polyols and diisocyanates (Fig. 4:) in the presence water. By the reaction of hydroxyl groups with diisocyanates urethane cross-linking bonds are made and the reaction of isocyanate groups with water releases carbon dioxide, which acts as the blowing agent. Linear or less

branched polyesters of adipic acid and diethylene glycole are used for production of soft foams. These foams are more elastic and resistant against hydrolysis than polyester-made foams but undergo oxidation easily. Hard foams are prepared using bigger amount of isocyanate component and hydroxyl component is heavily branched. Usually diphenyl methane diisocyanate is used providing higher tenacity to the product. Densities of soft and hard foams differ essentially, usually 15–70 $kg \cdot m^{-3}$ for soft and 10–600 $kg \cdot m^{-3}$ for hard foams.

Specialty PUR foams include so called integral foams (Fig. 5:), where the core is porous, and the edge/outer layer is compact. The density of the product increases from the core to the edges and fluor-trichlormethane is used as a blowing agent. Production of this structure is by heating of the mould and by creating the temperature gradient between mould and inward of the foam, the thickness of the skin can be controlled – the lower the temperature of the mould, the thicker is the skin. Skin-core structure in case of rigid polymer provides good flexural properties at low overall densities, so wide application can be found as structural materials. Other advantages are low thermal conductivity and ease of processing.

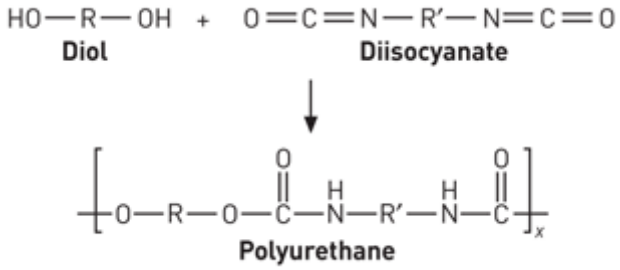

Fig. 4: Reaction of diol and diisocyanate forming polyurethane [24]

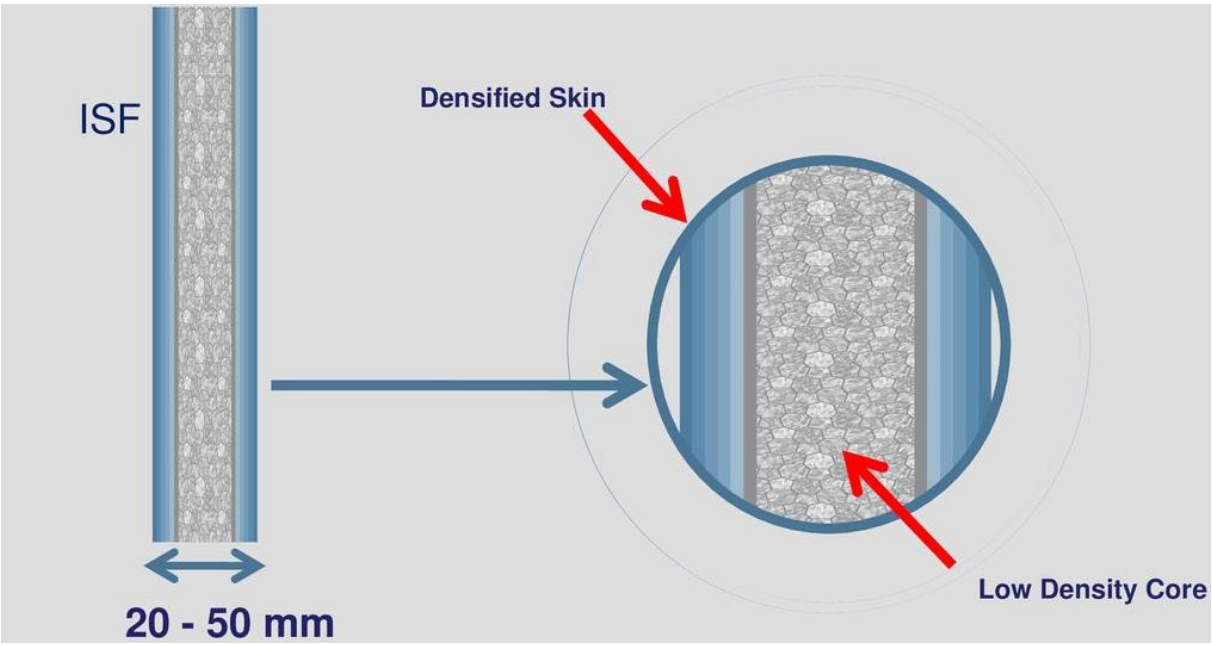

Fig. 5: Scheme of structure of integral PUR foam [25]

Soft PUR foams are used for laminating of textile, packaging, in automotive industry, furniture or isolating tapes. Hard foams are mostly used for thermal or sound insulation (refrigerators, construction industry, isolation of pipes, etc.) and for levelling voids. Integral foams are used in automotive industry for bumpers, in furniture and for soles of ladies shoes [26; 27].

Thermoplastic foams

Thermoplastic polymers possess the advantage of simpler processability and recyclability. Polystyrene foams are the most frequently utilized, they are discussed first, and, later, PMMA foams are reviewed in a separate section as they are part of experiment in this thesis. Polyethylene and polypropylene foams possess similar features as the PS foams.

Polystyrene (PS) is one of the most important commodity polymers. Expanded PS (EPS) is made by polymerization in presence of volatile aliphatic hydrocarbons (mostly pentane), which are soluble in polymer and high pressure is needed due to low boiling points of hydrocarbons. EPS is supplied in the form of beads. The final products are made by foaming the beads in closed moulds. Regularly, the process consists of three stages: prefoaming, aging and foaming in moulds giving it the shape of the desired product. EPS density is usually in the range from 15 to 50 $kg \cdot m^{-3}$ and this foam exhibits very good thermal insulating properties. Mechanical properties of EPS are proportional to the density. Sound and mechanical damping properties are also affected primarily by the geometry of the molded part, less by the bead size and processing conditions. Temperature changes in the range from –-17 °C to 43 °C do not affect performance of EPS. Dimensional stability performed by EPS is exceptional and remain unaffected within a wide range of ambient factors, less than 2 %. Mechanical properties should not be affected by moisture and EPS is essentially waterproof [27; 28].

PMMA foams

Several studies were investigating PMMA foams, most probably because it is one of the most promising polymers to obtain nanocellular structure. It was proven that the pore size has a strong impact on the macroscopic physical properties of polymer foams, and this was further demonstrated by developing nanoporous polymer foams exhibiting unexpected physical properties. More specifically, PMMA nanoporous foam showed higher elasticity modulus, impact strength and improved hardness in comparison with microporous structure of PMMA foam with similar densities [29]. Also, increased thermal insulation properties were observed due to the Knudsen effect of nanosized pores. Knudsen diffusion occurs, when the pore diameter is smaller than the mean free path of the diffusing gas, so the gas molecules collide more often with the pore walls than with each other. For PMMA nanoporous foams considering pores filled with air is the mean free path about 70 nm and the air thermal conductivity is significantly decreased. These advantages increased interest in production of lightweight material with nanosized porous structure with mainly carbon dioxide, used as the preferred blowing agent. It offers not only easy processability and absence of chemical residues, but an environmentally friendly way of using CO_2.

Difficult task of producing nanocellular foams with appropriate dimensions resides in the thermodynamics of the foaming process. The interfacial (surface) area increases as nanocells are created causing increase of the interfacial (surface) free energy. High cell nucleation densities (above 10^{14} cells/cm^3) were achieved by adding nanosilica particles or by using block copolymers – blends of PMMA and [poly(methyl methacrylate)-block poly(butyl acrylate)-block poly(methyl methacrylate)] [30]. Introducing nanoparticles in the foam structure creates problem with their dispersion, but otherwise this approach seems suitable. This problem was solved with an “in-situ synthesis of NPs”, where the NPs are directly synthesized in a hosting polymeric matrix and formation of NPs aggregation is prevented. Usually dispersed precursor is converted to NPs by thermal treatment, laser irradiation or sol-gel reactions [30].

2.4.1 Open and closed cell foams

Open cell foams possess interconnected pores and are usually considered open cell, when more than half of its pores are opened. Unique property of some of the open cell foams is their shape memory enabling return to their original shape after compression due to free air movement and chemical makeup. On the other hand, closed cell foams are characterized by sealed pores preventing flow of

water or gases. Typical representatives of the open cell foams are open cell polyurethane, polyester, polyamide and closed cell foams are EPDM, neoprene, PVC/NBR [32; 33]. Size, shape and spatial organisation of pores significantly influences mechanical behaviour of the foam by controlling deformation process prevailing in foam [34]. These phenomena are discussed further in chapter 2.5. Morphology of open and closed cell foams is depicted in Fig. 6:.

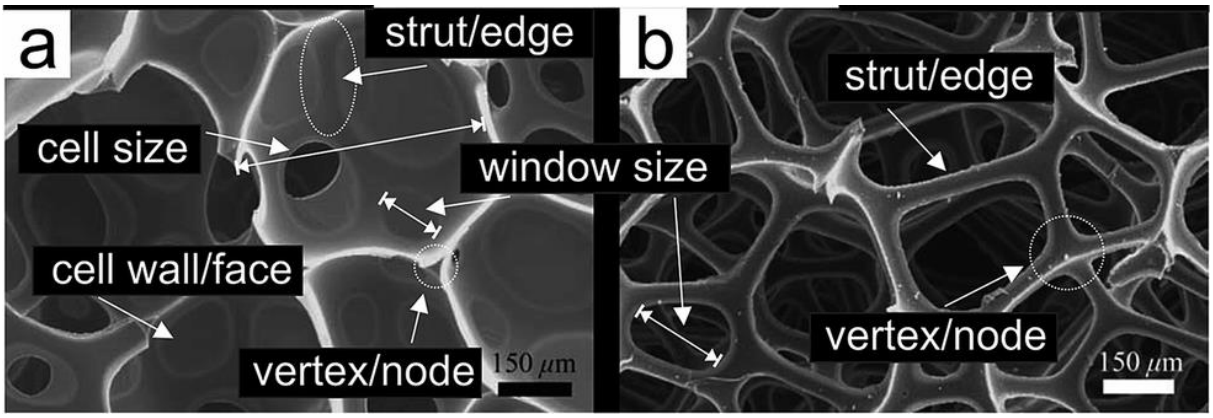

Fig. 6: Pore morphology of polymer with opened-cell (a) and closed-cell (b) structure, both structures are made of polyurethane; SEM [31]

2.4.2 Functionally graded/gradient foams

Recently, functionally graded materials were introduced as a new category of engineered materials in which the unique porosity and possibly composition structure is created in a way resulting in gradually changing properties of such material [4]. For functionally graded foams (FGFs), it is suggested that pores coordinated in a hierarchical manner should exhibit improved properties. Various sizes of pores secure different properties, such as macropores decrease diffusion distance, mesopores provide transport pathways with a minimized resistance and micropores possess the dominant absorption sites for guest species. Thus, precise distribution and structure of these pores could result in synergistic effect and that is the main reason for focusing on the design and synthesis of hierarchical porous polymers [6].

Literature differentiates between gradient and graded material, where microstructure and properties are designed to change continuously and step-wise, respectively. The advantage of these materials rests in tailoring of desired properties by morphological or compositional variations. These materials are used mainly as biomaterials for use in cell cultivation scaffolds. Many porous biomaterials fabricated so far had homogenous structure (uniform pore size distribution, uniform porosity distribution, mechanical properties), but introducing porosity distribution could result in unexpected mechanical or biological properties (table 1) [10].

FGFs have also been considered for utilization in automotive industry enhancing crashworthiness applications. Gupta and Cui. et al. both presented functionally graded foams and experimentally confirmed that they can improve the energy absorption over conventional foams. In further experiments, they found out that stress wave propagation and plastic dissipation are determined by the type of the gradient function. To find the best FGFs structure, it is necessary to investigate its properties in comparison with conventional foams and seek the best foam gradient [35].

Table 1: Some examples of graded/gradient porous materials used in medicine for various applications [10]

Biomaterial	**Potential application**
Graded porous Ti	Permanent skeletal replacement implants with minimized stress shielding
Gradient porous Ti	Dental implants with osteointegration
Graded porous hydroxyapatite	Mechanical strength and cell/tissue ingrowth
Compositionally graded porous collagen on PLGA-collagen	Osteochondral tissue engineering

2.4.2.1 Syntactic foams

Different approach to create porous structure is used in syntactic foams, where the cells are created by hollow glass microspheres dispersed in a matrix. Polymer, metal or ceramic matrices are used; however, thermosetting polymers are most frequently used. Syntactic foams are widely studied due to their excellent compressive and high strain rate properties. They possess large stress-plateau in their compressive stress representing their energy absorption characteristics, which is getting larger with lower density of foam balanced by the reduced strength (Fig. 7:). Recently, new studies were published on functionally graded syntactic structures, where volume fraction gradient of hollow spheres is created along one dimension of the material structure. However, non-uniform stress distribution in the material caused by changes in volume fraction of hollow microspheres can result in catastrophic failure in the matrix rich volume. There is also a gradient in the coefficient of thermal expansion and moisture absorption resulting in uneven thermal expansion causing internal stresses to develop. Radius ratio is defined as the fundamental structural parameter of hollow sphere:

$$\eta = \frac{r_i}{r_0} \tag{4}$$

where r_i is inner radius and r_0 is outer radius of the hollow sphere. Higher value represents thinner walls of the same size hollow spheres resulting in lower strength. On the contrary, linear increase in modulus and strength can be observed when η is decreased. Taking radius ratio in consideration, there can be created a gradient of η (Fig. 8:), whereas volume fraction of hollow spheres is kept unchanged and functionally graded structure is made and proved by measuring the densities of these foams [22; 36].

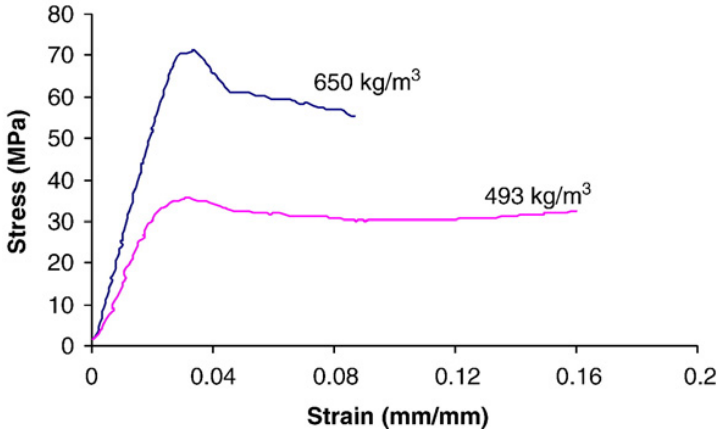

Fig. 7: Compressive stress-strain curve for syntactic foam with different densities, large stress-plateau and lower strength can be observed when lower density of syntactic foams is achieved [22]

Fly ash cenospheres are widely used as the filler in syntactic foams, because of their low cost. However, recovered from ash in the coal burning power plants, it is necessary to remove impurities and isolate only low-density intact particles. Alumina, silica, or silicon carbide are also used as hollow particles with high specific surface area providing better interfacial bonding with the matrix material. Availability of these particles is now in wide range of sizes, from nanometers to several milimeters [37].

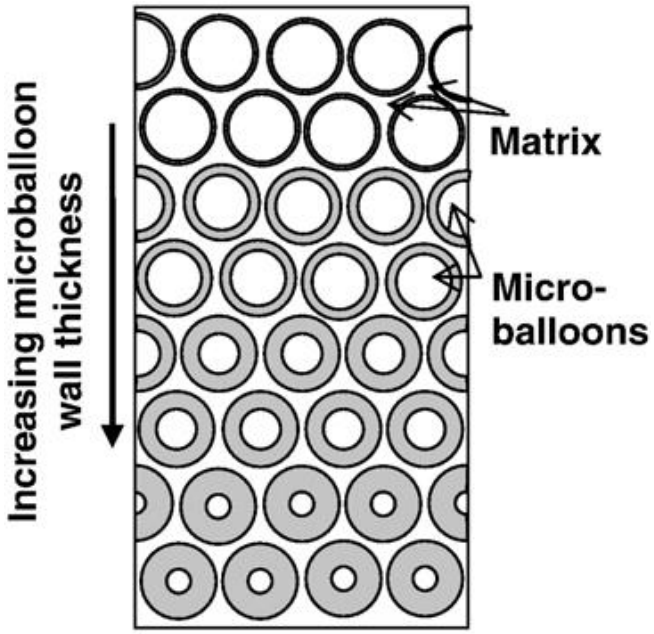

Fig. 8: Functionally graded structure of syntactic foam; gradient in radius ratio can be observed [22]

Early applications of syntactic foams included marine and aerospace structures, too. Thermal insulation applications in oil and gas industry were achieved thanks to the high-volume fraction porosity. Dimensional stability and low coefficient of thermal expansion at high temperatures allow their use in electronic packaging, composite tooling or thermoforming plug assists [38].

2.4.2.2 Sandwich structures

Sandwich structure is widely spread providing excellent balance of stiffness, and strength low structural weight. It consists of two thin, stiff skins, so called face sheets, which carry the tensile and the compressive loading and light weight core, which separates the two face sheets and carries shear loading. Core and face sheets thickness will be of importance as it will determine the mechanical response. Increased moment of inertia of the cross section, caused by separated face sheets with porous core, secures perfect resistance to bending and buckling. Sandwich structure can be found in commercial aircrafts, where their low weight structure is a big advantage, and, also, in aerospace launch vehicles and satellite structures in interior as well as in exterior. Design of large structures use sandwich structure, like the Stockholm Globe Arena, or railway vehicles, where floor panels, partition walls and even whole wagons are made in such manner [39; 40]. However, sandwich structures were first observed in nature, for example bird skulls, where almost fully dense face sheets are separated by low-density core of trabecular bone or leaves of monocotyledon plants, like irises (Fig. 9:) and cattails, which have long, narrow leaves with parallel veins [5].

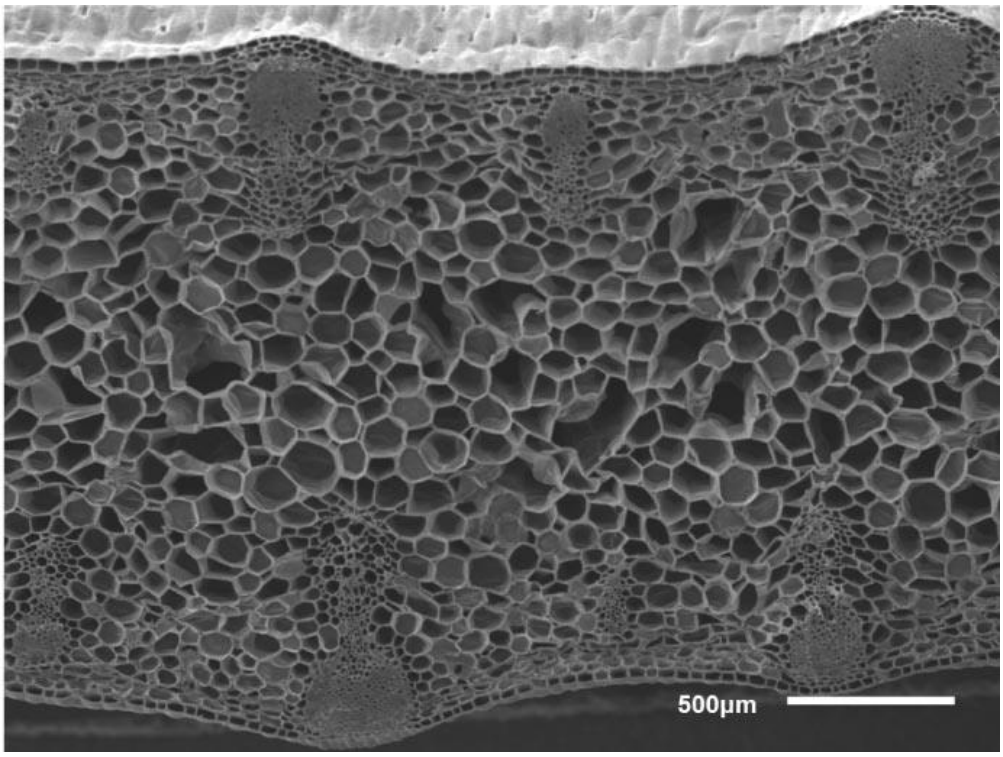

Fig. 9: Cross-section of iris leaf with sandwich structure; SEM [41]

2.4.2.3 Layer-by-layer structured foams

Some of interest was oriented on multilayer structures improving chemical, physical and mechanical properties in one direction depending on design. The functionally graded polyurethane foam was prepared using technique of sedimentation casting (layer-by-layer), where layers with various ratios of polyol/isocyanate groups were prepared and laminated from layer with least ratio to layer with highest ratio of polyol/isocyanate groups. It is necessary to maintain sufficient time between casting of layers, so the previous layer is passed its gel time and can keep its dimensions. The resulting structure is, however, discontinuous, because pronounced crossing between layers with different polyol/isocyanate ratio is observable (Fig. 10:).

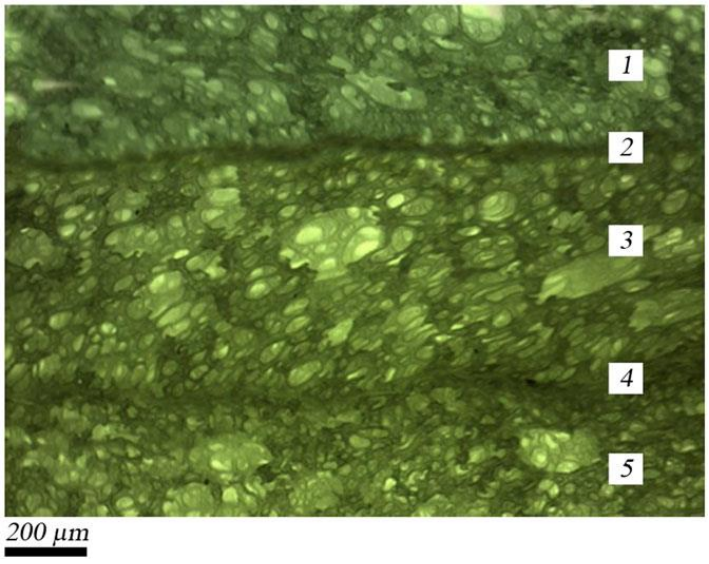

Fig. 10: Functionally graded structure of PUR foam prepared by sedimentation casting of layers with different polyol/isocyanate ratio; 1,3 and 5 are the layers, 2 and 4 are the crossings between the layers; OM [4]

Investigation of single layers and graded structure proved better properties of functionally graded PUR foam in certain areas. Compression test showed high strength and optimum flexibility, indentation force deflection test proved flexible surface and firmness configuration of functionally graded PUR foam and drop weight test showed better behaviour in energy absorption compared to single layers [4].

2.4.2.4 3D printed porous structure

Effective control of the pore size and geometry during the processing is desired, however, most of current techniques produce porous structures with random pore size and spatial distribution. The 3D printing technologies offer possibility to fabricate geometrically precise structures. Here, the main advantage is the possibility of controlling desired sizes, shape and location of pores [42]. However, the current 3D printing techniques have resolution limiting the geometric precision and utilization of dies with small diameter offering better resulting structure causes slow structure build-up rates.

3D printing enabled manufacturing of new protective structures for automotive industry or production of cost-effective parts in sports industry. Also, applications in medicine are possible – bioprinting of tissues and organs, manufacture of implants, prostheses or printing of scaffolds for initial cell attachment and tissue formation and for bone tissue engineering. The fused deposition modelling (FDM) technique is used with wide variety of materials, specifically thermoplastic polymers, such as polylactic acid or acrylonitrile butadiene styrene copolymers [43].

3D printing of foamed polymer using carbon dioxide has been attempted. The nozzle extruding liquid polymer generates bubbles of carbon dioxide, so the resulting structure is composed of polymer elements containing dispersed bubbles. However, the dispersion of bubbles in the wall material is not further controlled, so it is random [3].

Fabrication of quality polymer filaments for FDM is of great concern as they are precondition for quality of the printed parts. ABS and PLA are among polymers used the most for filament fabrication. PLA offers good mechanical strength and biodegradability, while obtained from renewable resources, whereas ABS possess high toughness and impact resistance [44].

2.4.3 Biodegradable foams

Increasing amount of waste and environmental problems are currently one of the main issues. At the same time, prices of plastics feed stock are increasing, too, and the crude oil is exhaustible raw

Fig. 11: Biodegradable PLA foam foamed with carbon dioxide suggested as replacement for PS foam in packaging material [48]

material, therefore, biodegradable foams made from renewable resources become the centre of research [45; 46; 47; 48]. Using of carbon dioxide as the environmentally friendly blowing agent is also emphasized.

Various materials were proposed for biodegradable foams, such as ethylene vinyl alcohol, polyvinyl alcohol, polycaprolactone, polylactic acid or starch. Starch is obtained from grains, corn or potatoes, and two different components, amylose and amylopectin, contribute to flexibility and foamability of the final product [49]. Polylactic acid extracted from corn or sugar-cane is very promising material for biodegradable foams, however, its low glass transition temperature restricts its usage in higher temperatures. PLA foamed with carbon dioxide is the desired candidate to replace PS foams as packaging material (Fig. 11:) [48].

2.5 Structure of foam

Honeycombs and foams (Fig. 12:) represent possible lightweight structures. Common honeycombs have prismatic uniform cells; thus, they are easier to investigate, and the insight gathered from these investigations can be applied to irregularly porous foams. The important structural parameter is the relative density defined as ratio of density of the cellular material (ρ_f) to the density of the solid material (ρ_s) from which the foam is made:

$$\rho^* = \frac{\rho_f}{\rho_s} \tag{5}$$

Mechanical behaviour also depends on the cell connectivity (Fig. 6:), size and shape distribution and on the geometrical anisotropy of the foam. Open-cell foams are formed by solid struts and closed-cell foams are formed by cell faces [5].

In general, the dependence of physical properties on the density of the material is given by Gibson and Ashby equation derived for either open or closed uniformly cellular structures:

$$P_f = C \cdot P_s \cdot (\rho^*)^n \tag{6}$$

In equation (6), P_f and P_s stand for the properties of a cellular material and the solid material, respectively, whereas C and n are constants, which can be obtained from experiments. However, C usually takes values around 1 and n between 1 and 2, but in the case of mechanical properties the value of n is typically 2 [30].

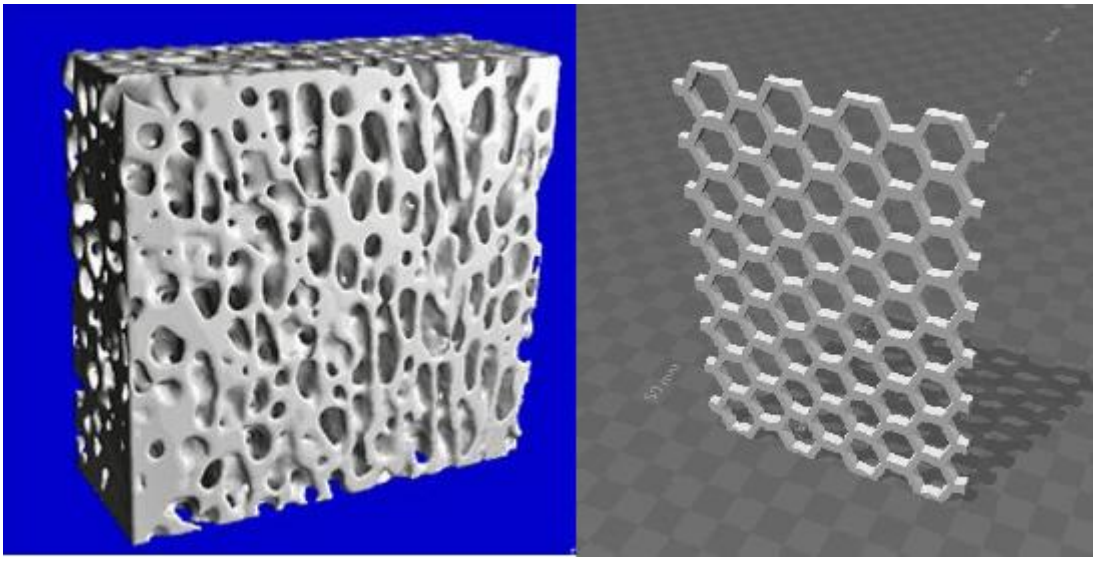

Fig. 12: Scheme of polyhedral structure in trabecular bone (left) [50] and 3D printed honeycomb structure (right) [51]

To improve foam performance, scientists focused on increasing the homogeneity of the cellular structure (narrow cell size distribution) and decreasing the average cell size of the foam. With this on mind, microcellular foams were developed where improved tensile and impact properties were found over conventional foams with bigger cell sizes for any given polymer. However, creating microcellular structure in polymeric foams with constant density and variable cell sizes was shown difficult to manufacture. Another important parameter determining foam structure and resulting mechanical properties are foaming conditions, such as foaming time, foaming temperature, etc. [30].

2.6 Deformation and failure of foams

There are several factors influencing mechanical properties, such as cell connectivity, material of wall and the cell geometry. Firstly, considering closed-cell structure, we must keep in mind that there will always be a fracture of open-cell pores. The fraction of open cells is a function of the relative density of the foam and this was proposed by Berlin and Shutov in 1980. Another important parameter influencing properties of porous materials coming from geometric structure were proposed [52]:

- cell size, shape or geometrical anisotropy
- cell wall thickness and distribution
- relative foam density
- relative number of open cells
- geometry of a foam cell

For open-cell foams at low relative densities the deformation process proceeds primarily by cell-wall bending. With increasing relative density ($\rho^* > 0{,}1$), the cell-wall compression and extension become more significant. When considering closed-cell foams, there need to be taken into account the cell faces, and the pressure of the fluid filling the cells. During the deformation, the cell edges bend and extend or contract, and the cell faces stretch, thus increasing the contribution of the axial cell-wall stiffness to the elastic moduli. The stiffness is also increased by the air compressed in the closed cells [34].

2.6.1 Deformation process

The process of deformation (Fig. 13:) and failure of foams considering cubic pores consists of edge bending, buckling and yielding. Precise description depends on the type of loading, and pore connectivity. The stress-strain curve in compression consist of a linear region (Hook´s law) at low deformations, followed by a long collapse plateau, where stress remains almost constant and finished with steep growth of stress caused by densification due to pore collapse. The Young´s modulus for open-cell foams is calculated as follows:

$$\frac{E^*}{E_s} = C_1 \cdot (\rho^*)^2 \tag{7}$$

where E_s is Young´s modulus of the wall, C_1 is constant obtained experimentally and ρ^* is relative density of the foam. For closed-cell foam stretching of the faces needs to be considered as it contributes to the mechanical response. The fraction of the solid in the edges (ϕ) is an important parameter as polymer is drawn away from the faces to the edges by surface tension during the processing, thus making faces thinner. Deformation process is also influenced by the gas or liquid captured in the closed pores. It is suggested that the gas in the pores and the polymer microstructure act synergically under deformation, thus, resulting in an additional stress. Then, the final equation for Young´s modulus of a closed-cell foams is in the form:

$$\frac{E^*}{E_s} = \phi^2 \cdot (\rho^*)^2 + (1-\phi) \cdot \rho^* + \frac{p_0 \cdot (1-2v^*)}{E_s \cdot (1-\rho^*)} \tag{8}$$

where p_0 is the initial pressure of the gas in the cell and ν^* is the Poisson´s ratio of the foam.

Mechanism of collapse of the cells depends also on the material of the cell walls. The plateau in the stress-strain curve is characterized by elastic buckling for elastomeric foams, and for elastoplastic foams, plastic deformation and formation of plastic hinges occurs.

In the point, where the cells almost collapsed, the densification occurs caused by compressing the cell walls into a solid. This process increases the density resulting in reduced strain [5; 34].

For open cell foams air-flow through the interconnected pores has to be accounted for. Deformation process, such as uniaxial compression, squeezes the air out of the pores and certain amount of work is done, because of the viscosity of the air. The amount of work is significantly dependent on the strain rate, as the faster the foam is compressed, the more amount of work is done. In literature, the contribution of air flow to the strength of a foam was investigated, too. It was found, that this contribution is proportional to the strain rate and to the viscosity of air and to the reciprocal of the cell size squared [34].

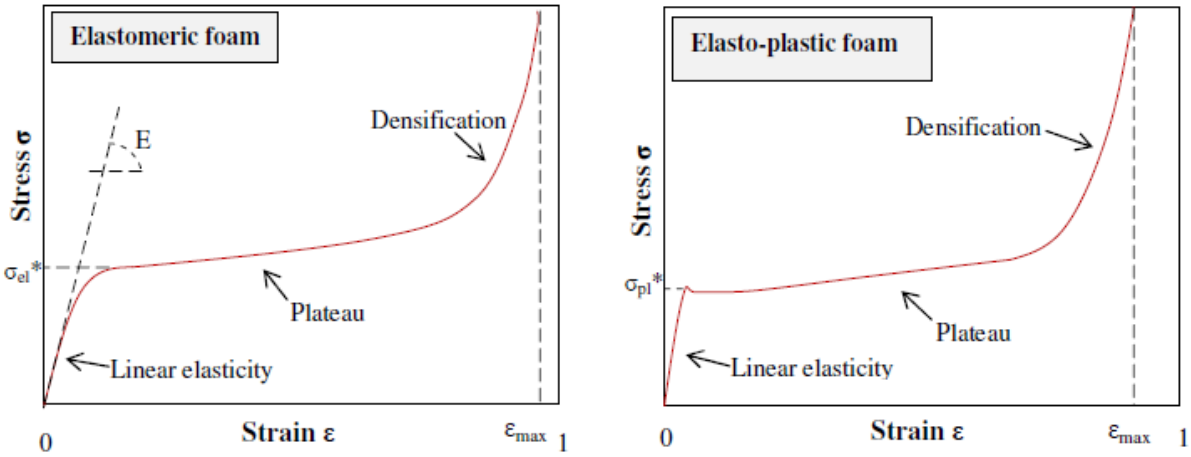

Fig. 13: Scheme of stress–strain curves in compression for elastomeric (left) and elastoplastic (right) foam [34]

2.6.2 Fracture toughness

Fracture toughness or the stress intensity factor K is very helpful parameter for determining the stress distribution around a crack. The fracture toughness is the function of applied load σ and crack size a according to the formula:

$$K = \sigma \cdot \sqrt{\pi \cdot a} \tag{9}$$

So, the K increases with increasing load and the failure occurs when the intensity of the applied stress at the crack tip reaches a critical value K_c. The critical value K_c is a constant for a particular material and defines the fracture toughness. It is also a function of the temperature, strain rate, the state of stress and the failure mode. The most investigated and frequent is mode I (Fig. 14:), which also occurs more often in real situations involving crack [53].

Interest in fracture toughness of foams rests in the weakening of the structure´s capacity of carrying load upon fracture. When foams are exposed to bending, the fracture occurs as the bending moment reaches the moment of fracture within the cell walls. At first, considering brittle foam with a crack at the edge, cell walls bend elastically, when they are loaded under tension and this process proceed with crack propagation as the force acting on the cell wall at the crack tip is big enough. For open-cell foams, fracture toughness (K_{IC}^*) is calculated using the following expression:

$$\frac{K_{IC}^{*}}{\sigma_{fs} \cdot \sqrt{\pi l}} = C_5 \cdot (\rho^{*})^{3/2} \tag{10}$$

where σ_{fs} is the modulus of rupture of the solid cell wall and l is the cell size. The assumption is for the crack length to be large compared to the cell size and for the rupture modulus to be constant [5].

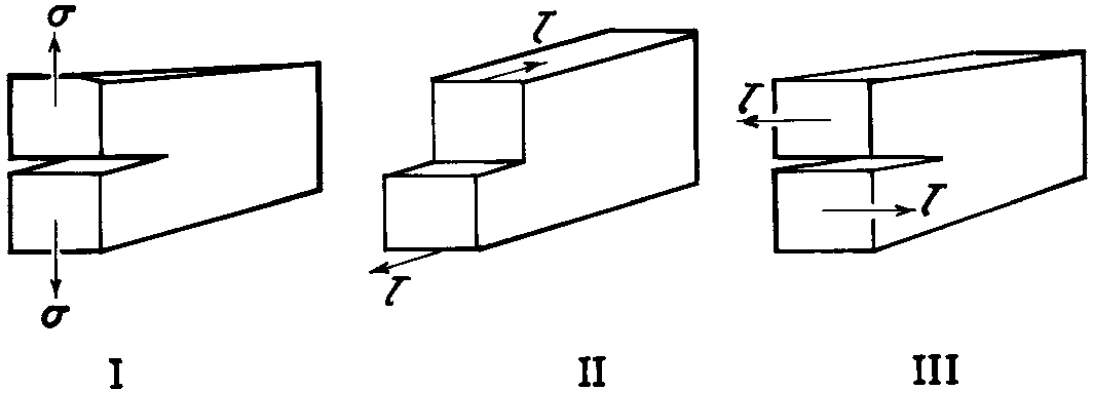

Fig. 14: Basic models of the failure – I is opening or tensile mode, II is sliding or in-plane shear mode, III is tearing or antiplane shear mode [53]

2.7 Foaming techniques

Some of possible routes for foaming were chosen and are described in this section. General foaming process is depicted in Fig. 2:.

2.7.1 Extrusion foaming

Extrusion process for foams was developed from plastic extrusion and is a fundamental foaming approach. It is an efficient method implemented with gas injection, mixing and cooling function. Extrusion foaming is also suitable for physical and chemical blowing agents.

Basic process includes mixing of blowing agent with a polymer melt under pressure, dissolving of the agent in the melt inside the barrel, cooling of the mixture as it approaches the die and nucleation of bubbles as the pressure drops abruptly at the die exit. The bubble growth continues until the cells are stabilized or ruptured. When using CBA, necessary requirements include high enough temperature of the melt to decompose blowing agent and high enough pressure in the barrel to keep the formed gas dissolved in the melt until exiting through the die [54; 18].

2.7.2 Foam injection moulding

The history of FIM goes back to 1950s, but this technology found its application later, when lower density product became interesting. Nowadays, foam injection moulding uses fully automated injection moulding machine with screw position control and increased injection volume. Specially designed screw in a plasticizing unit is the key part of the machine. The process is similar to extrusion foaming, when the gas is injected directly into the polymer melt in the form of super critical fluid and homogenously dispersed mixture is created. As certain pressure must be kept in the barrel to prevent premature expansion of the dissolved gas, also nonreturn valve and shut-off nozzle are present to block the melt at both ends [55]. The polymer/gas mixture is injected into the mould in a volume less than the amount required for a solid part. The pressure drop creates cellular core (Fig. 15:) and skin of the product can be either porous or solid depending on the temperature of the mould – cold surface favours porous skin. The expanding gas holds the pressure in the mould and final part is usually 10–30 % lighter than the equivalent solid part [56]. Also, shrinkage at the mould

wall is compensated by foaming of the melt, which allows using of less holding pressure or even no holding pressure in ideal case [55].

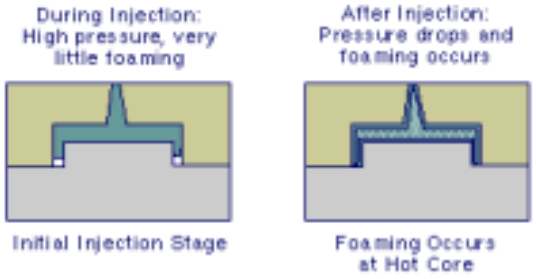

Fig. 15: Scheme of filling the mould with polymer/gas mixture and following expansion of gas [56]

2.7.3 Freeze casting method

Freeze casting is "a wet shaping technique involving preparing of stable colloidal suspension". This suspension is then poured into a mould, frozen and put into vacuum, so the dispersed medium can sublimate (Fig. 16:). The dispersing media are usually water or camphene and the suspension should be stable and evenly dispersed. When the solidification of suspension occurs, the walls are created by removing particles of solute with solidifying liquid. Next step is post-solidification solid removal, when pores are created in a manner of preserving the structure of the solidified fluid. Green state samples with homogenous or directional microstructures are products of this technique. This technique got a lot of attention in the beginning of 21st century due to possible usage in porous polymer and ceramic biomaterials.

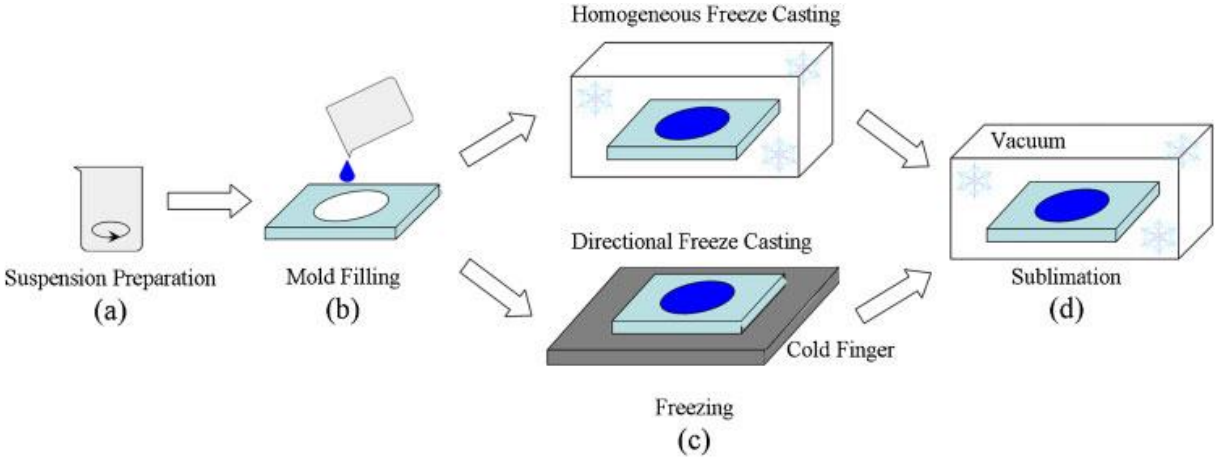

Fig. 16: Scheme of wet-freeze casting process [57]

In last years, the versatility of freeze casting was revealed as it can be also used for processing metals or pharmaceuticals and composites of ceramic/metal, ceramic/polymer, metal/polymer. The essential advantage of this technology rests in creating materials with adjustable porous microstructure. The freezing conditions are key parameter for achieving desired microstructure. Homogenous (cellular) microstructure with interconnected pores can be created if directional growth of solidifying medium is inhibited and uniform temperature and freezing rate are set. On the contrary, also directional (lamellar) well-defined structure is created when temperature gradient is applied, and the solidifying medium grows in anisotropic direction. Other advantages include production of open pores with pore size gradient, fabrication of high porosity materials (up to 90 %), complex shapes

and fine features of products, and unique mechanical properties such as low elastic modulus and relatively high mechanical strength. [57; 58]

3 AIM OF DIPLOMA THESIS

a. Preparation of porous materials with controlled gradient of density
b. Measurements of mechanical properties of the prepared porous structures followed by analysis via known mechanical models

4 EXPERIMENTAL PART

4.1 Chemicals

4.1.1 Dentacryl

Dentacryl is a methyl methacrylate resin determined for technical usage produced as a powder and a liquid in a package. The polymerization process proceeds spontaneously after mixing of the two components by so-called chemical initiation. After curing, the colourless or slightly yellowish matter is created suitable for cutting, sawing, grinding or polishing. The mixing ratio of powder and liquid is recommended by the producer as 100 parts of powder for 45 to 55 parts of liquid. Utilization of Dentacryl is wide in various industries, e. g. in the electrical industry for its isolating properties, in engineering for watering the conducting plates of punches or in metallurgical laboratories. Some of the mechanical and the thermal properties are in table 2, and DSC diagrams of the powder and the mixture with mixing ratio 1:1 are in Fig. 47: and Fig. 48:, respectively [59].

Table 2: Left part – mechanical properties given by producer [59]; Right part – thermal properties measured on TGA

	[MPa]		T_g [°C]	
Bending strength	50	Dentacryl 1:1	1st heating	2nd heating
Tensile strength	20		79,8	81,1
Compressive strength	80			

4.1.2 UNICELL D 200 A

UNICELL D 200 A is a chemical blowing agent, which is chemically described as azodicarbonamide (Fig. 17:) with molecular weight 116,08 $g \cdot mol^{-1}$ and it is produced in the form of fine yellow powder. The decomposition temperature is determined in the range from 202–208 °C and the volume of gas produced is 225–250 ml/g [60]. Various ways of thermal decomposition were presented as it depends on the decomposition temperature. The produced gas consists mainly of nitrogen, carbon monoxide and isocyanic acid at lower temperatures or ammonia at higher temperatures. After the decomposition, white residue remains consisting of biurea, cyanuric acid and urazole.

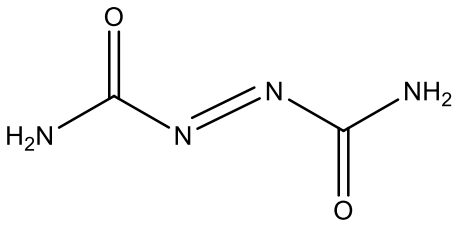

Fig. 17: Azodicarbonamide [ChemDraw Pro 12.0]

When azodicarbonamide decomposes, two main primary reactions take place concurrently:

- in the first reaction, biurea, nitrogen and isocyanic acid are formed (11)
- in the second reaction, urazole, nitrogen, isocyanic acid and ammonia are formed (12)

However, urea is unstable at the temperatures of azodicarbonamide decomposition, it is present in sublimate due to the recombination of ammonia and isocyanic acid in the cooler parts of reaction space. The result of the reduction of isocyanic acid by undecomposed azodicarbonamide is carbon monoxide, which is only produced after a sufficient amount of isocyanic acid has been formed.

TGA and DSC curves of azodicarbonamide are showed in Fig. 49: and Fig. 50:, respectively.

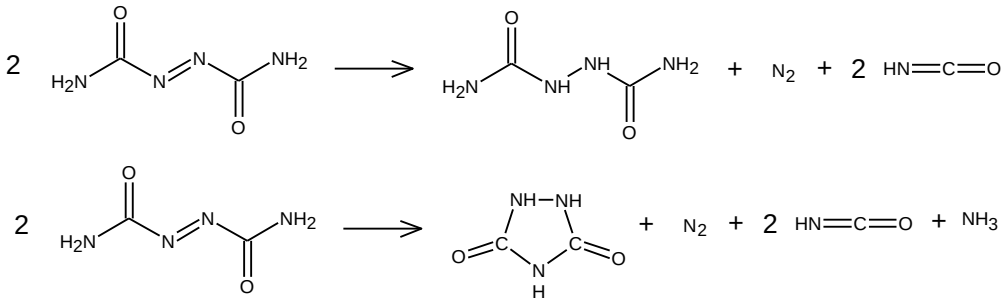

(11)

(12)

4.1.3 Polylactic acid

PLA filament "Gembird natural" without any additional pigments was used for printing 3D samples. The PLA filament was chosen due to its low melting temperature suitable for printing tiny parts and low thermal expansion securing low deformation of printed pores. Also, biodegradability and availability were advantages. Recommended printing temperatures are 210±10 °C for the nozzle and 40–60 °C for heatbed. Material properties are given in table 3.

Table 3: PLA filament properties given by the producer – σ_y is yield strength; d is filament diameter

ρ [g/cm^3]	1,25
MFI [g/10 min] 2,16 weight	5
T_m [°C]	190-220
σ_y [MPa] 5 mm/min	45
d [mm]	1,75±0,05

4.2 Sample preparation

Two kinds of samples were prepared – first, layered structure, where the mixture of a prepolymer, monomer and the chemical blowing agent were layered with different amount of the CBA in each layer and second, 3D printed structure, where internal pores and gradient structure were precisely manufactured by using the die of 3D printer.

4.2.1 Preparation of layered gradient structure

Layered gradient structure was prepared using PMMA as a matrix and azodicarbonamide as the CBA. There was used commercial product Dentacryl, which consist of the prepolymer of PMMA in the form of a powder and a liquid, which is a low-molecular product for crosslinking of PMMA prepolymer. A specific amount of azodicarbonamide was dissolved in the liquid and this mixture was placed under an ultrasonic gun for 1 min to destroy clusters of azodicarbonamide in the liquid. After, this liquid mixture was mixed with the powder in a beaker for 30 s and poured into the mould (Fig. 19:). The mixing ratio of the powdered prepolymer and the low-molecular liquid was set to 1:1. The amount of the CBA (table 4) dissolved in the liquid was calculated from the overall amount of the powder and the liquid. The filled mould was immediately moved into the pressure polymerator "K+B polymerátor Trystom", where polymerization run under the pressure of 0,5 MPa. The time spent in the polymerator varied according to the amount of the CBA in the PMMA matrix – 5 % CBA → 30 min, 3 % → 30 min, 1 % → 3,5 h. Then, the mould was taken out, another layer with

different amount of the CBA was laid on the almost polymerised layer and this way filled mould was placed in the pressure polymerator again. An important step in the procedure was lowering the pressure slowly before taking it out to avoid undesired release of the bubbles. The prepared sample was placed in the drier for 12 h at the temperature 100 °C for curing.

Table 4: The amount of the CBA in the individual layers

layer	CBA [%]
bottom	5
middle	3
up	1

After, the cured sample was placed into the cylinder with a diameter of 1,8 cm made of hard aluminium foil on a beaker (Fig. 18:). It is important to place the sample in the cylinder, so the body keeps its dimensions after the CBA decomposition and release of the gas. This sample was moved into the drier, where the temperature was set at 215 °C and the decomposition of the CBA went on for 30 min. This foamed sample was, then, adjusted with an electric chopper using hot wire as a cutting mechanism. Only the top side of the body needed to be cut.

Fig. 18: Photo of the mould for foaming the PMMA with dispersed CBA; Camera

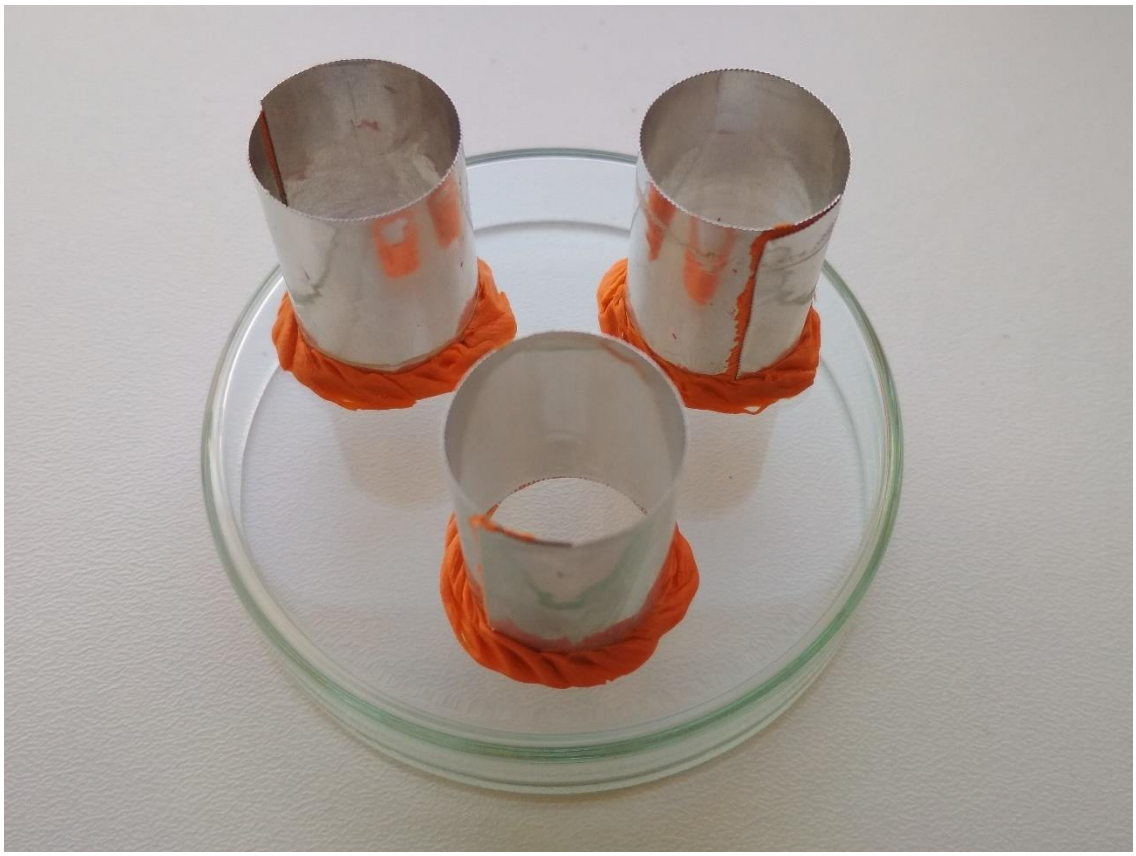

Fig. 19: Mould for the layered structure of the PMMA resin; hard aluminium foil was bond together with play-dough on a Petri dish

4.2.2 Preparation of 3D printed gradient structure

3D printed samples were prepared on "Prusa i3 MK3S" using commercial colourless PLA filament "Gembird". The samples were prepared as follows:

- Compact samples without porosity
- Samples with uniform porosity of 20, 40, 60 and 80 %
- Samples with 3 different gradients of porosity

From each type, there were 10 samples, 5 were tested for bending strength in three-point bending test and another 5 were tested with a notch for bending strength in three-point bending test. The printing temperature was set for 200 °C, and, for the first layer, it was 215 °C. The temperature of the heatbed was 50 °C and 55 °C for the first layer. The printing speed was adjusted when preparing porosity gradient samples due to the precise dimensions to lower values. The amount of extruded filament was adjusted, too, and it was moved between 1-1,15 of the pre-set value.

4.3 Testing methods

4.3.1 The density of the samples

The densities of the samples were obtained differently for each type of sample. For layer-by-layer samples, there was used water displacement method based on Archimedes´ principle, and at least three measurements were carried for each load of the CBA and the solid PMMA. As the 3D printed samples had regular outer shape – rectangular - the density was calculated by measuring the dimensions and weighing the samples. At least three measurements were carried for each type of 3D sample.

4.3.2 Thermogravimetric analysis

TGA was used for the Dentacryl mixture and for the CBA. When measuring the Dentacryl mixture, first, the temperature of the degradation was of interest, and, then, the simulation of the foaming was performed on PMMA loaded with the CBA to observe, if degradation of PMMA occurred upon the foaming. TGA of the CBA was used to determine the temperature of its decomposition. The measuring programmes were as follows:

PMMA and Azodicarbonamide

- Heating 10 °C/min to 650 °C in a nitrogen atmosphere
- Switch to oxygen
- Hold for 20 min

PMMA loaded with CBA

- Heating 50 °C/min to 215 °C
- Hold for 30 min
- Heating 50 °C/min to 600 °C

4.3.3 Differential scanning calorimetry

DSC was performed on the Dentacryl powder, UNICELL D 200 A and the PLA filament for determination T_g. The testing programmes were as follows:

- Cool down 10 °C/min to –70 °C and hold for 1 min
- Heating 10 °C/min to 250 °C and hold for 1 min
- Cool down 10 °C/min to –70 °C and hold for 1 min
- Heating 10 °C/min to 250 °C and hold for 1 min
- Cool down to the room temperature

4.3.4 Confocal laser scanning microscopy

CLSM was performed on the samples prepared by the layer-by-layer technique by the confocal microscope OLYMPUS OLS4100. The magnification used were 5×, 10× and 20×. The snapshots were captured under the optical light and using the laser. The snapshots were always taken from two different spots with each magnification, and the sizes of the pores and the thicknesses of the walls were measured. The samples with the uniform density were investigated in the centre and at the edges, whereas the density gradient foams were investigated at the transfers between the layers. From the snapshots, pores´ sizes and walls´ thicknesses were investigated by the software included with OLS4100.

4.3.5 Scanning electron microscopy

Scanning electron microscopy (SEM) pictures were taken to determine the distribution of the CBA in the PMMA matrix and to set the difference between various loading of the CBA. The test was performed on Verios 460L and the images were taken when detecting secondary electrons for enhancing topographical contrast.

4.4 Mechanical tests

4.4.1 Compressive strength

This test was performed on the samples prepared by the layer-by-layer technique in order to determine the compressive strength difference between the samples with the uniform density and samples with the density gradient. The procedure was set as follows:

- compression test on Zwick Z010
- measuring head – 10 kN maximum load

- dimensions of testing samples – cylindrical shape with specific dimensions for each sample
- test speed – 1 mm/min

4.4.2 Bending strength

This test was performed on the 3D printed samples in order to determine the bending strength difference between the samples with the uniform density and the samples with the density gradient. The test run on the samples without previous crack and on the samples with a notch. The notch was made on the Power.Driven Notchvis (CEAST) and the depth of the notch was 0,45*W* of the sample, where *W* is the width of the sample, as stated in [61]. The procedure was set as follows:

- 3-point bending test on Zwick Z010
- measuring head – 10 kN maximum load
- support separation – 128 mm
- the diameter of support and grips – 5 mm
- test speed – 1 mm/min
- dimensions of testing samples – (8×8×160) mm^3
- depth of the notch – 3,6 mm
- the test was performed according to ČSN EN ISO 178 except for the width of the sample

5 RESULTS AND DISCUSSION

5.1 Layer-by-layer technique

A new procedure was developed for manufacturing density gradient foams. Although, the gradient is not continuous, due to the layering of the layers with different amount of the blowing agent resulting in a jump change. The foam density, the polymerisation pressure, the simulation of the foaming, the internal pore structure, and the compressive strength were examined on the samples prepared by this technique and are further discussed in the following chapters.

5.1.1 Foam density

The foam density was observed to determine the best time for the foaming, and, then, the dependence of the foam density on the amount of the CBA filled into the matrix was of interest. The time of the foaming was observed on the samples filled with 3 % of the CBA. There were chosen times from 15 to 30 min with 5 min step, and after the foaming at 215 °C, the density was measured. In Fig. 20:, there can be seen a steep decrease of the foam density with the increasing time of the foaming. The lowest density was obtained for the foaming time of 30 min and this was also the chosen time. The density of the samples with a uniform density over the whole body should grow with the decreasing amount of the CBA, which was confirmed and is depicted in Fig. 21:. As the CBA amount is increasing, more pores are created resulting in a lower density.

Comparing samples with the uniform density over the whole volume to the sample with density gradient (Fig. 22:), there can be seen that the density gradient sample has a value of the density in the range of density values of the uniform samples. The range of densities is from 0,12 g·cm^{-3} for the CBA loading of 1 % to 0,06 g·cm^{-3} for the CBA loading of 5 % and the gradient density value is 0,10 g·cm^{-3}.

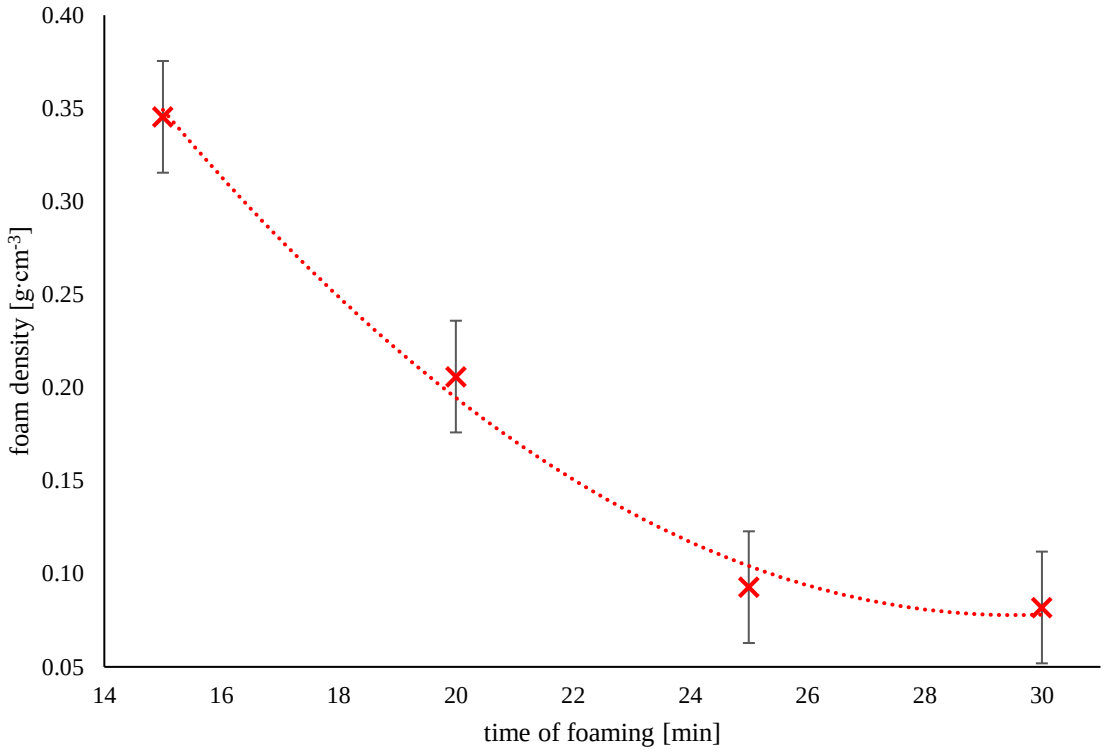

Fig. 20: Diagram of the dependence of the density of a uniform porosity PMMA foam at a temperature 215 °C and 3 wt. % concentration of the CBA on the time of the foaming, the red curve is a guide for the eyes only

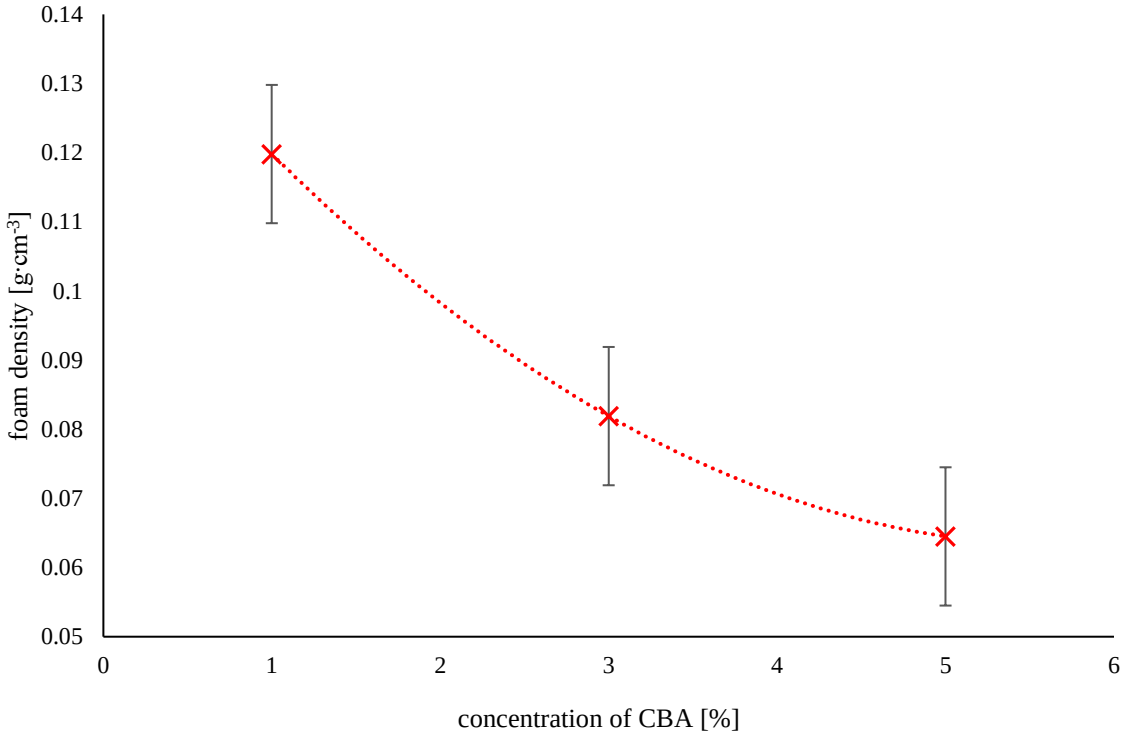

Fig. 21: Diagram of the dependence of the density of a PMMA foam at temperature 215 °C and foaming time of 30 min on the concentration of the CBA; the red curve is a guide for the eyes only

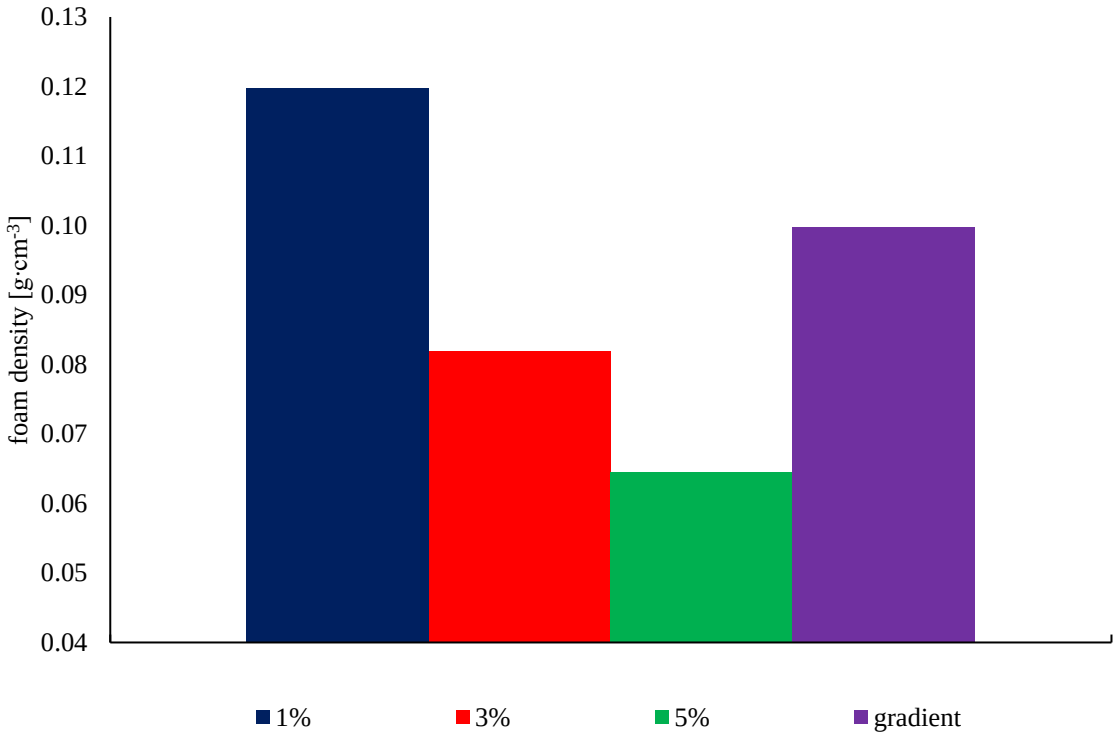

Fig. 22: Diagram depicting varying densities of the uniform density PMMA foams (1, 3, 5 %) and density gradient PMMA foams at temperature 215 °C and time of foaming 30 min; the value of the density gradient PMMA foam (purple column) lies within the values of the uniform density PMMA foams (dark blue, red, green columns)

5.1.2 Pressure during polymerisation of PMMA

During the polymerisation of PMMA, small bubbles emerged in the sample before the foaming. This created not controlled and uneven porosity in the samples before the foaming, which was not desired. To prevent this phenomenon, polymerisation under the pressure was suggested. In Fig. 23:, there can be seen transparent samples without the CBA polymerized under three different pressures. Almost vacuum pressure (left sample) worked well, and no bubbles were seen after the polymerisation. However, upon the release of low pressure to the ambient pressure, the sample expanded in the top layer and big bubbles started to come up on the surface. Atmospheric pressure (middle sample) caused releasing of the bubbles in the whole volume of the body. With the increased pressure of 0,5 MPa (right sample), there was also achieved non-bubble structure, but the same phenomenon occurred as with the low pressure, and that upon the release of the pressure small bubbles came up in the top layer. This was solved by an extension of time spent in the high-pressure environment and slow releasing to the ambient pressure. Also, the dimensions of the sample were preserved using 0,5 MPa pressure. As this high-pressure method was easier to manufacture and the non-bubble structure achieved was sufficient, the pressure of 0,5 MPa was chosen.

The time spent under the increased pressure varied according to the amount of the CBA loaded in the sample. As it was observed, the higher amount of the CBA in the sample caused the faster time of the polymerisation. This can be caused by introducing particles into the polymer matrix, which makes the sample stiffer. When foaming the uniform density samples, the concern was to have the samples under the increased pressure until the polymerisation is finished. However, to secure the best connection between layers of the density gradient structure with different loading of the CBA, the polymerisation time was shortened, so the surface of the layer was not polymerised completely and after pouring another layer on the top of it, the bonds were formed also with the previous layer.

As it may seem, the delamination should be of concern. But during the foaming, the polymer matrix melted a little bit resulting in a very good connection between the layers. In Fig. 24:, there can be seen the density gradient structure without visible transfers between the layers. When looking with a naked eye, it is not obvious, where the layers with different loading of the CBA are connected. Comparing with the structure studied with the confocal microscope, there is no obvious difference between the layers. So, it can be considered, that the bonding between the layers, and, further, foaming caused a very good connection between the layers.

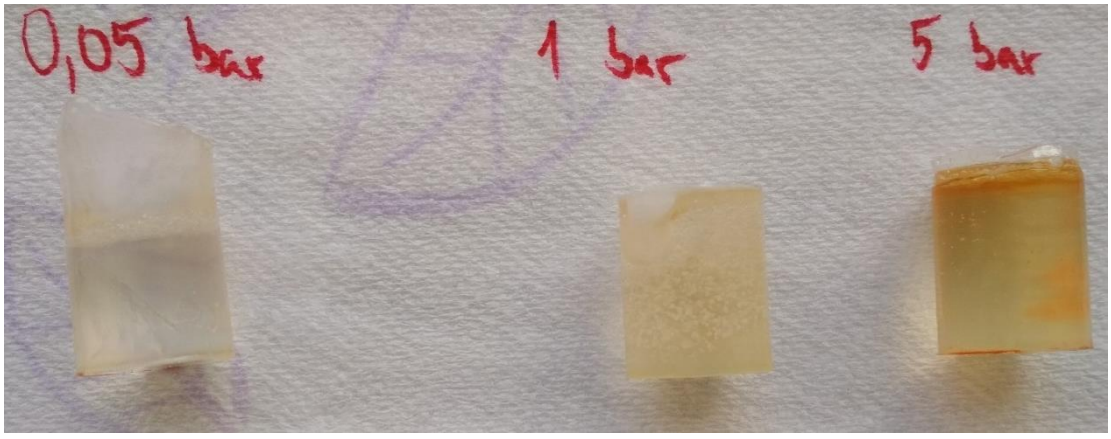

Fig. 23: Photo of the Dentacryl samples polymerised under three different pressures and at laboratory temperature 20 °C; left sample – polymerisation under 0,05 bar without bubbles and with deformed top layer; middle sample – polymerisation under atmospheric pressure with bubbles in the whole volume of the sample; right sample – polymerisation under 5 bar without bubbles and undeformed top layer

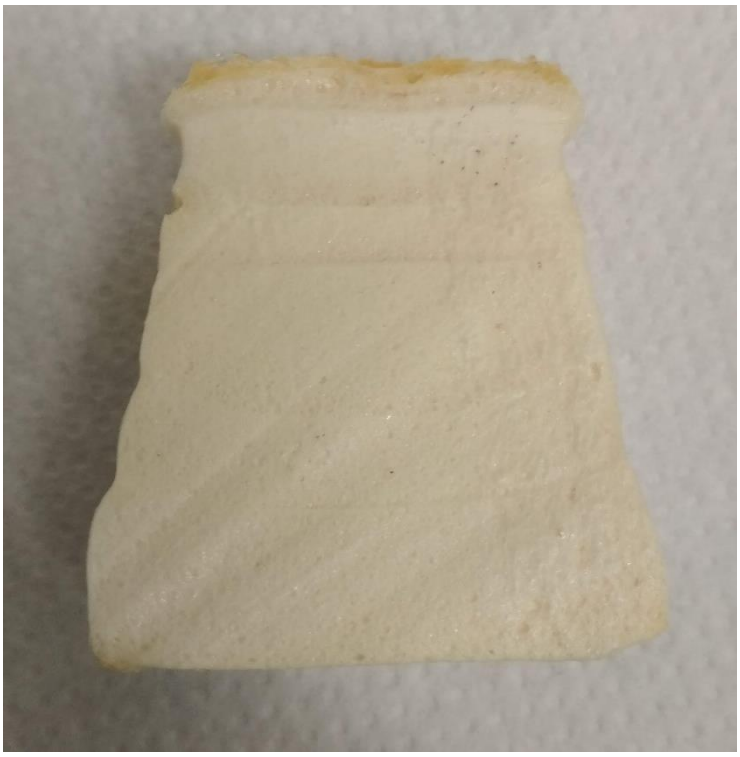

Fig. 24: Photo of the density gradient structure of the PMMA foam without visible transfers between the layers containing different amount of the CBA; from the bottom to the top, there are layers with 5, 3, and 1 wt. % of the CBA

5.1.3 Simulation of the foaming process

This simulation was performed to observe if the degradation of PMMA occurs upon release of the gas. It was discovered that PMMA degrades upon the release of the gas because the decrease of the mass is much bigger than the loading of the CBA. In Fig. 25:, there can be seen the decrease in the PMMA mass in a percentage in respect with the time of foaming. The decrease can be also caused by non-reacted monomer or prepolymer in PMMA, which cannot withstand the temperature of the foaming. Obvious growth of mass decrease occurs with a rising amount of the CBA dispersed in PMMA matrix. This effect is expected as more CBA is decomposed.

However, the connection between the layers after the foaming was very good and the sample was not deformed. The increased temperature within the sample caused partial melting of the PMMA, thus creating better bonding between the layers, which is the desired effect. Also, a small sample put into thermogravimeter could act differently than a bulk material foamed in the drier. We can suppose that the bulk sample put in the drier had a different temperature at the surface than within a material, so the degradation could occur mostly on the surface. This could also cause uneven distribution of the pores´ sizes on the edge of the foam compared to the distribution within the foam.

In Fig. 25:, the red curve of the PMMA foam loaded with 1 % of the CBA is placed above the dark blue curve of the solid PMMA, which seems incorrect, because in sample loaded with the CBA should decompose the CBA, too, thus resulting in a bigger mass decrease. It is possible that small piece of the sample taken from the PMMA loaded with 1 % of the CBA contained smaller or no amount of the CBA, and the solid PMMA contained more unreacted low-molecular residues than the PMMA loaded with the CBA. Thus, it would be possible to observe a bigger mass decrease for pure PMMA.

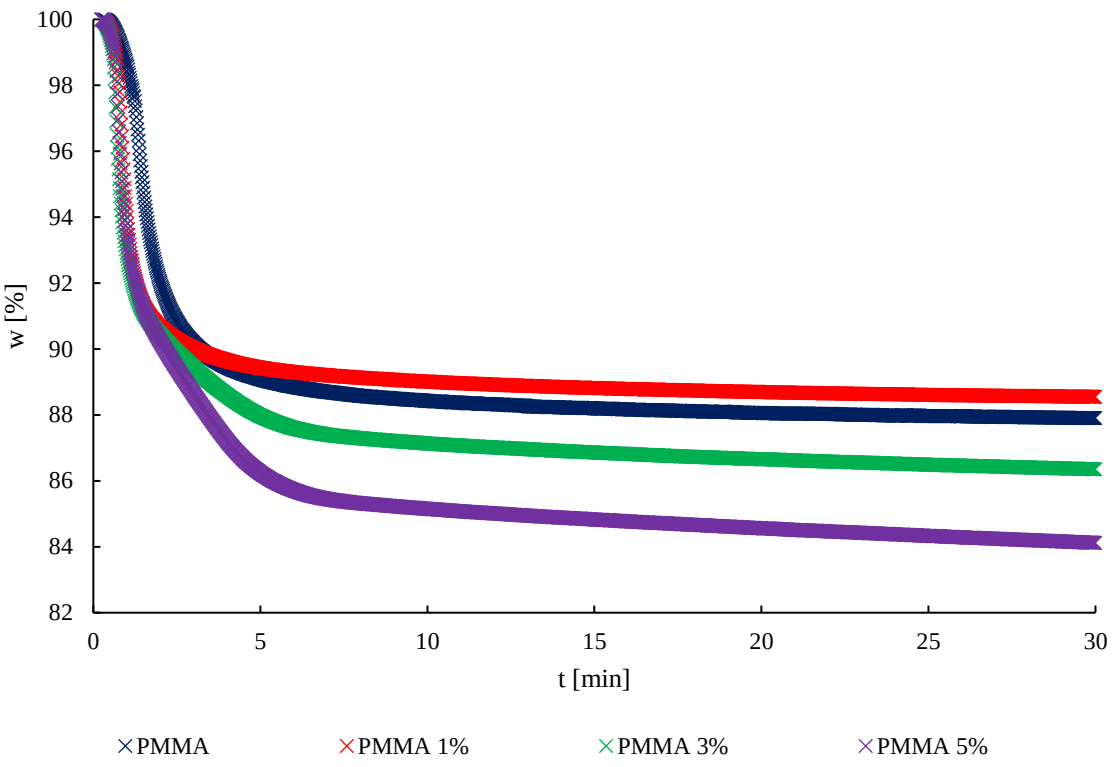

Fig. 25: Thermogravimetric curve displaying weight reduction of the non-foamed samples without the CBA (PMMA) and with different loading of the CBA (PMMA 1%, 3%, 5%) with time at a temperature 215 °C

5.1.4 Internal structure of the uniform density foams and the density gradient foams

The distribution of pores´ sizes differ depending on the amount of CBA dispersed in the matrix. The most uniform dispersion of the sizes of the pores performs the sample with 3 % of the CBA loaded in the matrix. There can be seen slightly better uniformity at the edges of the foam (Fig. 26:) than in the centre (Fig. 27:), but the difference is negligible. Significantly wider distribution of the pores´ sizes is visible in Fig. 26: and Fig. 27: for the samples with the amount of 1 and 5 % of the dispersed CBA. More uniform distribution was at the edges of the foam for both loadings of the CBA. This can be caused by the wall of the mould, where the samples were foamed, which restricted the expansion of the material, and so the pores could not grow to the bigger dimensions. However, the sizes of pores for all three loadings were mainly in range from 50 to 450 µm. Fewer pores emerged in the samples containing 1 % of the CBA and with the increasing amount of the CBA more pores were found. Although, there is not a big difference in the number of the pores between the samples with 3 and 5 % of the CBA loaded.

The pores´ distribution investigated in the density gradient samples showed similar trends for both transfers – from 1 to 3 % and from 3 to 5 % (Fig. 28:). However, significantly more pores of smaller diameter (around 50 µm) were found at the transfer from 3 to 5 %. The distribution of the pores on the top and at the bottom of the foam was investigated, so the determination could be done if there is a difference in the pores´ sizes, when the foaming is hindered by the mould (bottom) and when there´s no obstacle (top). Results in Fig. 28: show that at the top prevailed bigger pores, whereas at the bottom were smaller pores. But this could be caused by a different amount of the CBA at the top (1 %) and at the bottom (5 %).

Various amounts of the CBA caused different dimensions of the foamed samples (Fig. 29:). This effect could also cause different sizes of the pores and their distribution when foaming occurred in the mould and without the mould. As we needed gradient samples for the mechanical tests to be in

the cylindrical shape, we chose to foam our samples in the mould. Further in the discussion, there is made a comparison between the foams prepared in the mould and the foams prepared without the mould. The mould was chosen, because the treatment of the foamed samples was difficult, mainly damaging of the sample structure was of concern, and there were not suitable machines for cutting the samples.

The values of the sizes of the pores can be found in table 5.

Table 5: The pore´s sizes calculated as the weighted average of the number of the pores in respect with their diameter

	pore sizes [µm]			pore sizes [µm]			
	edge	centre		top	1 % - 3 %	3 % - 5 %	bottom
1%	247	250					
3%	184	161	gradient	220	222	159	161
5%	200	255					

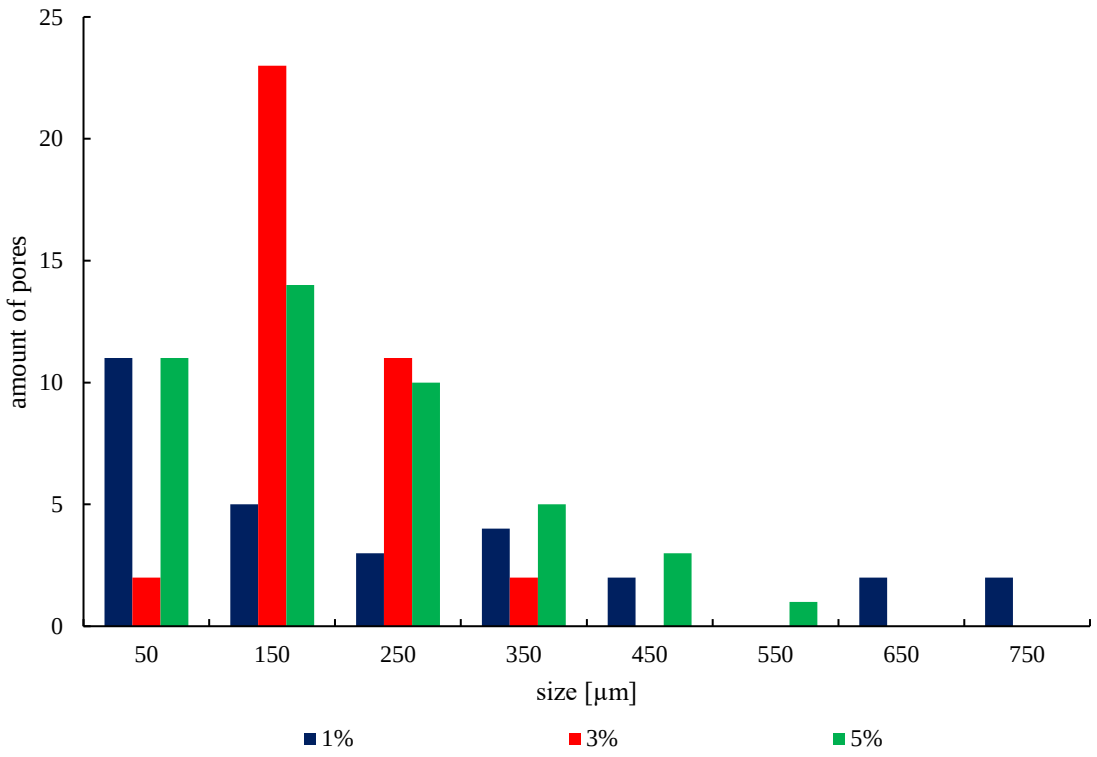

Fig. 26: Diagram of the pores´ quantity in respect with their diameter measured at the edges of the uniform density PMMA foams

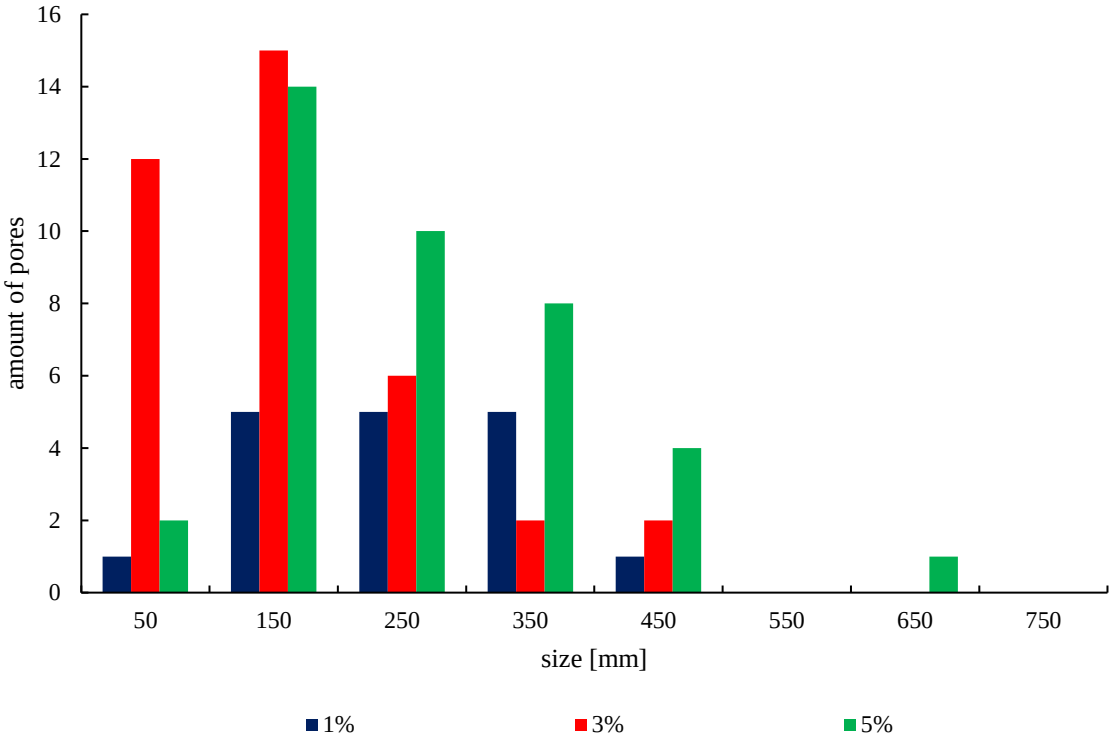

Fig. 27: Diagram of the pores´ quantity in respect with their diameter measured within the uniform density PMMA foams

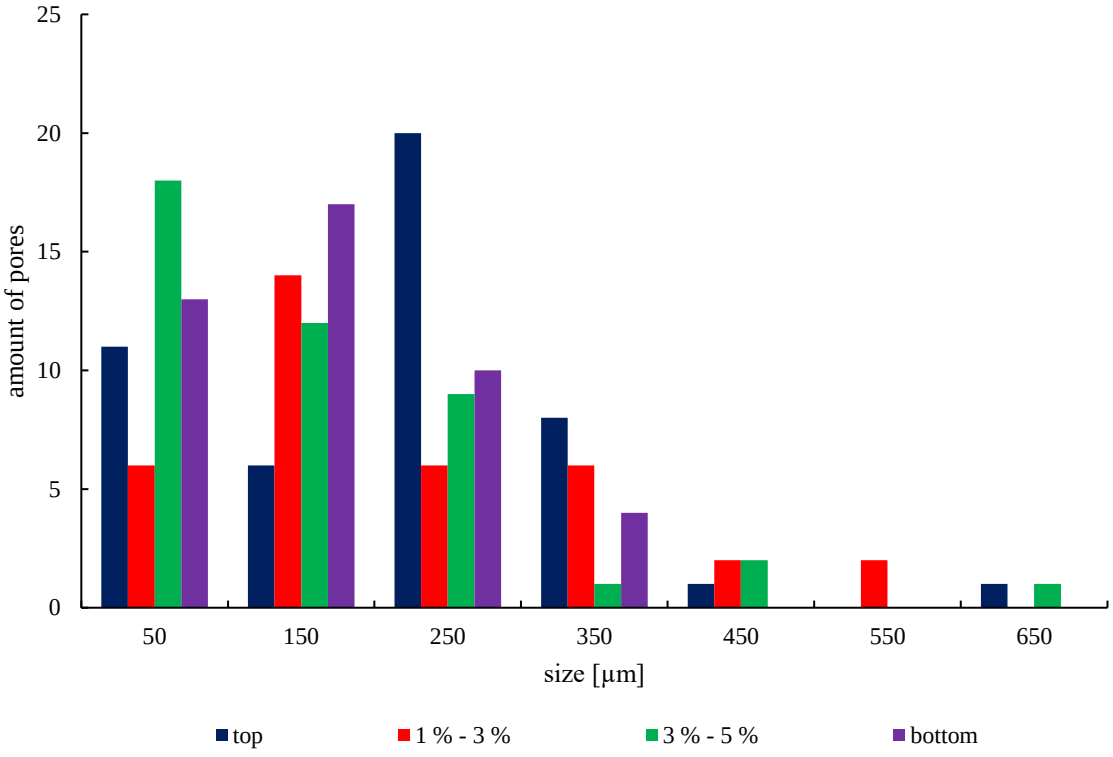

Fig. 28: Diagram of the pores´ quantity in respect with their diameter measured in the density gradient PMMA foams; top – pores at the top layer of the foam; 1 % - 3 % and 3 % - 5 % – pores at the transfers between the layers containing different amount of the CBA corresponding to the numbers in the name; bottom – pores at the bottom layer of the foam

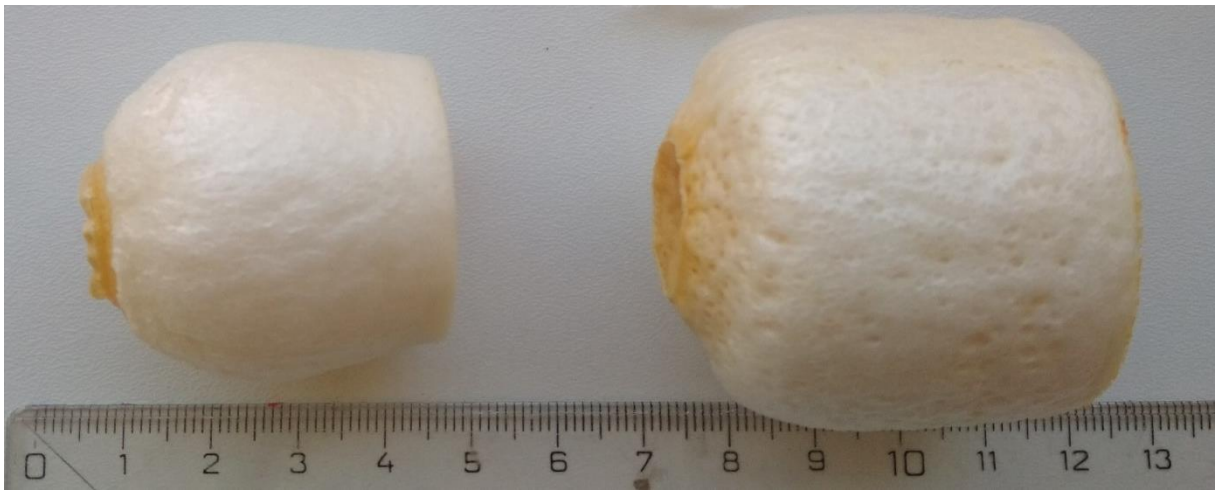

Fig. 29: Photo of the PMMA samples foamed without the mould at 215 °C for 30 min – left contains 1 % of the CBA and right contains 3 % of the CBA; their dimensions after foaming rise with the rising amount of the CBA

CLSM images (Fig. 30: and Fig. 31:) were taken to investigate the shape of the pores and not visible differences with a naked eye between the samples with various loading of the CBA. It was observed that the pore shape was solely circular varying only in the diameter of the pore. In Fig. 30:, there are compared photos of the uniform density foams, where no significant difference can be observed. In Fig. 31:, there are compared photos of the gradient sample, specifically, the top of the foam, where was no obstacle for the growth during the foaming, the transfer between the layers with different amount of the CBA, and the bottom of the foam, where the growth was hindered by the wall of the beaker. However, no significant differences were recorded, too.

Also, SEM pictures were taken to investigate the arrangement of the CBA in the PMMA matrix in the non-foamed samples. In Fig. 32:, the top image shows the sample with 1 % of the CBA where can be seen particles of the CBA (yellow arrow) entirely covered in PMMA. However, in the images below, where the loading of the CBA is higher, 3 % and 5 %, respectively, the CBA particles are covered less in PMMA and for the sample with 5 % of the CBA, the particles are only partially covered in PMMA matrix. Nevertheless, the CBA particles in the sample with 1 % of the CBA were harder to find and most of the sample was composed of PMMA matrix. In the samples with 3 and 5 % of the CBA, the particles were more visible.

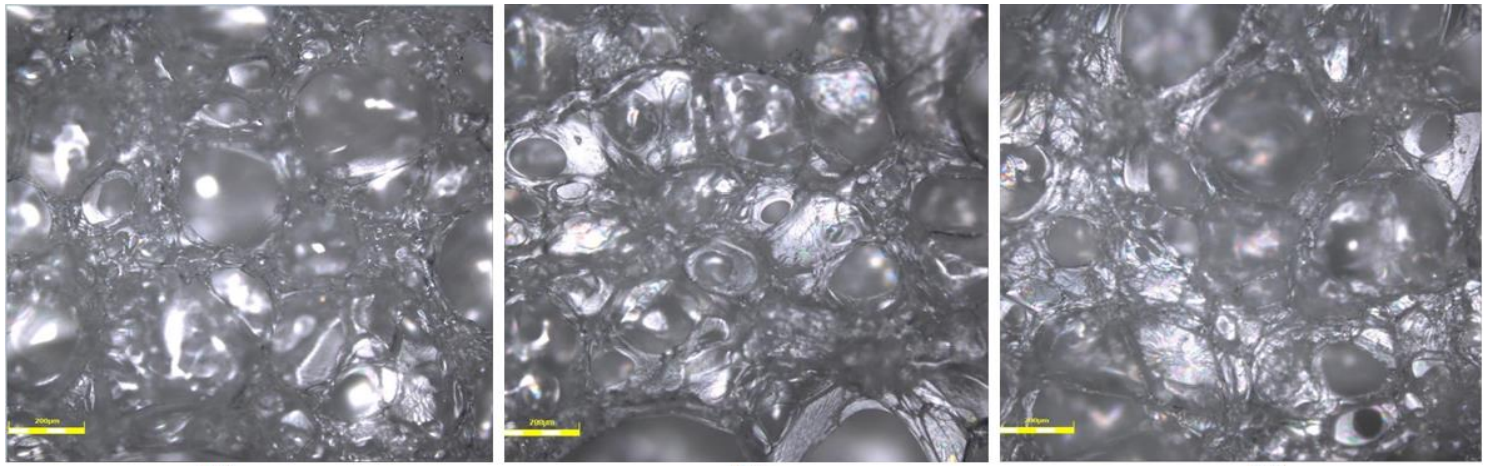

Fig. 30: Photos of the internal structure of the uniform density PMMA foams – left contains 1 % of the CBA, middle contains 3 % of the CBA, right contains 5 % of the CBA; the scale bar is 200 μm

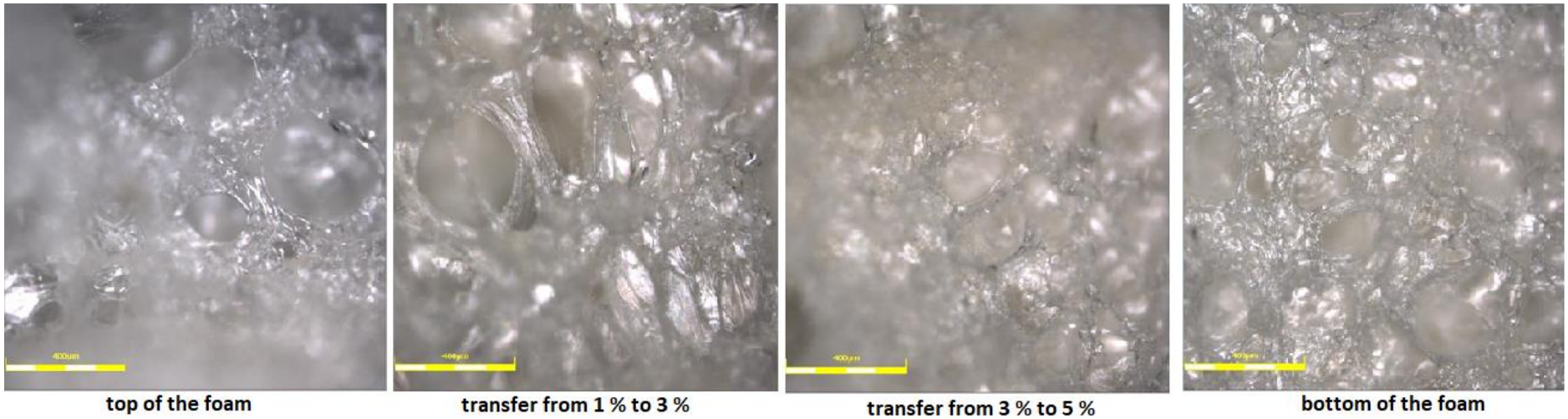

Fig. 31: Photos of the density gradient PMMA foam –top of the foam with 1 % of the CBA, transfer from 1 % to 3 %, transfer from 3 % to 5 % and the bottom of the foam 5 %; the scale bar is 400 μm

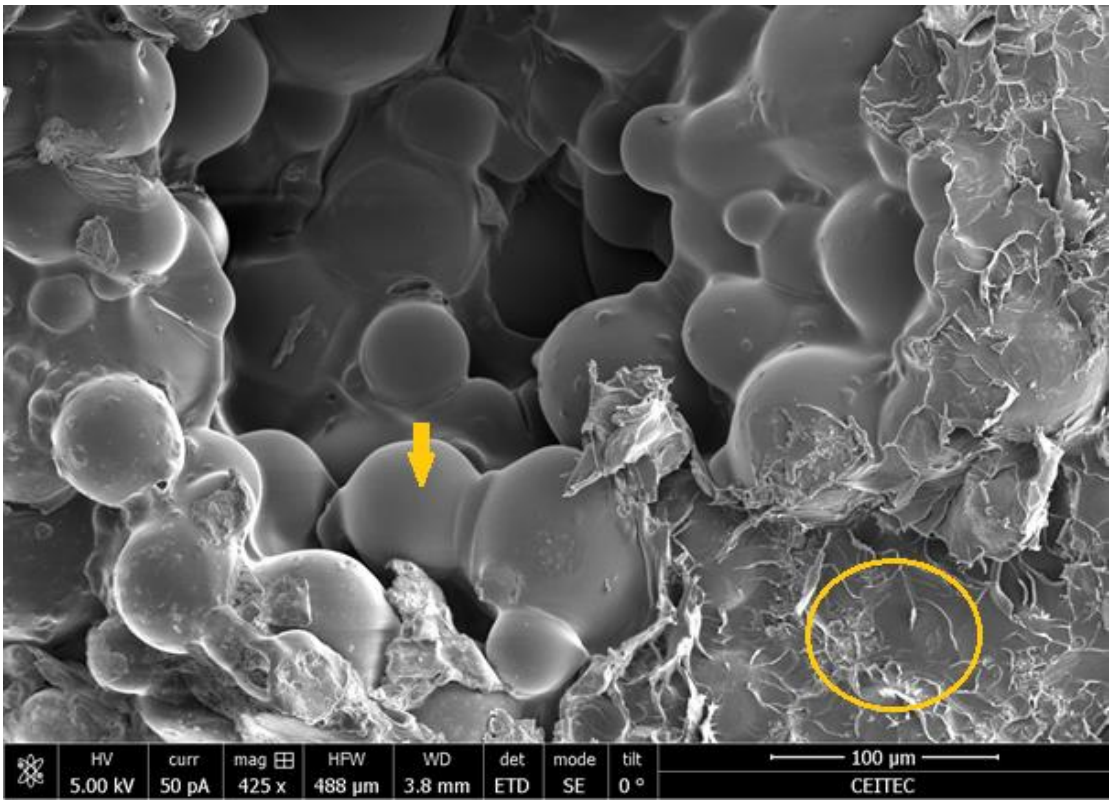
HV
5.00 kV
curr
50 pA
mag
425 x
HFW
488 µm
WD
3.8 mm
det
ETD
mode
SE
tilt
0 °
100 µm
CEITEC

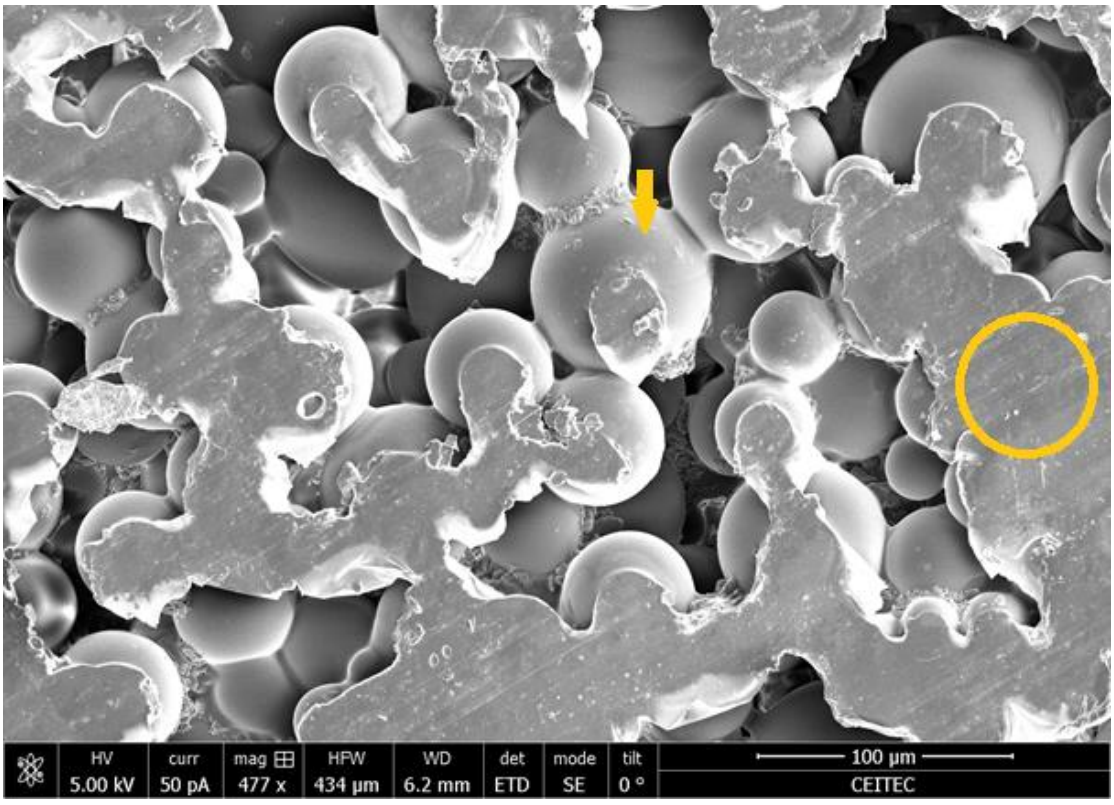
HV
5.00 kV
curr
50 pA
mag
477 x
HFW
434 µm
WD
6.2 mm
det
ETD
mode
SE
tilt
0 °
100 µm
CEITEC

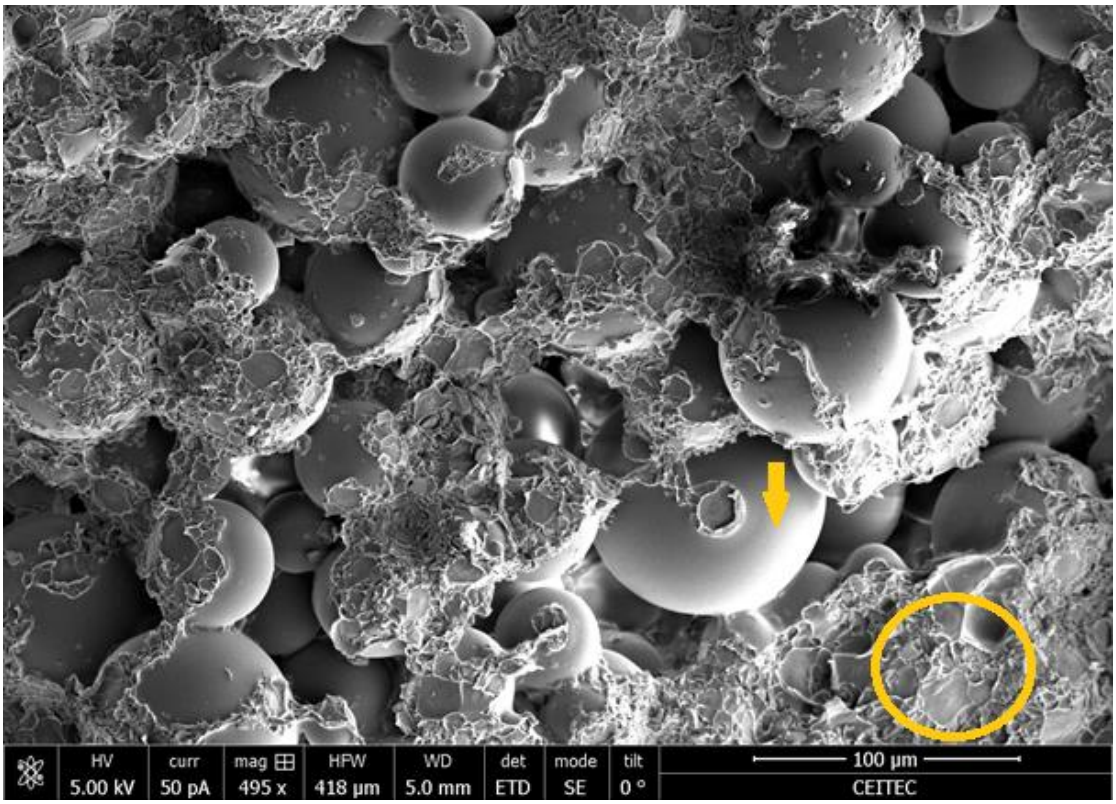

Fig. 32: SEM images of the dispersed CBA in PMMA matrix in non-blown samples; from top to bottom 1 % of CBA, 3 % of CBA, and 5 % of CBA; yellow arrows point on the CBA particles, yellow circles point on the PMMA matrix; in the top picture, the particles are covered in the PMMA; in the bottom picture, the particles are just partially covered in the PMMA

5.1.5 Compressive strength

The compressive strength was measured to determine if the stress-strain response of the density gradient foam, the uniform density foam and the non-foamed sample was changed. In Fig. 34:, there can be seen mechanical responses of all the mentioned samples. For the solid PMMA (purple curves), the value of the yield strength was 56,913MPa, Young´s modulus was 953,195 MPa and the compressive strength was 111,821 MPa. The compressive strength stated by the producer is 80 MPa. The region of elastic deformation, yield strength, plastic deformation region with increasing stress, and, then, failure could be observed for all types of samples. However, the values differed for each foam. The higher values of the stress were achieved in the foams with lower content of the CBA, because fewer pores were created, and so the sample was stiffer and tougher.

The density gradient foam (light blue curves) showed no improvement over the uniform density foams (dark blue, green and red curves). The values of the stress are very low, and the range of deformation is the same as for the uniform density samples. However, the values of Young´s modulus (8,223 MPa) and the compressive strength (6,553 MPa) of the density gradient foam lie between the values of the uniform density foams. The values of Young´s modulus are from 4,304 to 18,944 MPa and the compressive strength from 5,986 to 8,647 MPa for the uniform density samples from the highest to the lowest loading of the CBA. Such low values and similar results could be caused by the different approach in the preparation of the density gradient samples. With the various amount of the CBA in the PMMA matrix, the dimensions of the foamed sample differed, and after the foaming of the gradient structure conical samples were obtained (Fig. 33: - left picture). In order to prepare cylindrical samples, the cylindrical mould was used with the dimensions of the foamed sample with the lowest content of the CBA used (1 %), where only the top was not hindered by the wall of the

mould (Fig. 18:). However, the layer with the highest content of the CBA (5 %) had no place to expand, so big bubbles emerged inside the body, which caused the uneven structure of the pores, and thus lower stress values in the yield strength and the compressive strength, too. Knowing this phenomenon, it would be suitable to prepare density gradient samples without the mould, and, then, adjust the sample for desired dimensions using, for example, laser cutter.

Fig. 33: Photo of the density gradient PMMA foams foamed at 215 °C for 30 min with conical (left) and cylindrical (right) shape; left – foamed without a mould; right – foamed with a mould

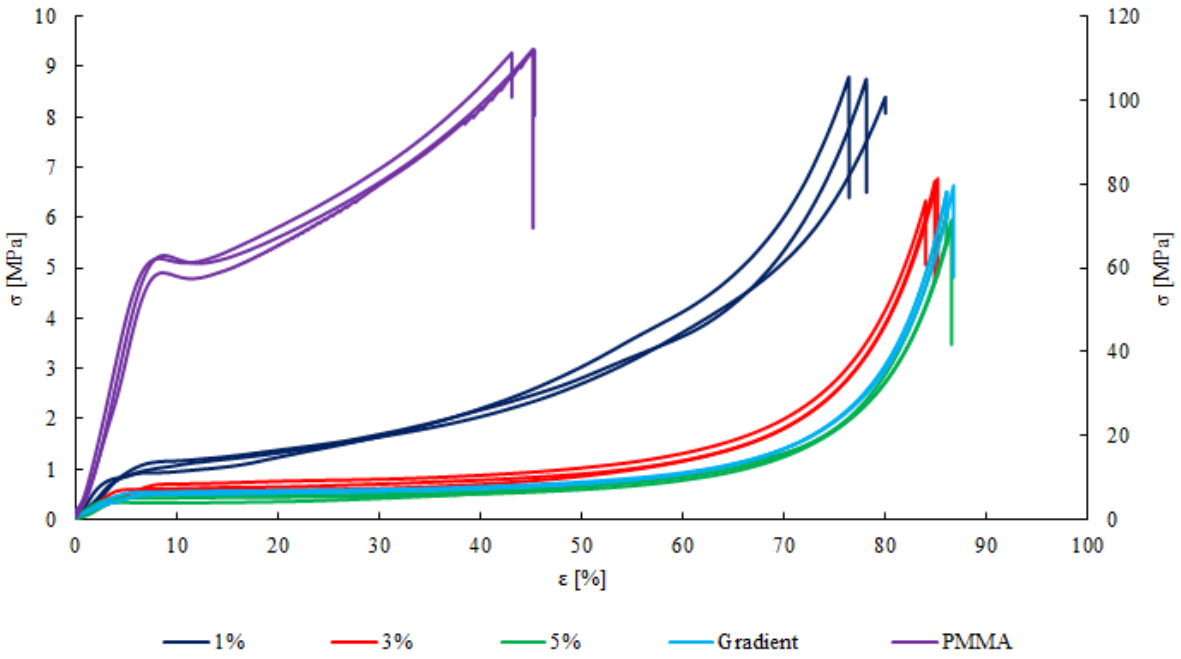

Fig. 34: Diagram of the stress-strain curves for non-foamed sample (purple curves), the uniform density foams (dark blue, red, green curves) and the foams with the density gradient (light blue curves); right y-axis is for pure PMMA and left y-axis for all other curves

5.2 3D printed gradient structure

A suggestion of making very precise pore structure by using 3D print was performed and 3 different structures of the porosity gradient were manufactured. The bending strength in the 3-point bending test and fracture toughness were investigated and compared to the uniform porosity samples.

5.2.1 DSC of the PLA filament

DSC was performed in order to determine the melting temperature and find the best printing conditions. In table 6, there can be seen the melting temperature of 170 °C confirmed in both heatings, whereas the producer stated range from 190 to 220 °C (table 3). Also, the recrystallization occurred during both heatings and is stated in table 6 with index *r*. This phenomenon was also confirmed in [62]. However, the recommended temperature for the 3D print was 230 °C stated by the producer, the chosen temperature performing the best samples was 200 °C. During the cooling, no crystallization occurred, and, only, the glass temperature transition was recorded. The crystallinity of the PLA was calculated using the equation:

$$w_c = \frac{H_m}{H_m^0} \cdot 100\ \% \tag{13}$$

Table 6: DSC results of the PLA filament with calculated crystallinity (w_c) – H_m is a heat of melting, T_r is a temperature of recrystallization, H_r is a heat of recrystallization

	Heating	
	1.	2.
T_g [°C]	63	62
T_m [°C]	170	170
H_m [J/g]	29,8	29,3
T_r [°C]	95	98
H_r [J/g]	26,1	28,1
H_m^0 [J/g]	93	93
w_c [%]	32,0	31,5

5.2.2 3D printed density gradient samples

By using filament deposition modelling 3D print very precise pore structure was introduced into the samples. As mentioned before, the geometry of pores and their distribution are of great importance for the resulting mechanical properties. In Fig. 36:, there can be seen how the porosity rises in each 3D structure. On the x-axis, there is the height of the sample from the surface (in region 0-0,5 mm no porosity occurs in the sample), where is no porosity to the centre of the sample (4 mm), where is the highest porosity. There are shown only values to the centre of the sample as the porosity rises in the same way to the centre from both edges. 3 different trends are depicted, and all are convex. Type I and II achieved the same resulting porosity, whereas type III had slightly lower porosity what should cause higher values of the bending strength.

In Fig. 37:, there are sketched 3 different types of porosity introduced in the 3D printed samples. The dimensions of the samples are 8 mm for width, 8 mm for height and 160 mm for length (Fig. 35:). As can be seen in Fig. 37:, the size of the pores and their distribution within the material vary

according to the structure. Thanks to the precise geometry of the pores, the comparison of the bending strength and Young´s modulus can be done among the 3 gradients.

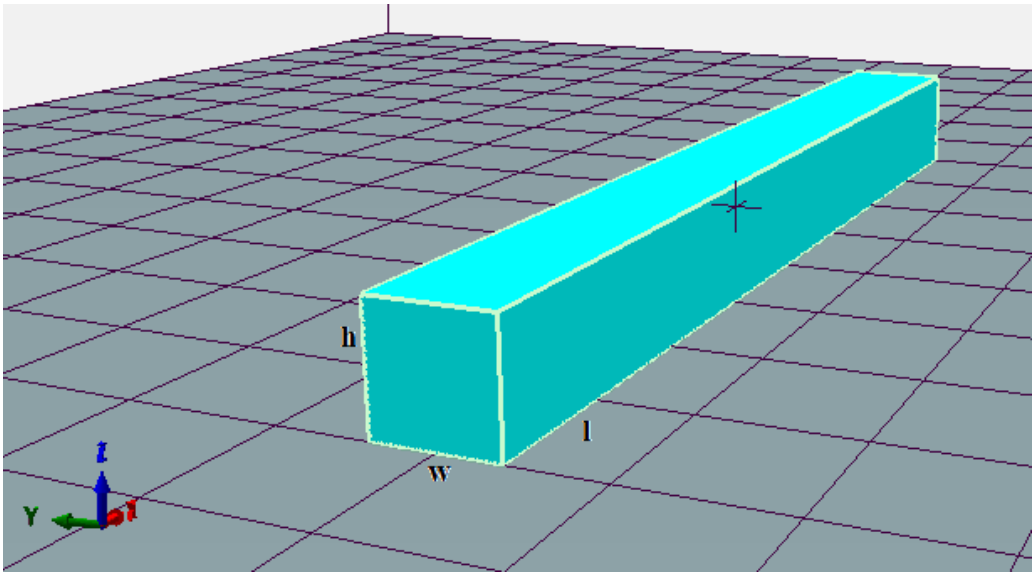

Fig. 35: A digital scheme of the 3D printed sample with indicated dimensions; h – height, w – width, l - length

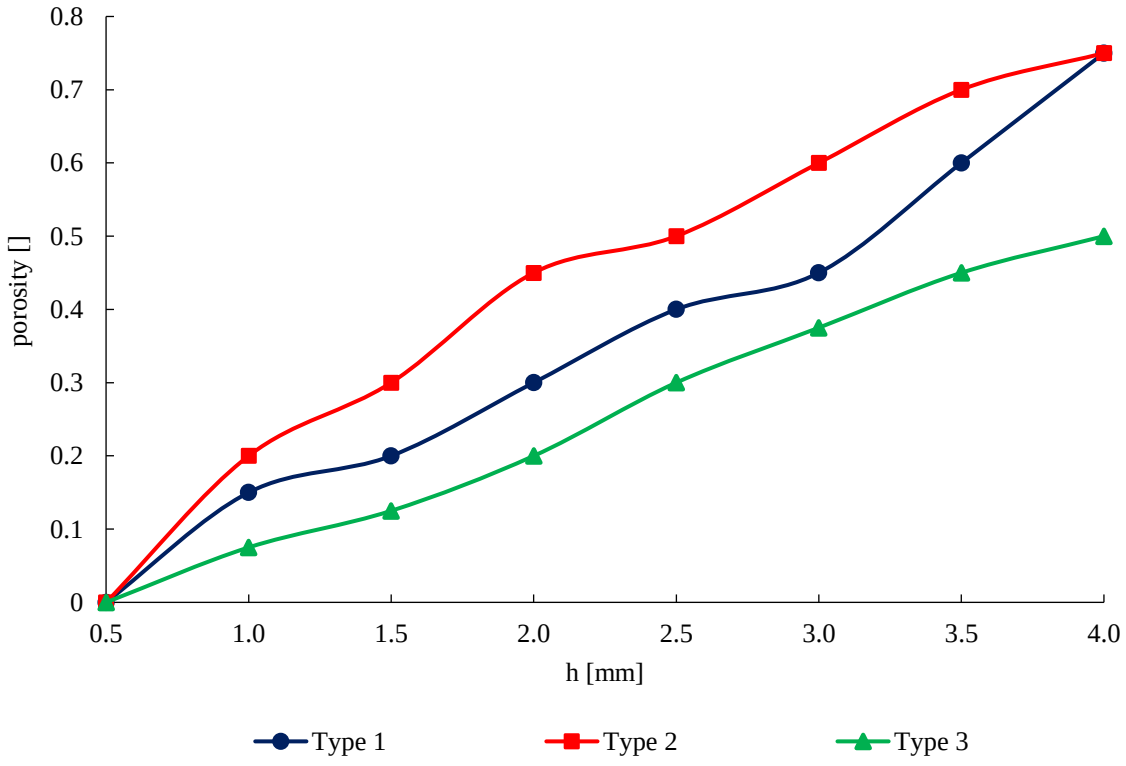

Fig. 36: Diagram of the 3 investigated 3D printed porosity gradient structures showing their different porosity trends within the material in respect with rising height from the edge to the centre of the sample; the curves are guides for the eye only

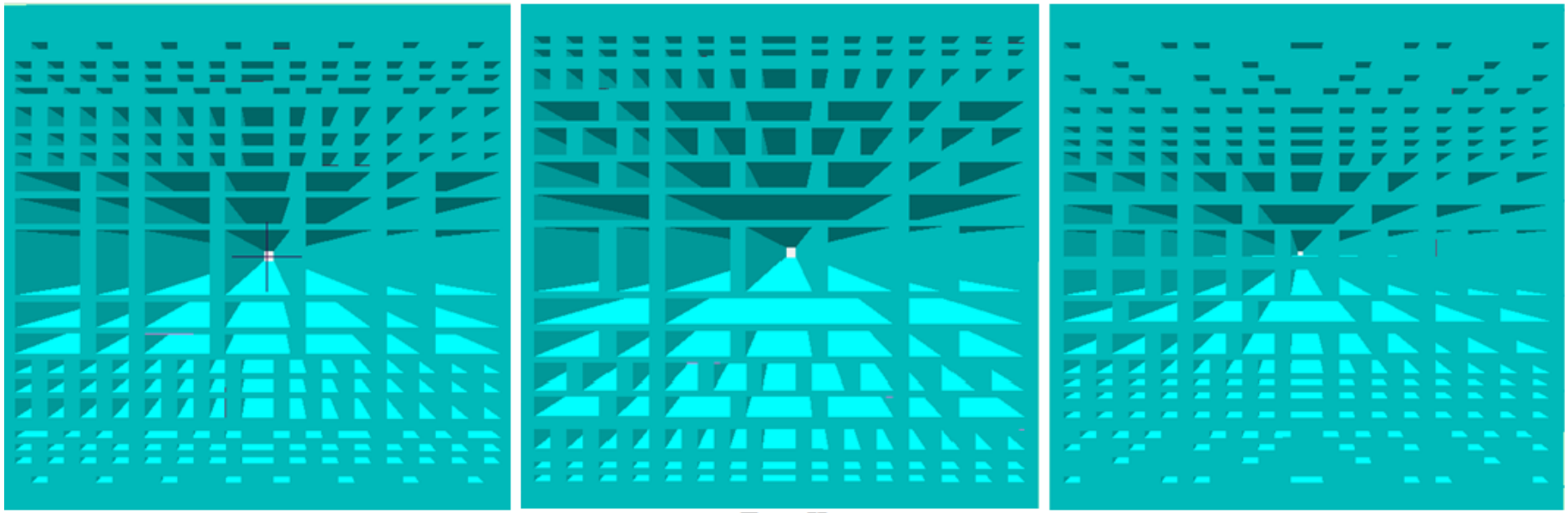

Fig. 37: A digital scheme of 3 types of the porosity gradients in the 3D printed samples –type I, type II and type III

5.2.3 Comparison of the uniform and the porosity gradient structure

Prepared samples had the same outer look regardless of their inner structure. The outer shell was always composed of the compact solid layers, and that was due to the parameters and options of the 3D print. Primary difference rest in the different porosity and the density of the samples, and, further, mechanical properties. A comparison of the uniform and the porosity gradient structures is graphically depicted in Fig. 38:, where the stress-strain curves show the primary difference in the mechanical response. Whereas no porosity samples (dark blue curves) and samples with the uniform porosity (red, brown, green and purple curves) show brittle character of the deformation, the porosity gradient structures (yellow, light blue and grey curves) completely changed the mechanical response of the samples with the same outer shape and the same material composing the samples. The gradient structures show the tough character of the deformation with significantly higher values of the deformation (around 7 % for the gradient 3, and 14-15 % for the gradients 1 and 2), although, lower values of the bending strength (table 8) were achieved. This proves that inner geometric structure of the prepared samples was of great importance regarding the mechanical properties. However, only different porosity does not make any difference in the mechanical response. The combination of the pores´ distribution, their size and shape caused different layout of the forces, and so the stress acting in the porosity gradient samples compared to the uniform porosity samples, thus resulting in different character of the deformation. The precise geometric composition of the pores in the sample, their shape and distribution are crucial, and, secondly, also the outer shape of the sample and the way of the mechanical loading. These various factors needs to be investigated to determine how exactly they influence each other.

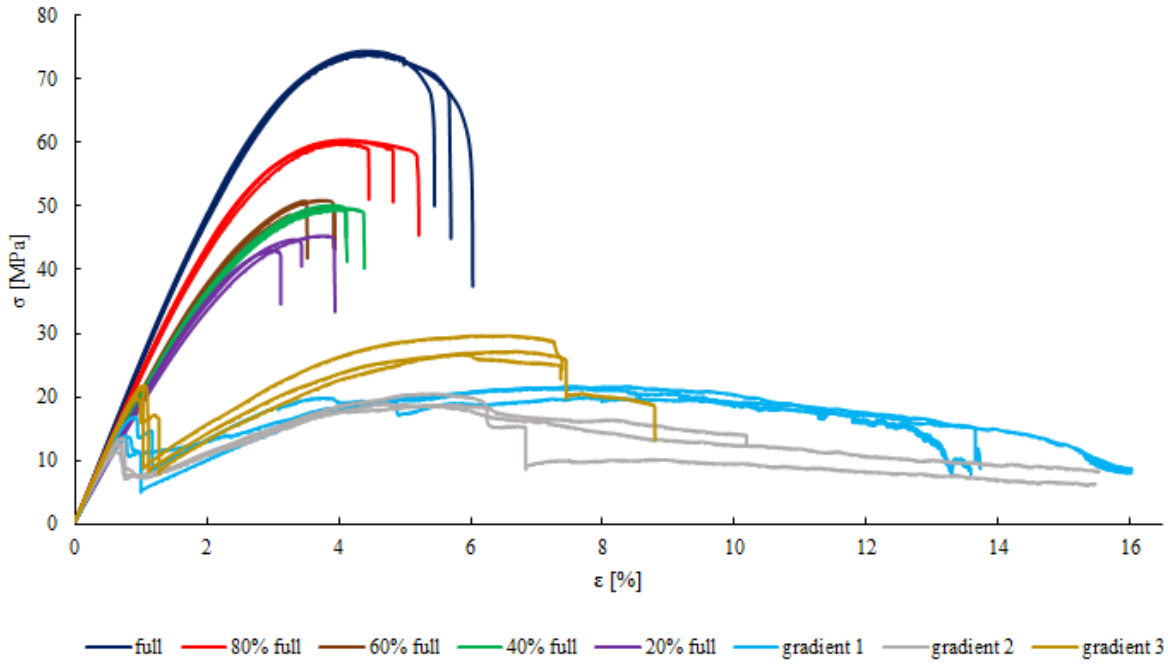

Fig. 38: Diagram of the stress-strain curves of the 3D printed samples with no porosity (full), uniform porosity (80% full, 60% full, 40 % full, 20% full) and porosity gradient (gradient 1, 2, 3); different character of deformation can be observed between porosity gradient samples and uniform porosity samples

The bending strength varied as expected for the compact solid sample and the uniform porosity samples. These samples deformation with brittle character show a decreasing trend in the values of the bending strength from the solid sample (74,040 MPa) to the samples with the highest uniform porosity (44,376 MPa). That is due to the introducing increased porosity into the samples. However, the bending strength for the porosity gradient structures is significantly lower compared to the

uniform porosity structures. The values are 21,001, 12,523 and 21,068 MPa for gradients 1,2 and 3, respectively. That is caused by different trend of the deformation and collapse of the cells. The gradient structure of the pores and their specific shape resulted in such bending of the cells and their rupture, that the ruptured cells contributed to the increase in the bending strength in plastic deformation region (Fig. 38:). However, Young´s modulus values lie in the range from the solid sample to the sample with the highest porosity (table 8).

5.2.4 Mechanical response of the notched samples

3-point bending test with notched samples was performed to determine the fracture toughness of the samples and to compare the bending strength and Young´s modulus of the samples with the notch and without the notch. In Fig. 39:, the stress-strain curves of the notched samples for no porosity samples (dark blue curves) and for the uniform porosity samples (red, green, light blue, purple curves) showed different response compared to the samples without the notch. The samples had a shorter region of elastic deformation and the fracture was not brittle, but tough. Also, the overall deformation was smaller, and the values of the bending strength and Young´s modulus were significantly lower (table 9) compared to the samples without the notch. These lower values were expected as the crack was inserted into the sample, thus reducing the strength of the entire structure. A similar decrease of Young´s modulus and the bending strength was recorded for the porosity gradient structures, too. The deformation range of the porosity gradient structures was smaller, but not significantly.

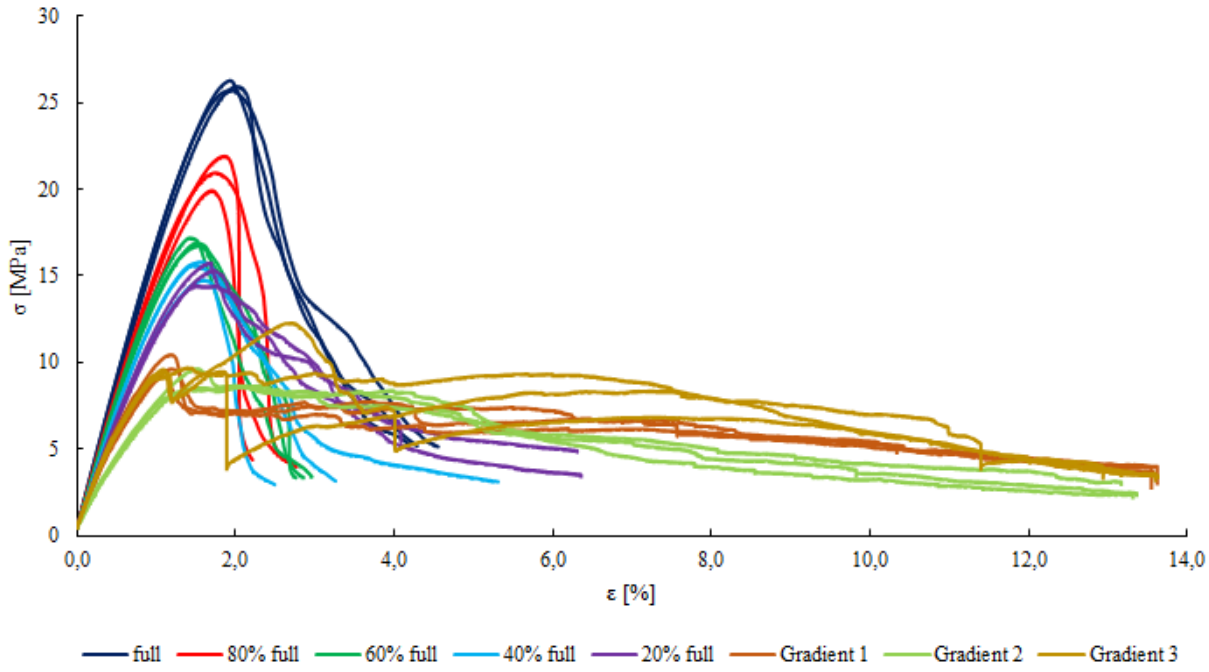

Fig. 39: Diagram of the stress-strain curves of the 3D printed notched samples with no porosity (full), uniform porosity (80% full, 60% full, 40% full, 20% full) and porosity gradient (gradient 1, 2, 3); different character of deformation can be observed between porosity gradient samples and uniform porosity samples

The values of the fracture toughness, K^*_{IC}, were calculated according to the eq. (9), where σ_{fs} is the stress at the break of the sample [MPa], and a is the depth of the notch [m], which was 3,6 mm. Values for the porosity gradient samples lie below the values of the porosity uniform samples. The porosity gradient samples reached values 0,3176, 0,2806 and 0,3574 MPa·m$^{1/2}$ for the gradient 1, 2 and 3, respectively. The lowest value was obtained for the porosity gradient sample with the lowest density (gradient 2). The highest fracture toughness´s value was obtained for the solid sample, and that was 0,5764 MPa·m$^{1/2}$. The fracture toughness´s values were rising from the highest porosity

sample to the non-porosity sample and this trend was expected because the increased porosity weakens the structure. However, because of the different character of the deformation of the porosity gradient samples, there were reached lower values.

In Fig. 40:, there are depicted deformation energies of all the measured 3D printed samples with a notch. There can be seen a decreasing trend from the compact sample (full) towards the samples with increasing porosity (80% full, 60% full). However, increasing deformation energy was observed for samples with the lowest values of porosity (40% full, 20% full). The biggest deformation energies were obtained for the porosity gradient samples (gradient 1, 2, 3). Despite lower values of the bending strength of the porosity gradient samples, they had much larger deformation area, which caused such high values of the deformation energies.

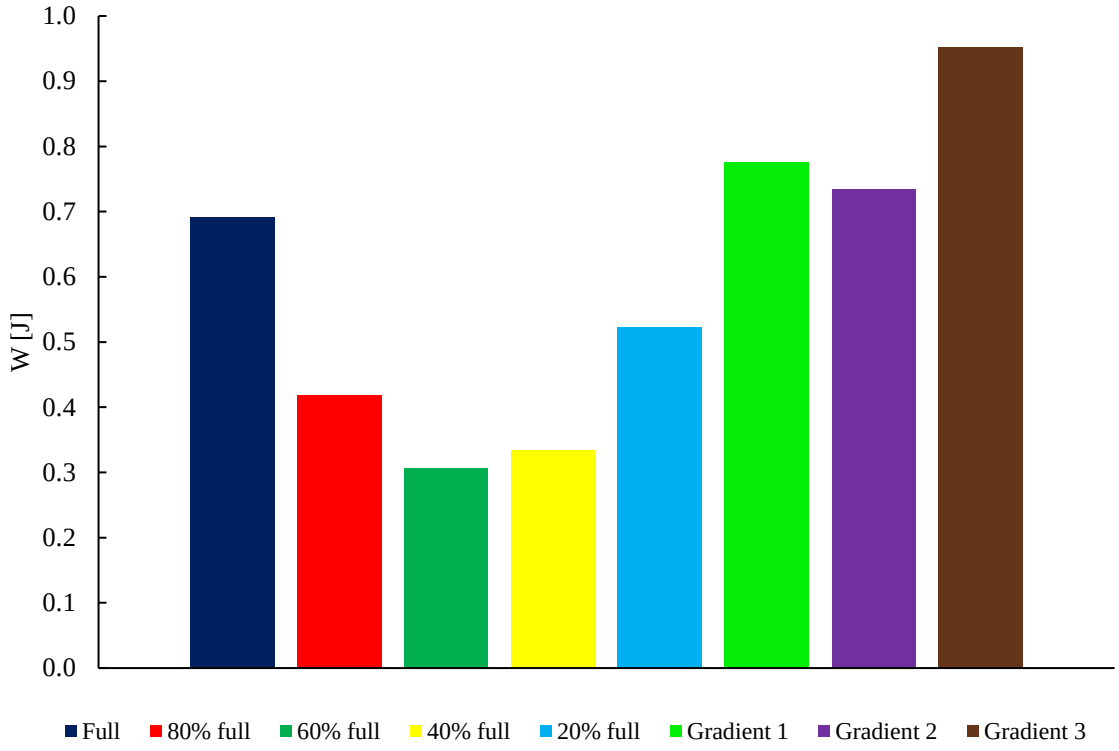

Fig. 40: Diagram of the deformation energies of the 3D printed samples without porosity (full), with uniform porosity (80% full, 60% full, 40% full, 20% full) and porosity gradient (gradient 1, 2, 3); the biggest values were achieved for porosity gradient structures; these are just averaged values obtained from 3-point bending measurements of the 3D printed notched samples

5.3 Comparison of the layered structure and the 3D structure

Essentially, both ways of preparing density gradient structure are by using the layering method, although there are differences. 3D print used the extruder head with a small diameter, which provided very precise layering, and, also, small and even thickness of each layer, whereas the layer-by-layer technique used simple casting of the layers, where the thickness of each layer was bigger and the dimensions were kept the same. Nevertheless, the pores could not be precisely manufactured, the delamination was hindered by casting layer on the top of the previous not completely polymerised layer. That secured good bonding of the layers together with the foaming in the drier, where partial melting of the material occurred. However, the delamination was quite a problem with the 3D samples, where mostly bottom layers were detached from the body. Precise control over the heatbed temperature of the 3D printer is necessary. Further delamination was observed during the 3-point bending test (Fig. 41:).

The 3D printing technique was able to secure precise pore distribution over the volume of the sample, which was also reproducible for every sample. The size of the pores was kept the same, too, and overall control over the manufacturing process was very good. Thanks to this, various density gradients could be designed and produced in comparison with the layer-by-layer technique. There could be controlled just the amount of the pores in the layer by varying the amount of the CBA dispersed in it. But other features, such as the distribution of the pores, their size or shape were stochastic. As was described above, the precise inner structure of the sample secures improved mechanical properties over the traditional ones with the uniform density. Since this was achieved for 3D samples, the mechanical response was improved only for this way of manufacturing the density gradient. Although, sufficiently smooth transfer between the layers with different amount of the CBA was achieved for the layer-by-layer technique.

Fig. 41: Photo of the delamination of the 3D printed sample during the 3-point bending test; red circle highlights the delamination spot

5.4 Comparison with theoretical models

Comparison with a theoretical model from Ashby and Gibson was performed to evaluate if our results were any improvement towards the model. This model is made for foams which deform primarily by edge bending, buckling and yielding, and the cubic cell is used to describe the deformation process with an assumption that foam cells are geometrically similar for different relative densities. As the pores in the prepared samples are not cubic (mainly the layer-by-layer samples), there will be a deflection of our results from the theoretical models. All points of measured data and gradient samples are averaged values from at least 3 measurements.

In the region of linear elasticity for open-cell foams with low density, the deformation proceeds primarily by bending of the cell edges under uniaxial stress, thus the eq. 7 for relative Young´s modulus is used where C_1 is the geometric constant experimentally settled for 1 and ρ^* is the relative density calculated as the ratio of the foam density to the density of the solid.

In Fig. 42:, there are depicted data from the theoretical model (dark blue dashed line), which show a linear trend. This was confirmed by measured data (green points), which values had an almost linear character (green spotted line) as shown by squared reliability coefficient (R^2 = 0,841). However, it is obvious that measured values are significantly bigger than values suggested by the theoretical model, mostly for lower relative densities. Even bigger values were achieved investigating porosity gradient structures (purple, yellow, red points). The porosity gradient structures varied in densities, and, also, in values of the relative Young´s modulus among themselves. These bigger values of the relative

Young´s modulus could be caused by the precise geometry of the samples, not just the outer shell, but mostly the inner structure. The highest values were obtained by gradient 3 (yellow point) with a slightly smaller/similar relative density as gradient 1 (red point).

The theoretical equation determined by Gibson-Ashby for three-point bending of foams is:

$$\frac{\sigma_f}{\sigma_s} = C_2 \cdot (\rho^*)^{3/2} \tag{14}$$

where σ_f and σ_s are bending strength of the foam and of the solid [MPa], respectively, and C_2 is a geometric constant experimentally settled for 0,18.

In Fig. 43:, there can be seen that measured values of the relative bending strength (green points) are significantly higher than the theoretical values (dark blue dashed line). However, the density gradient samples (red, purple and yellow points) did not achieve such superior values of the relative bending strength but remained above the values of the theoretical model. The highest value of the bending strength was reached by gradient 3 (yellow point) for the similar relative density as for the gradient 1 (red point).

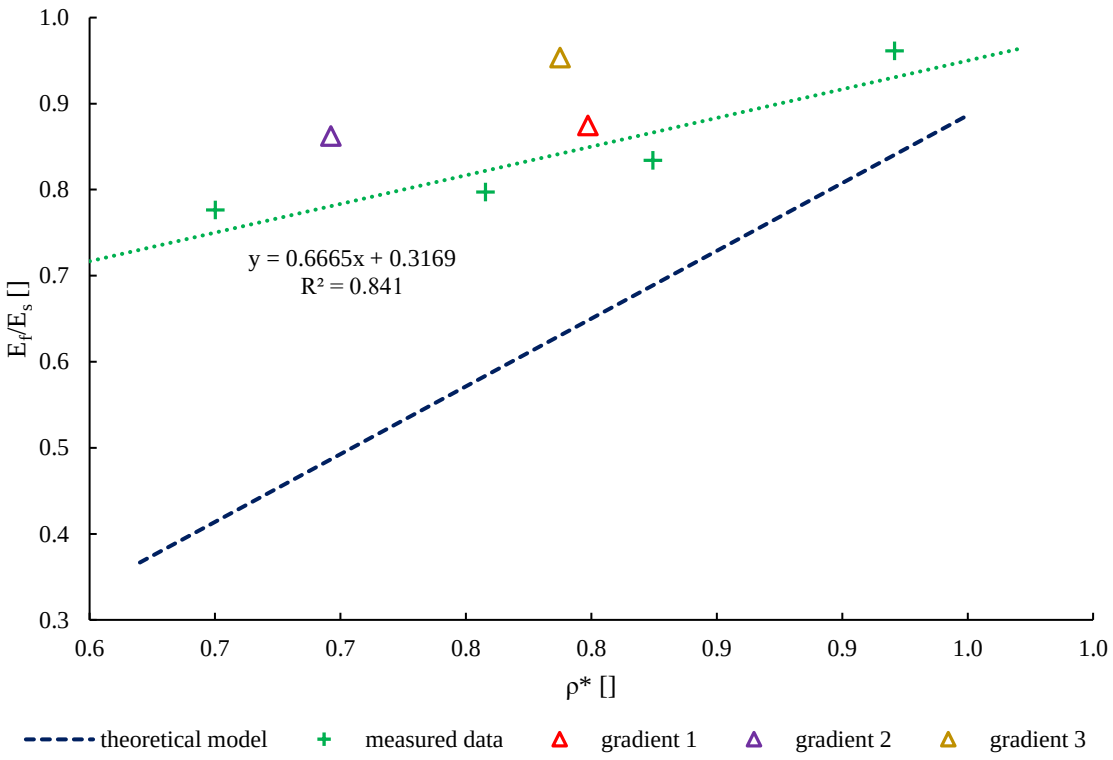

Fig. 42: Diagram of the relative Young´s modulus in respect with the relative density of the theoretical model´s data (dark blue dashed line), measured data (green points) and gradients values (purple, yellow, red points) of the 3D printed samples; all the measured values are averaged loaded with an error less than 4 %, so the error is included in the range of the points

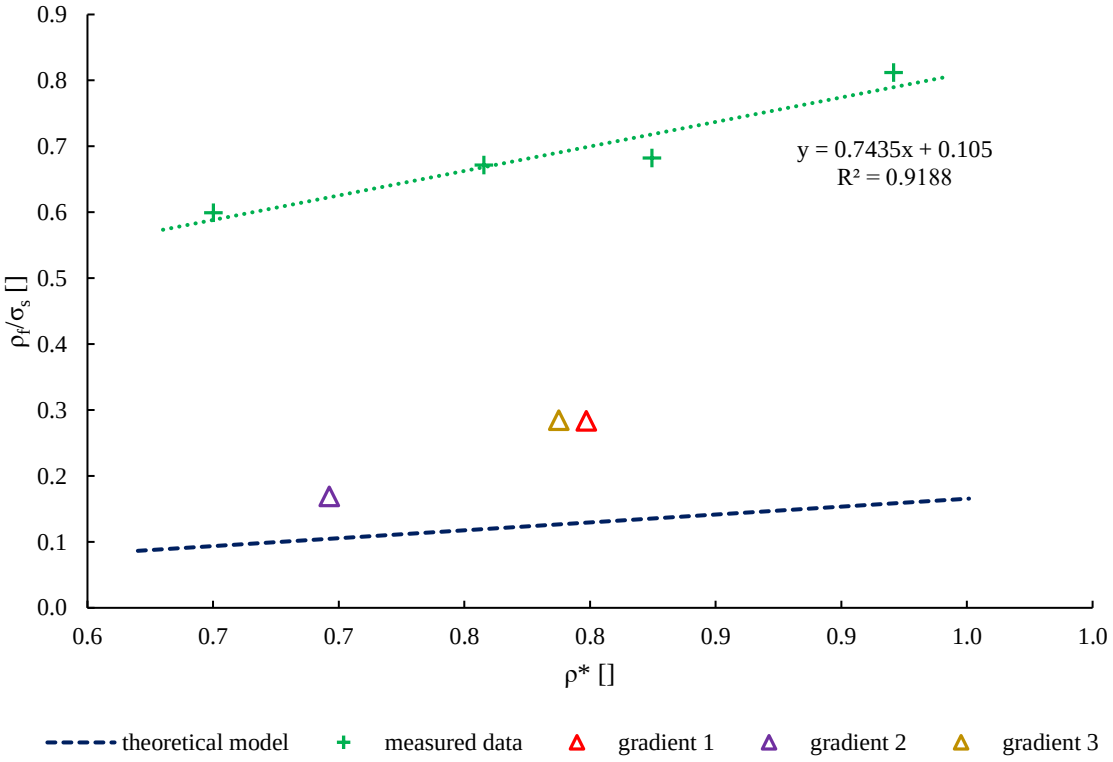

Fig. 43: Diagram of the relative bending strength in respect with the relative density of the theoretical model´s data (dark blue dashed line), measured data (green points) and gradients values (purple, yellow, red points) of the 3D printed structures; all the measured values are averaged loaded with an error less than 2 %, so the error is included in the range of the points

For the samples prepared by the layer-by-layer technique, it is obvious that the gradient structure did not achieve any improvement over the traditional uniform density samples (Fig. 44: and Fig. 45:, green points). When comparing with the theoretical model for the relative Young´s modulus (dark blue dashed line), the gradient structure achieved even worse results than the theoretical model (Fig. 44:). The equation used for calculating the theoretical model was eq. 7, where C_1 is experimentally settled for 1.

The equation for calculating the relative compressive strength determined by Gibson-Ashby is:

$$\frac{\sigma_{f,c}}{\sigma_{s,c}} = C_3 \cdot (\rho^*)^{3/2} \tag{15}$$

where $\sigma_{f,c}$ and $\sigma_{s,c}$ are the compressive strength of the foam and of the solid [MPa], respectively, and C_3 is a geometric constant experimentally settled for 0,3.

Comparing results to the theoretical model for compressive strength (dark blue dashed line), the value for density gradient samples (green point) lie slightly below the linear trend of the uniform density foams (red points) (Fig. 45:). This proves that a simple density gradient over the volume of the sample is not sufficient for creating improved mechanical properties. There is a need for creating a way of preparing samples with a controlled distribution of the pores, their shape, and, probably, also their amount. However, it is very difficult to achieve such control with the CBA, because the dispersion is always stochastic, and the size of the CBA clusters varies, too.

The last theoretical model used was for determining the relative fracture toughness (K^*_{IC}) according to the Gibson-Ashby equation:

$$\frac{K^*_{IC}}{\sigma_{fs} \cdot \sqrt{\pi \cdot l}} = C_4 \cdot (\rho^*)^{3/2} \tag{16}$$

where σ_{fs} is the modulus of rupture of the solid [MPa], l is the size of the cell, and C_4 is a geometric constant experimentally settled for 0,65.

The sizes of the cells were 4, 2, 1, and 0,5 mm for the uniform porosity samples with the infill of 20, 40, 60, and 80 %, respectively. For the gradient structures where sizes of the cells varied according to the layer, there were calculated the averaged size of the cells for each gradient type. The average size was calculated using the digital design depicted in Fig. 37:, where were counted the number of the pores and their diameter in each layer. Then, the weighted average was calculated, and this value was put in the eq. 16. The values of the cells' sizes were 0,3904, 0,5325, and 0,3347 for the porosity gradients 1, 2, and 3, respectively. It is obvious that the sizes of the cells of the uniform porosity samples are higher than of the porosity gradient samples, thus resulting in lower values of the relative fracture toughness. In Fig. 46:, there can be seen a theoretical model (dark blue dashed line), which lies below the measured data (green points). The measured data had a different trend than the theoretical model, probably caused by different shape of the cells. The values of the porosity gradient structures (purple, yellow, red points) lie above the measured data of the uniform porosity samples, which was caused by the specific inner geometry of the samples.

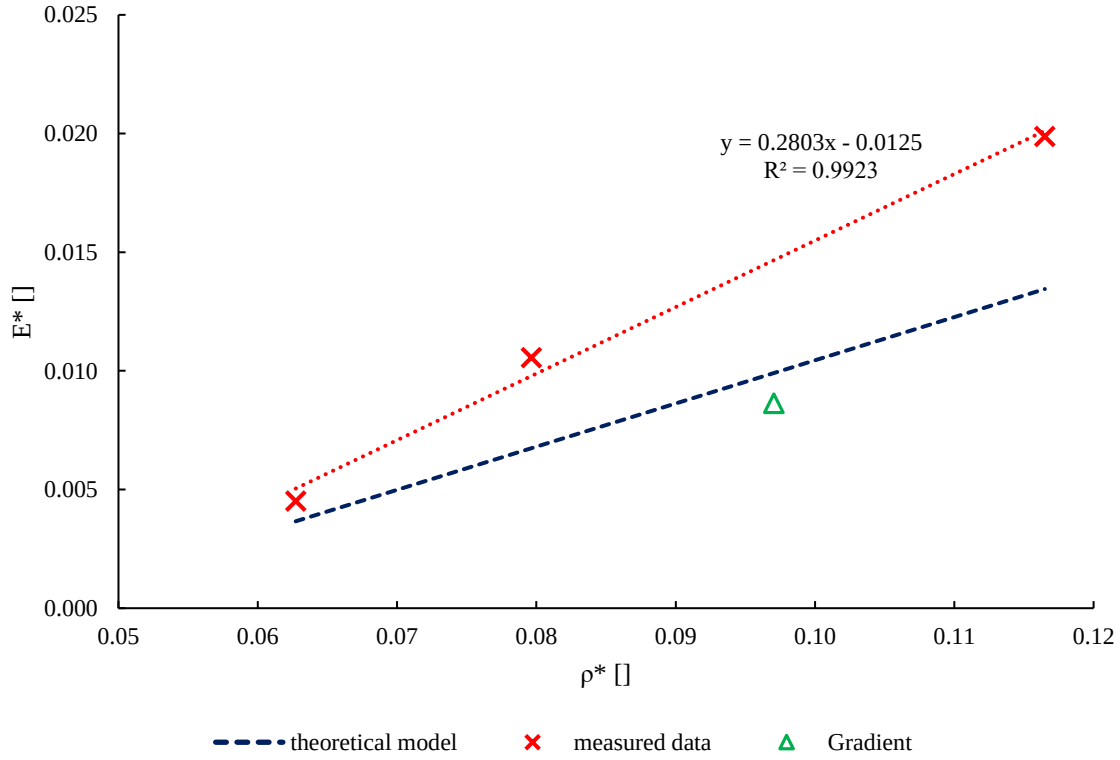

Fig. 44: Diagram of the relative Young´s modulus in respect with the relative density of the theoretical model´s data (dark blue dashed line), measured data (red points) and density gradient sample (green point) of the PMMA foams; all the measured values are averaged loaded with an error less than 2 %, so the error is included in the range of the points

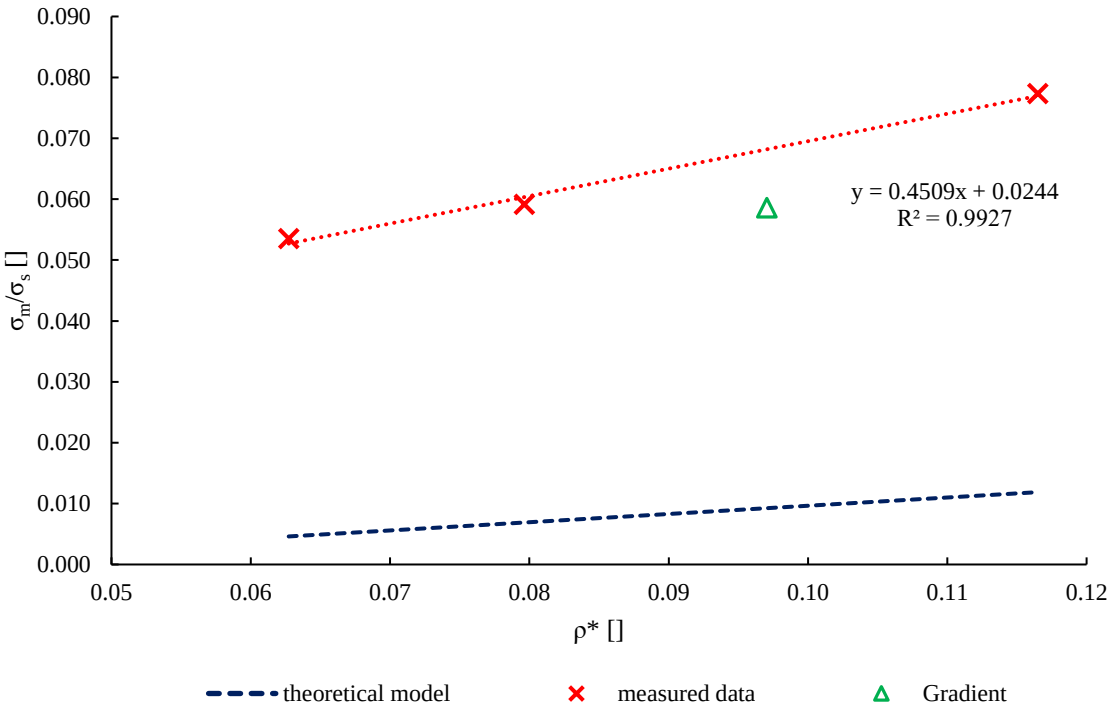

Fig. 45: Diagram of the relative compressive strength in respect with the relative density of the theoretical model´s data (dark blue dashed line), measured data (red points) and density gradient sample (green point) of the PMMA foams; all the measured values are averaged loaded with an error less than 2 %, so the error is included in the range of the points

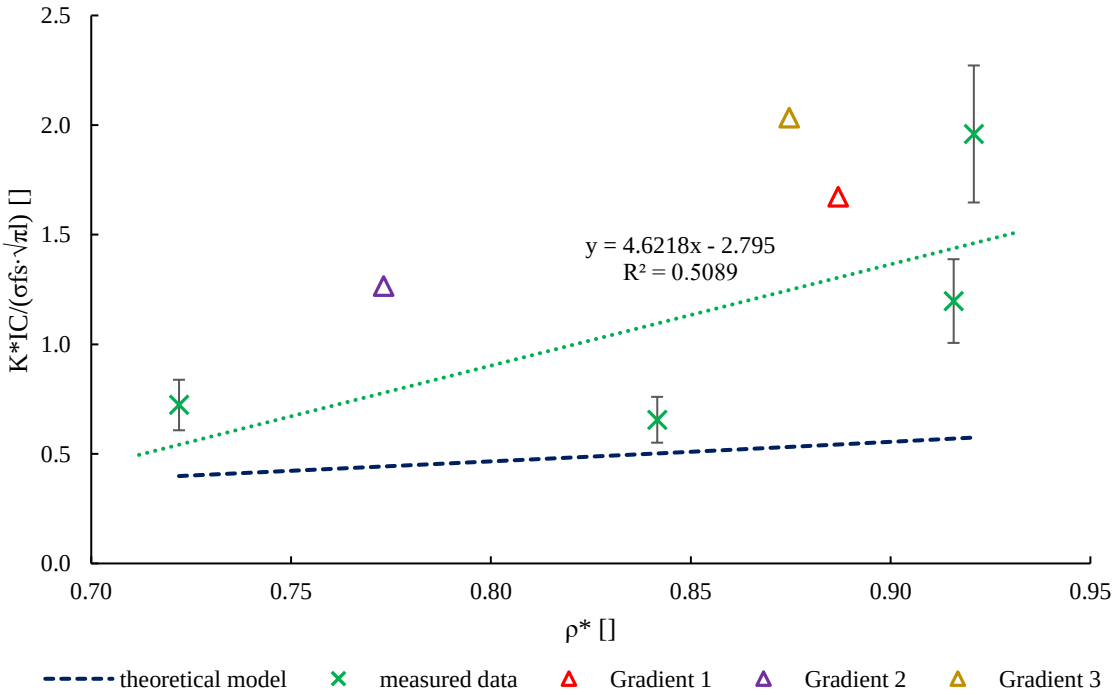

Fig. 46: Diagram of the relative fracture toughness in respect with the relative density of the theoretical model´s data (dark blue dashed line), measured data (green points) and gradient values (purple, yellow, red points) of the 3D printed samples with the notch; all the measured values are averaged and the gradients sample are loaded with an error of 16 %

6 CONCLUSION

For PMMA foams with porosity gradient prepared by laminating technique, no improvement of the mechanical properties over homogenous porosity foams was observed. The predicted moduli and strength based on the existing theoretical models were always greater than those for the gradient porosity PMMA foams. The observed discrepancies were ascribed to the stochastic pores´ distribution and irregular shape of the pores.

3D printed gradient porosity cellular materials exhibited deformation behaviour differing from that observed for the uniform porosity foams substantially. Unlike the laminated porosity gradient foams, 3D printed cellular materials with porosity gradient exhibited greater relative Young´s modulus and relative fracture toughness than predicted using simple Ashby-Gibson models. The observed behaviour was ascribed to the more precise pore geometry, more regular size and their spatial distribution and number. Our results provides starting point for further investigation of the cellular materials with controlled porosity gradient intended for application in lightweight engineering components.

7 BIBLIOGRAPHY

[1] ELSING, Jonas, Aggeliki QUELL a Cosima STUBENRAUCH. Toward Functionally Graded Polymer Foams Using Microfluidics. *Advanced Engineering Materials* [online]. 2017, **19**(8) [cit. 2019-02-21]. DOI: 10.1002/adem.201700195. ISSN 14381656. Dostupné z: http://doi.wiley.com/10.1002/adem.201700195

[2] SAUCEAU, Martial, Jacques FAGES, Audrey COMMON, Clémence NIKITINE a Elisabeth RODIER. New challenges in polymer foaming: A review of extrusion processes assisted by supercritical carbon dioxide. *Progress in Polymer Science* [online]. 2011, **36**(6), 749-766 [cit. 2019-02-21]. DOI: 10.1016/j.progpolymsci.2010.12.004. ISSN 00796700. Dostupné z: https://linkinghub.elsevier.com/retrieve/pii/S0079670010001280

[3] YOO, C.J., B.S. SHIN, B.S. KANG, C.Y. GWAK, C. PARK, Y.W. MA a S.M. HONG. A Study on a New 3D Porous Polymer Printing Based on EPP Beads Containing CO 2 Gas. *Procedia Engineering* [online]. 2017, **184**, 10-15 [cit. 2019-02-20]. DOI: 10.1016/j.proeng.2017.04.064. ISSN 18777058. Dostupné z: https://linkinghub.elsevier.com/retrieve/pii/S1877705817315692

[4] ESMAILZADEH, Mojtaba, Habib DANESH MANESH a S. Mojtaba ZEBARJAD. Fabrication and characterization of functional graded polyurethane foam (FGPUF). *Polymers for Advanced Technologies* [online]. 2018, **29**(1), 182-189 [cit. 2019-02-20]. DOI: 10.1002/pat.4100. ISSN 10427147. Dostupné z: http://doi.wiley.com/10.1002/pat.4100

[5] GIBSON, Lorna J., M. F. ASHBY a Brendan A. HARLEY. *Cellular materials in nature and medicine*. First. New York: Cambridge University Press, 2010. ISBN 978-0-521-19544-7.

[6] WU, Dingcai, Fei XU, Bin SUN, Ruowen FU, Hongkun HE a Krzysztof MATYJASZEWSKI. Design and Preparation of Porous Polymers. *Chemical Reviews* [online]. 2012, **112**(7), 3959-4015 [cit. 2019-02-18]. DOI: 10.1021/cr200440z. ISSN 0009-2665. Dostupné z: http://pubs.acs.org/doi/10.1021/cr200440z

[7] KOOHBOR, Behrad a Addis KIDANE. Design optimization of continuously and discretely graded foam materials for efficient energy absorption. *ScienceDirect* [online]. 2016, **102**, 151-161 [cit. 2019-05-04]. DOI: 10.1016/j.matdes.2016.04.031. ISSN 02641275. Dostupné z: https://linkinghub.elsevier.com/retrieve/pii/S0264127516304981

[8] CUI, Liang, Stephen KIERNAN a Michael D. GILCHRIST. Designing the energy absorption capacity of functionally graded foam materials. *Materials Science and Engineering: A* [online]. 2009, **507**(1-2), 215-225 [cit. 2019-05-04]. DOI: 10.1016/j.msea.2008.12.011. ISSN 09215093. Dostupné z: https://linkinghub.elsevier.com/retrieve/pii/S0921509308013646

[9] KITAGAWA, Susumu. Future Porous Materials. *Accounts of Chemical Research* [online]. 2017, **50**(3), 514-516 [cit. 2019-05-04]. DOI: 10.1021/acs.accounts.6b00500. ISSN 0001-4842. Dostupné z: http://pubs.acs.org/doi/10.1021/acs.accounts.6b00500

[10] MIAO, Xigeng a Dan SUN. Graded/Gradient Porous Biomaterials. *Materials* [online]. 2010, **3**(1), 26-47 [cit. 2019-01-30]. DOI: 10.3390/ma3010026. ISSN 1996-1944. Dostupné z: http://www.mdpi.com/1996-1944/3/1/26

[11] KHEMANI, Kishan C. Polymeric Foams: An Overview. *Polymeric Foams* [online]. Washington, DC: American Chemical Society, 1997, , 1-7 [cit. 2019-01-18]. ACS Symposium

Series. DOI: 10.1021/bk-1997-0669.ch001. ISBN 0-8412-3516-3. Dostupné z: http://pubs.acs.org/doi/abs/10.1021/bk-1997-0669.ch001

[12] ALTAN, Mihrigul. Thermoplastic Foams: Processing, Manufacturing, and Characterization. *Recent Research in Polymerization* [online]. InTech, 2018 [cit. 2019-01-18]. DOI: 10.5772/intechopen.71083. ISBN 978-953-51-3746-7. Dostupné z: http://www.intechopen.com/books/recent-research-in-polymerization/thermoplastic-foams-processing-manufacturing-and-characterization

[13] LEE, L, C ZENG, X CAO, X HAN, J SHEN a G XU. Polymer nanocomposite foams. *Composites Science and Technology* [online]. 2005, **65**(15-16), 2344-2363 [cit. 2019-01-20]. DOI: 10.1016/j.compscitech.2005.06.016. ISSN 02663538. Dostupné z: http://linkinghub.elsevier.com/retrieve/pii/S0266353805002253

[14] NVH – What are porous materials and how are they related to automotive applications?. *Simulating Reality, Delivering Certainty* [online]. 2013 [cit. 2019-02-27]. Dostupné z: http://simulatemore.mscsoftware.com/nastran-nvh-what-are-porous-materials-and-how-are-they-related-to-automotive-applications/

[15] A new introduction to Chemical Blowing Agents. *A new introduction to Chemical Blowing Agents* [online]. Houston, Texas: REEDY, 2017 [cit. 2019-01-22]. Dostupné z: https://etouches-appfiles.s3.amazonaws.com/html_file_uploads/885d8cddaedb03c6613d0bc2fd7bc498_schroeck.pdf?response-content-disposition=inline%3Bfilename%3D%22schroeck.pdf%22&response-content-type=application%2Fpdf&AWSAccessKeyId=AKIAJC6CRYNXDRDHQCUQ&Expires=1548004066&Signature=V2AAYqa2KMv2GmRXSLTj6UTyvqM%3D

[16] Blowing agents. *Urethans Technology International* [online]. London: Simon Robinson, 2013 [cit. 2019-01-22]. Dostupné z: https://utech-polyurethane.com/post_glossary/blowing-agents/

[17] EAVES, David. *Handbook of polymer foams*. Shawbury, Shrewsbury, Shropshire, U.K.: Rapra Technology, 2004. ISBN 18-595-7388-6.

[18] ZHANG, Hongtao. *Scale-Up of Extrusion Foaming Process for Manufacture of Polystyrene Foams Using Carbon Dioxide*. Toronto, 2010. Master thesis. University of Toronto.

[19] REGLERO RUIZ, José Antonio, Michel VINCENT, Jean-François AGASSANT, Tarik SADIK, Caroline PILLON a Christian CARROT. Polymer foaming with chemical blowing agents: Experiment and modeling. *The open archive HAL* [online]. 2015, **55**(9), 2018-2029 [cit. 2019-02-20]. DOI: 10.1002/pen.24044. ISSN 00323888. Dostupné z: http://doi.wiley.com/10.1002/pen.24044

[20] DRENCKHAN, Wiebke a Arnaud SAINT-JALMES. The science of foaming. *Advances in Colloid and Interface Science* [online]. 2015, **222**, 228-259 [cit. 2019-02-22]. DOI: 10.1016/j.cis.2015.04.001. ISSN 00018686. Dostupné z: https://linkinghub.elsevier.com/retrieve/pii/S0001868615000603

[21] GIBSON, Lorna J. Biomechanics of cellular solids. *Journal of Biomechanics* [online]. 2005, **38**(3), 377-399 [cit. 2019-01-22]. DOI: 10.1016/j.jbiomech.2004.09.027. ISSN 00219290. Dostupné z: http://linkinghub.elsevier.com/retrieve/pii/S0021929004004919

[22] GUPTA, Nikhil. A functionally graded syntactic foam material for high energy absorption under compression. *Materials Letters* [online]. 2007, **61**(4-5), 979-982 [cit. 2019-01-30]. DOI:

10.1016/j.matlet.2006.06.033. ISSN 0167577X. Dostupné z: https://linkinghub.elsevier.com/retrieve/pii/S0167577X06007270

[23] POLLARD, Thomas D., William C. EARNSHAW, Jennifer LIPPINCOTT-SCHWARTZ a Graham T. JOHNSON. *Cell biology: p. 540, fig. 34-4*. Third edition. Philadelphia, PA: Elsevier, 2017. ISBN 978-032-3341-264.

[24] Acoustic Damping using Polyurethane/Polymer Composites: Analysis of Polyurethane Foam. *APPROPEDIA* [online]. California, 2015 [cit. 2019-02-19]. Dostupné z: http://www.appropedia.org/Acoustic_Damping_using_Polyurethane/Polymer_Composites

[25] A Cost Effective Alternative for Polyurethane Foams: slide 22. *Slide player* [online]. b.r. [cit. 2019-02-19]. Dostupné z: https://slideplayer.com/slide/13899393/

[26] GUPTA, V. K. a D. V. KHAKHAR. Formation of integral skin polyurethane foams. *Polymer engineering and science* [online]. 1999, **39**(1), 164-176 [cit. 2019-01-30]. Dostupné z: https://onlinelibrary.wiley.com/doi/pdf/10.1002/pen.11405

[27] MLEZIVA, Josef. *Polymery - výroba, struktura, vlastnosti a použití*. 2. přepr. vyd. Praha: Sobotáles, 2000. ISBN 80-859-2072-7.

[28] Properties, Performance and Design Fundamentals of Expanded Polystyrene Packaging. *EPS industry* [online]. Crofton: EPS Industry Alliance, 2016 [cit. 2019-01-30]. Dostupné z: https://www.epsindustry.org/sites/default/files/-Properties%2C%20Performance%20and%20Design%20Fundamentals%20of%20Expanded%20Polystyrene%20Packaging.pdf

[29] NOTARIO, B., J. PINTO a M.A. RODRÍGUEZ-PÉREZ. Towards a new generation of polymeric foams: PMMA nanocellular foams with enhanced physical properties. *Polymer* [online]. 2015, **63**, 116-126 [cit. 2019-02-04]. DOI: 10.1016/j.polymer.2015.03.003. ISSN 00323861. Dostupné z: https://linkinghub.elsevier.com/retrieve/pii/S0032386115002311

[30] PINTO, Javier, Davide MORSELLI, Victoria BERNARDO, Belen NOTARIO, Despina FRAGOULI, Miguel Angel RODRIGUEZ-PEREZ a Athanassia ATHANASSIOU. Nanoporous PMMA foams with templated pore size obtained by localized in situ synthesis of nanoparticles and CO 2 foaming. *Polymer* [online]. 2017, **124**, 176-185 [cit. 2019-02-05]. DOI: 10.1016/j.polymer.2017.07.067. ISSN 00323861. Dostupné z: https://linkinghub.elsevier.com/retrieve/pii/S0032386117307425

[31] Open cell foam. *Foam Fabricating* [online]. b.r. [cit. 2019-02-19]. Dostupné z: https://www.foamfabricating.net/open-cell-foam/

[32] Open Cell vs. Closed Cell Foam: What's the Difference?. *CGR products* [online]. Greensboro, NC: Chuck Keeley, 2017 [cit. 2019-02-19]. Dostupné z: https://www.cgrproducts.com/open-cell-vs-closed-cell-foam/

[33] *Characterization of polymeric foams* [online]. Eindhoven: University of Technology, 2009 [cit. 2019-02-04]. Dostupné z: http://www.mate.tue.nl/mate/pdfs/10702_sec.pdf

[34] KRÄNZLIN, Niklaus a Markus NIEDERBERGER. Controlled fabrication of porous metals from the nanometer to the macroscopic scale. *Materials Horizons* [online]. 2015, **2**(4), 359-377 [cit. 2019-02-21]. DOI: 10.1039/C4MH00244J. ISSN 2051-6347. Dostupné z: http://xlink.rsc.org/?DOI=C4MH00244J

[35] SUN, Guangyong, Guangyao LI, Shujuan HOU, Shiwei ZHOU, Wei LI a Qing LI. Crashworthiness design for functionally graded foam-filled thin-walled structures. *Materials Science and Engineering: A* [online]. 2010, **527**(7-8), 1911-1919 [cit. 2019-02-05]. DOI: 10.1016/j.msea.2009.11.022. ISSN 09215093. Dostupné z: https://linkinghub.elsevier.com/retrieve/pii/S0921509309012234

[36] JOHN, Bibin a C.P. REGHUNADHAN NAIR. Syntactic Foams. *Handbook of Thermoset Plastics* [online]. Elsevier, 2014, , 511-554 [cit. 2019-01-30]. DOI: 10.1016/B978-1-4557-3107-7.00013-0. ISBN 9781455731077. Dostupné z: https://linkinghub.elsevier.com/retrieve/pii/B9781455731077000130

[37] GUPTA, Nikhil, Dung D. LUONG a Kyu CHO. Magnesium Matrix Composite Foams—Density, Mechanical Properties, and Applications. *Metals* [online]. 2012, **2**(3), 238-252 [cit. 2019-02-05]. DOI: 10.3390/met2030238. ISSN 2075-4701. Dostupné z: http://www.mdpi.com/2075-4701/2/3/238

[38] GUPTA, Nikhil, Steven E. ZELTMANN, Vasanth Chakravarthy SHUNMUGASAMY a Dinesh PINISETTY. Applications of Polymer Matrix Syntactic Foams. *JOM* [online]. 2014, **66**(2), 245-254 [cit. 2019-01-30]. DOI: 10.1007/s11837-013-0796-8. ISSN 1047-4838. Dostupné z: http://link.springer.com/10.1007/s11837-013-0796-8

[39] RIBEIRO-AYEH, Steven. *Finite element modelling of the mechanics of solid foam materials*. Stockholm, 2005. Doctoral thesis. Kungliga Tekniska Hogskolan.

[40] POTLURI., Rakesh., A. ESWARA KUMAR, M. NAGA RAJU a K. Ravi Prakash BABU. Finite Element Analysis ofCellular Foam Core Sandwich Structures. *Materials Today: Proceedings* [online]. 2017, **4**(2), 2501-2510 [cit. 2019-02-21]. DOI: 10.1016/j.matpr.2017.02.103. ISSN 22147853. Dostupné z: https://linkinghub.elsevier.com/retrieve/pii/S2214785317303012

[41] Cellular Solids: Structure, Properties and Applications. *The Gibson group* [online]. Cambridge: The Gibson group, b.r. [cit. 2019-02-21]. Dostupné z: http://lornagibson.org/research

[42] Research and Application of 3D Printed Porous Geometric Structure: a Review. *Materials Reports* [online]. 2018, **32**(15), 2672-2683 [cit. 2019-02-20]. Dostupné z: http://www.mr-int.net/EN/10.11896/j.issn.1005-023X.2018.15.020

[43] BUJ-CORRAL, Irene, Ali BAGHERI a Oriol PETIT-ROJO. 3D Printing of Porous Scaffolds with Controlled Porosity and Pore Size Values. *Materials* [online]. 2018, **11**(9) [cit. 2019-02-20]. DOI: 10.3390/ma11091532. ISSN 1996-1944. Dostupné z: http://www.mdpi.com/1996-1944/11/9/1532

[44] LIU, Wenjie, Jianping ZHOU, Yuming MA, Jie WANG a Jie XU. Fabrication of PLA Filaments and its Printable Performance. *IOP Conference Series: Materials Science and Engineering* [online]. 2017, **275** [cit. 2019-02-22]. DOI: 10.1088/1757-899X/275/1/012033. ISSN 1757-8981. Dostupné z: http://stacks.iop.org/1757-899X/275/i=1/a=012033?key=crossref.7509eaf37596914ebfc15c2238238c84

[45] SVATÍK, Juraj. *Štúdium prípravy expandovanej poly(kyseliny mliečnej)*. Brno, 2017. Bachelor thesis. Brno University of technology, Faculty of chemistry. Vedoucí práce Ing. Silvestr Figalla.

[46] WANG, Hong Juan, Min Zhi RONG, Ming Qiu ZHANG, Jing HU, Hui Wen CHEN a Tibor CZIGÁNY. Biodegradable Foam Plastics Based on Castor Oil. *Biomacromolecules* [online].

2008, **9**(2), 615-623 [cit. 2019-02-20]. DOI: 10.1021/bm7009152. ISSN 1525-7797. Dostupné z: http://pubs.acs.org/doi/abs/10.1021/bm7009152

[47] MARRAZZO, Carlo, Ernesto Di MAIO a Salvatore IANNACE. Foaming of Synthetic and Natural Biodegradable Polymers. *Journal of Cellular Plastics* [online]. 2016, **43**(2), 123-133 [cit. 2019-02-20]. DOI: 10.1177/0021955X06073214. ISSN 0021-955X. Dostupné z: http://journals.sagepub.com/doi/10.1177/0021955X06073214

[48] LIAO, Xia, Haichen ZHANG a Ting HE. Preparation of Porous Biodegradable Polymer and Its Nanocomposites by Supercritical CO 2 Foaming for Tissue Engineering. *Journal of Nanomaterials* [online]. 2012, **2012**, 1-12 [cit. 2019-02-20]. DOI: 10.1155/2012/836394. ISSN 1687-4110. Dostupné z: http://www.hindawi.com/journals/jnm/2012/836394/

[49] SIVERTSEN, Katrine. *Polymer foams: Biodegradable foams* [online]. 2007 [cit. 2019-02-20]. Dostupné z: https://ocw.mit.edu/courses/materials-science-and-engineering/3-063-polymer-physics-spring-2007/assignments/polymer_foams.pdf

[50] QIN, Yi-Xian, Wei LIN, Erik MITTRA, Yi XIA, Jiqi CHENG, Stefan JUDEX, Clint RUBIN a Ralph MÜLLER. Prediction of trabecular bone qualitative properties using scanning quantitative ultrasound. *Acta Astronautica* [online]. 2013, **92**(1), 79-88 [cit. 2019-02-04]. DOI: 10.1016/j.actaastro.2012.08.032. ISSN 00945765. Dostupné z: https://linkinghub.elsevier.com/retrieve/pii/S0094576512003426

[51] Honeycomb structure 3D print model. *CGTrader - 3D content made easy* [online]. Vilnius: CGTrader, b.r. [cit. 2019-02-04]. Dostupné z: https://www.cgtrader.com/3d-print-models/science/engineering/honeycomb-structure

[52] *Modelling of the mechanical properties of low-density foams* [online]. Delft University of Technology: Shaker Publishing B.V., 1997 [cit. 2019-02-20]. ISBN 90-423-0025-6. Dostupné z: http://citeseerx.ist.psu.edu/viewdoc/download?doi=10.1.1.849.986&rep=rep1&type=pdf

[53] EBEWELE, Robert Oboigbaotor. *Polymer science and technology*. First. Boca Raton: CRC Press, 2000. ISBN 08-493-8939-9.

[54] Chemical foam extrusion processing guide. *Bergen international* [online]. NJ, b.r. [cit. 2019-02-05]. Dostupné z: http://www.bergeninternational.com/files/Extrusion_Processing_Guide.pdf

[55] Thermoplastic Foam Injection Molding. *Plasticportal.eu* [online]. Nitra: KUBOUŠEK s.r.o., 2014 [cit. 2019-02-05]. Dostupné z: https://www.plasticportal.eu/en/thermoplastic-foam-injection-molding/c/2416/

[56] Structural foam injection molding process. *Wilmington machinery* [online]. Wilmington, NC, 2010 [cit. 2019-02-19]. Dostupné z: http://www.wilmingtonmachinery.com/structural-foam-injection-molding-process/

[57] LI, W L, K LU a J Y WALZ. Freeze casting of porous materials: review of critical factors in microstructure evolution. *International Materials Reviews* [online]. 2013, **57**(1), 37-60 [cit. 2019-02-15]. DOI: 10.1179/1743280411Y.0000000011. ISSN 0950-6608. Dostupné z: http://www.tandfonline.com/doi/full/10.1179/1743280411Y.0000000011

[58] SCOTTI, Kristen L. a David C. DUNAND. Freeze casting – A review of processing, microstructure and properties via the open data repository, FreezeCasting.net. *Progress in Materials Science* [online]. 2018, **94**, 243-305 [cit. 2019-02-15]. DOI:

10.1016/j.pmatsci.2018.01.001. ISSN 00796425. Dostupné z: https://linkinghub.elsevier.com/retrieve/pii/S007964251830001X

[59] Dentacryl technický. *Nejlevnejší barvy laky.cz* [online]. Praha, b.r. [cit. 2019-02-26]. Dostupné z: https://www.nejlevnejsi-barvy-laky.cz/dentacryl-technicky-bezbarva-souprava-100-g?utm_source=google&utm_medium=shopping&gclid=Cj0KCQiAwc7jBRD8ARIsAKSUBHI0fU86-b-4ydpOyEarHoC3F5BlQI5Q9Cfks6plBu94JXOIp0jZQY8aAm48EALw_wcB

[60] UNICELL-D Series. *UNICELL-D Series* [online]. b.r. [cit. 2019-02-26]. Dostupné z: https://www.dongjin.com/file/file_1.pdf

[61] JANČÁŘ, Josef a Eva NEZBEDOVÁ. *Zkoušení plastů*. First. Brno: Vysoké učení technické, 2007. ISBN 978-80-214-3452-3.

[62] KMETTY, Ákos, Katalin LITAUSZKI a Dániel RÉTI. Characterization of Different Chemical Blowing Agents and Their Applicability to Produce Poly(Lactic Acid) Foams by Extrusion. *Applied Sciences* [online]. 2018, **8**(10) [cit. 2019-04-09]. DOI: 10.3390/app8101960. ISSN 2076-3417. Dostupné z: http://www.mdpi.com/2076-3417/8/10/1960

8 LIST OF ABBREVIATIONS

ABS	acrylo-butadiene styrene
CBA	chemical blowing agent
CLSM	confocal laser scanning microscopy
DSC	differential scanning calorimetry
EMI	electromagnetic
EPDM	ethylene propylene diene monomer
EPS	expanded polystyrene
FDM	fused deposition modelling
FGFs	functionally graded/gradient foams
FIM	foam injection moulding
H_m	heat of melting
H_r	heat of recrystallization
MFI	melt flow index
MOFs	metal organic frameworks
NBR	nitrile rubber/acrylonitrile butadiene rubber
OM	optical microscopy
PBA	physical blowing agent
PLA	polylactic acid
PMMA	poly(methyl methacrylate)
PS	polystyrene
PUR	polyurethane
PVC	polyvinylchloride
SC-CO_2	supercritical carbon dioxide
SEM	scanning electron microscopy
T_g	glass transition temperature
TGA	thermogravimetric analysis
T_m	melting temperature
T_r	recrystallization temperature

9 APPENDIX

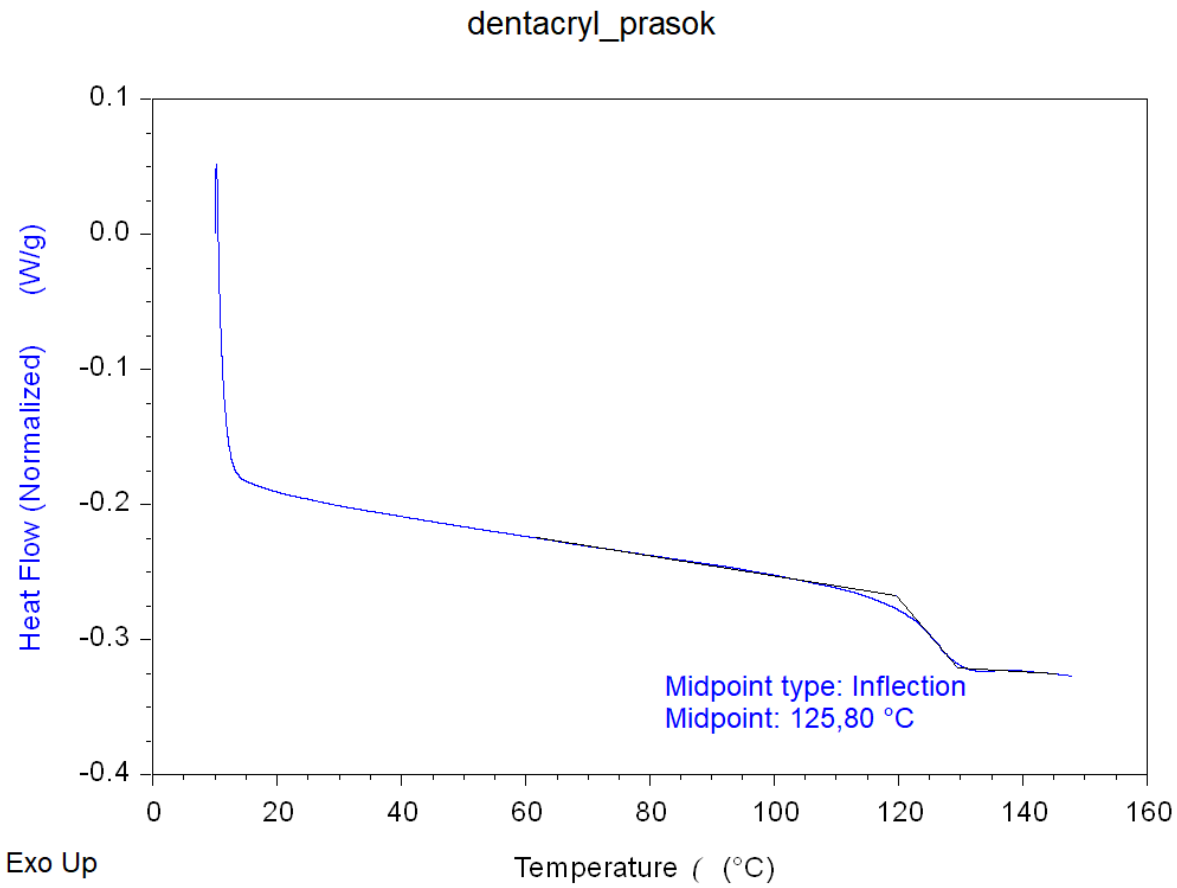

Fig. 47: DSC curve of Dentacryl powder

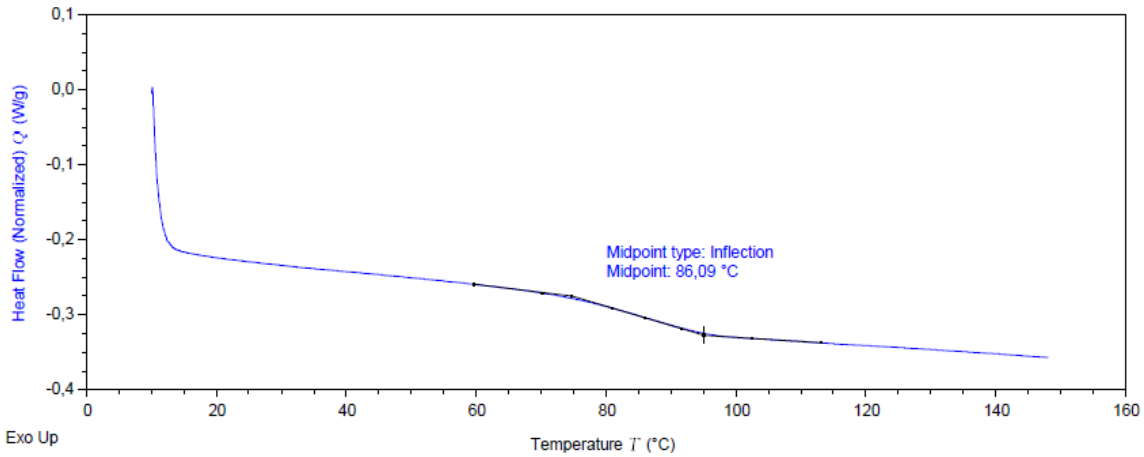

Fig. 48: DSC curve of Dentacryl resin with mixing ratio 1:1, the inflection point is highlighted in the diagram and T_g is determined for 86 °C

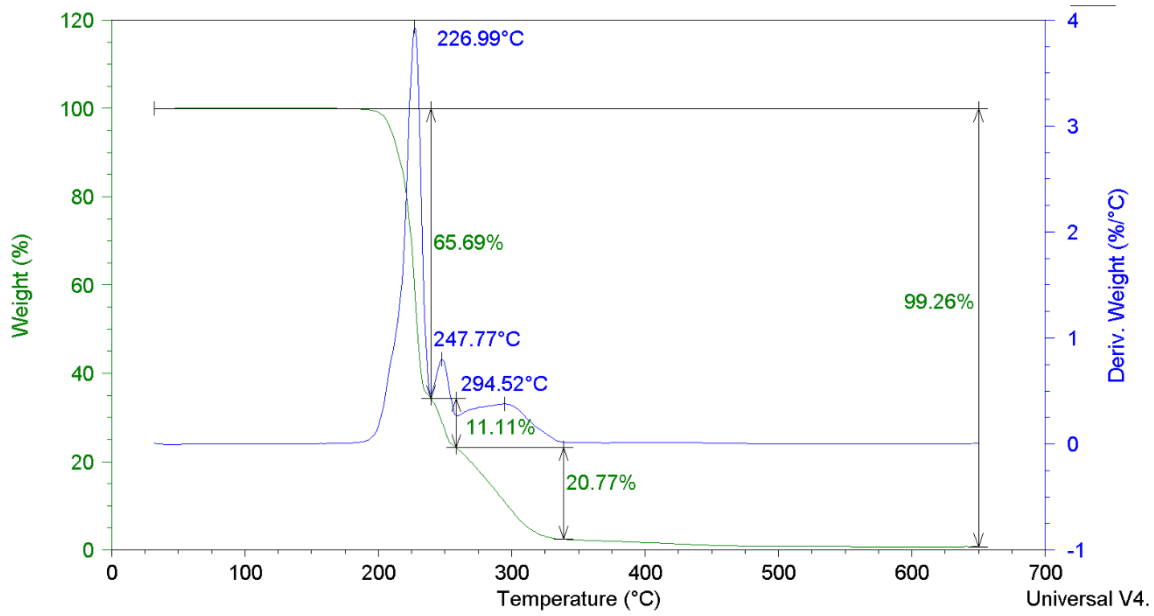

Fig. 49: TGA curve of pure azodicarbonamide (UNICELL D 200 A) with distinguished steps of decomposition

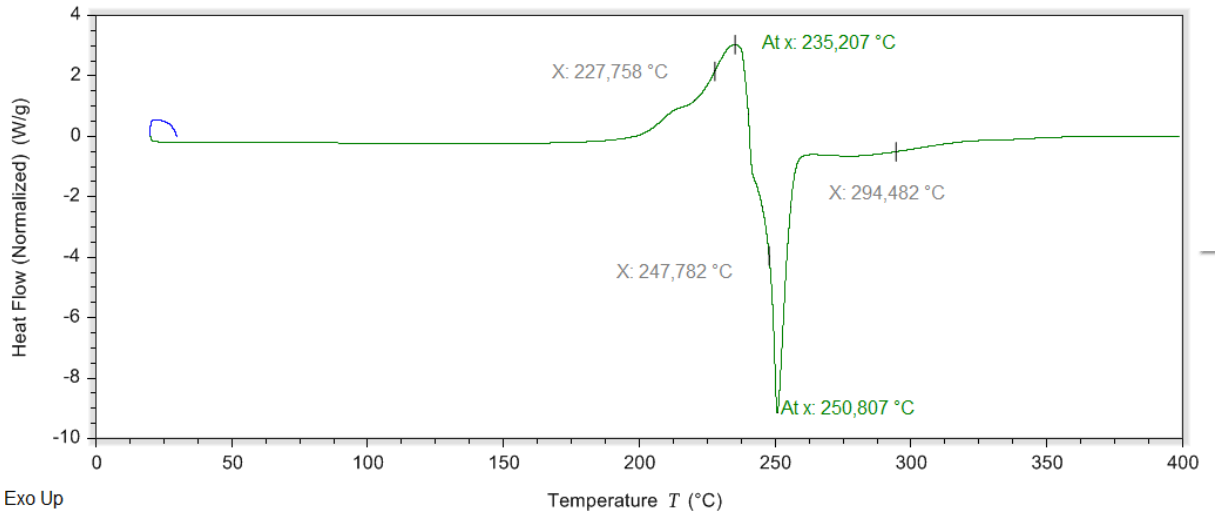

Fig. 50: DSC curve of azodicarbonamide (UNICELL D 200 A) where endothermic peak shows melting temperature at 235 °C

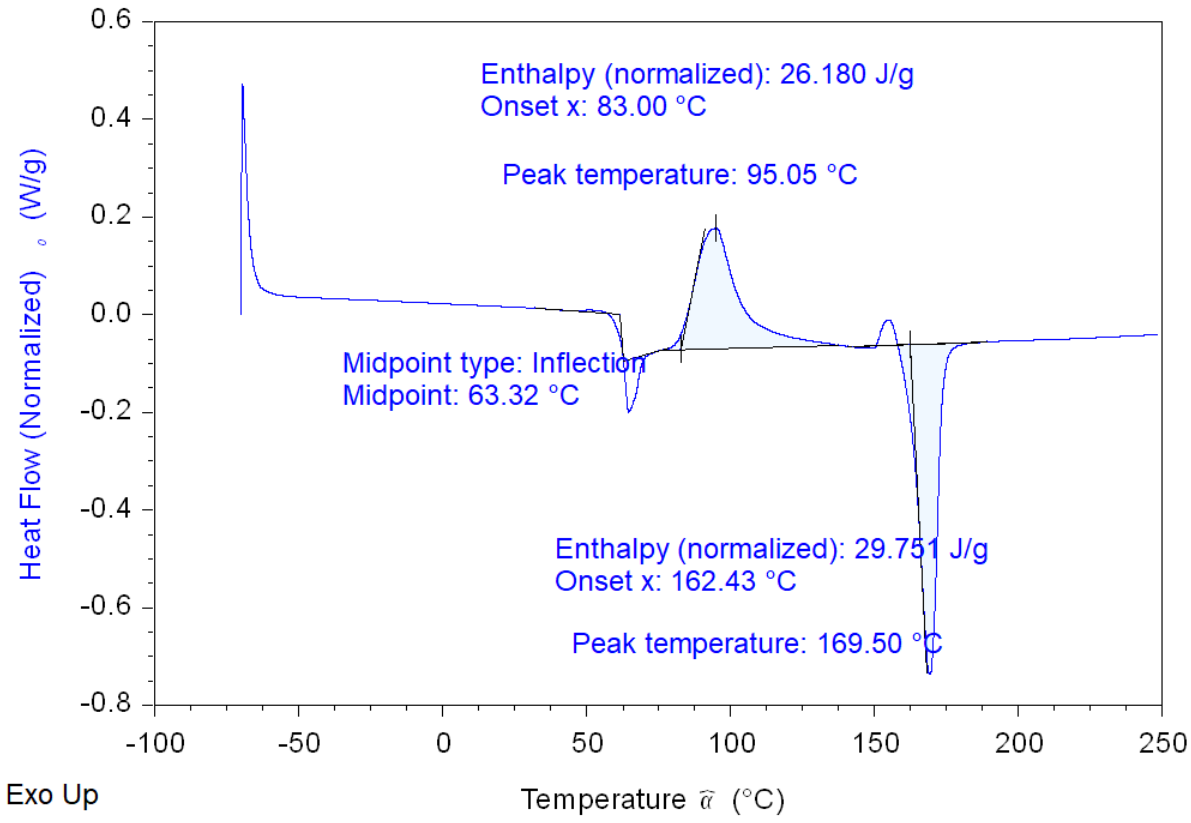

Fig. 51: DSC of PLA filament – 1st heating; DSC

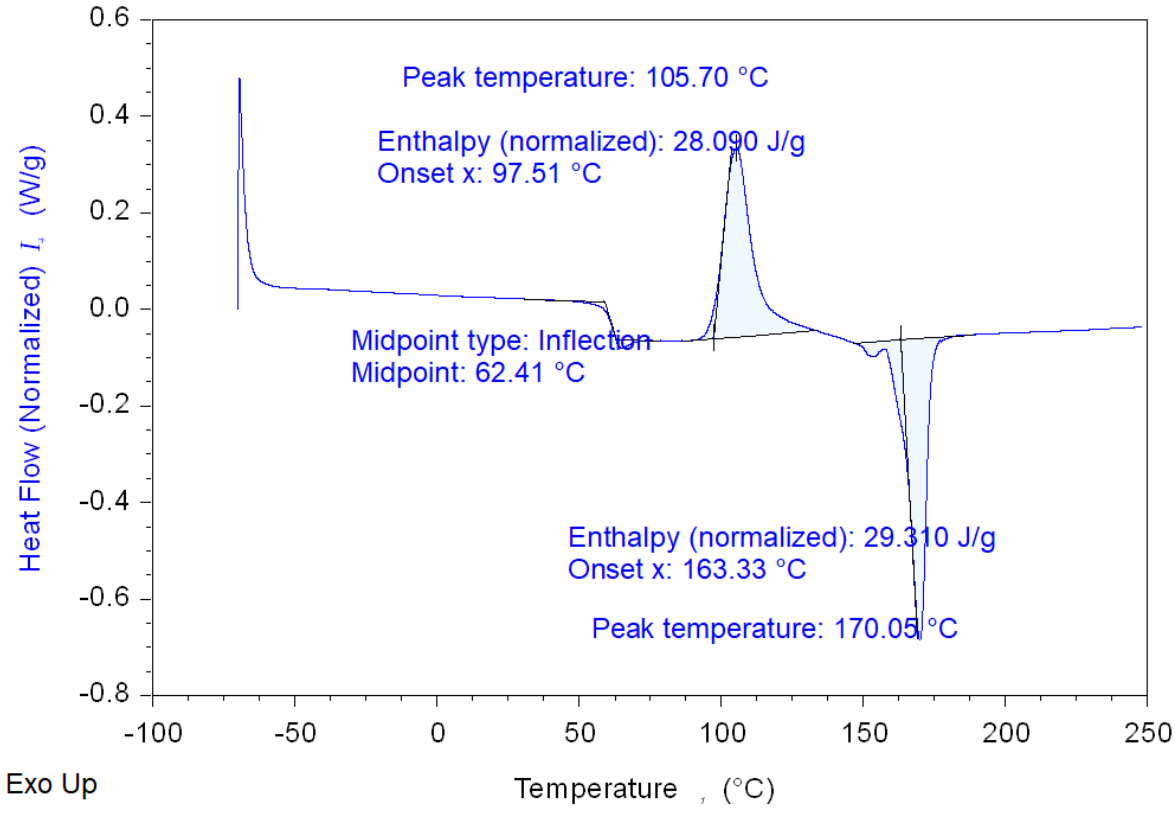

Fig. 52: DSC of PLA filament – 2nd heating; DSC

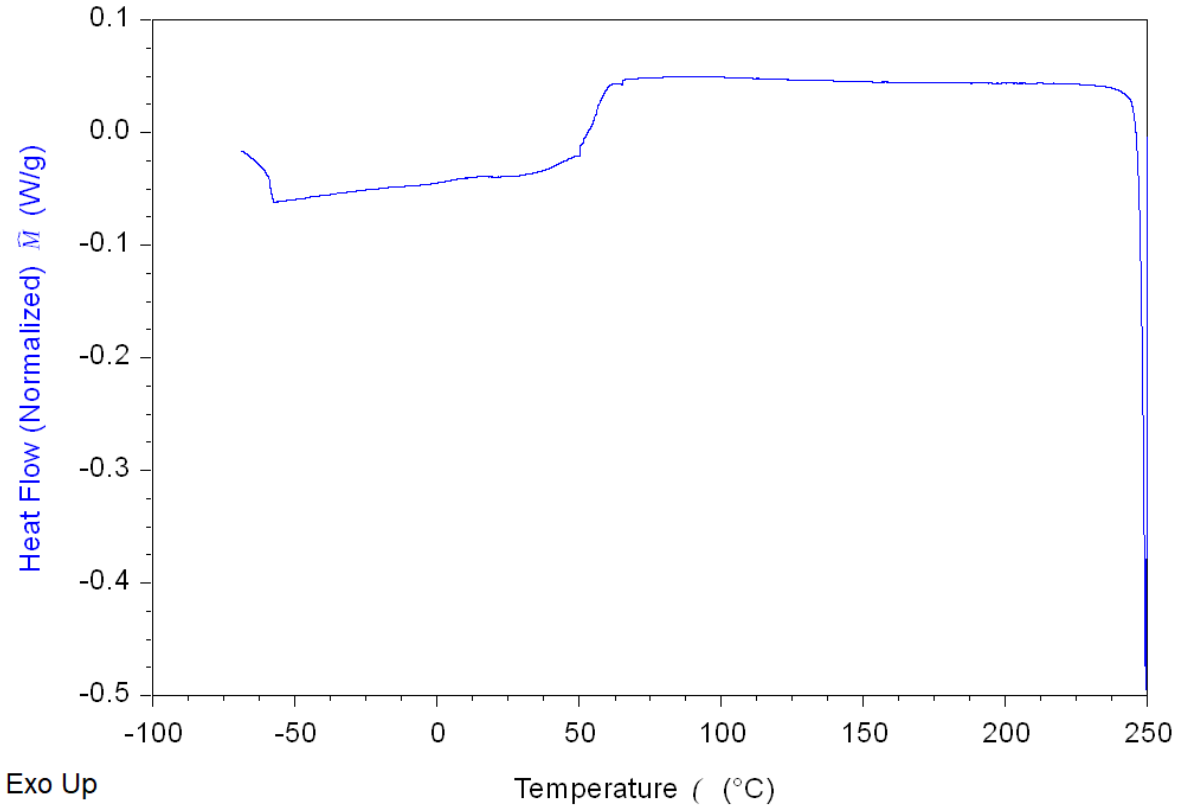

Fig. 53: DSC of PLA filament – cooling; DSC

Table 7: Various measured values for the samples prepared by the layer-by-layer technique – ρ is the density, ρ^* is the relative density, E is the Young´s modulus, E_a is the averaged Young´s modulus, σ_c is the compressive strength, $\sigma_{c,a}$ is the averaged compressive strength, E^*_t is the relative Young´s modulus calculated from the Gibson-Ashby model, E^* is the relative Young´s modulus calculated from the measured values, σ_s is the compressive strength of the solid, and under the index t are values calculated from the Gibson-Ashby model

	ρ [g·cm^{-3}]	ρ^* [g·cm^{-3}]	E [MPa]	E_a [MPa]	σ_c [MPa]	$\sigma_{c,a}$ [MPa]	E^*_t []	E^* []	$(\sigma_m/\sigma_s)_t$ []	σ_m/σ_s []
1 %	0,1198	0,1165	21,196 18,353 17,282	18,944	8,752 8,394 8,796	8,647	0,01357	0,01987	0,0119	0,0773
3 %	0,0819	0,0796	12,825 7,809 9,539	10,058	6,728 6,334 6,776	6,612	0,00634	0,01055	0,0067	0,0591
5 %	0,0645	0,0627	4,256 3,928 4,727	4,304	5,893 6,107 5,957	5,986	0,00393	0,00451	0,0047	0,0535
Gradient	0,0998	0,0971	8,297 8,279 8,092	8,223	6,511 6,511 6,637	6,553	-	0,00863	-	0,0586
solid PMMA	1,0283	-	845,971 967,219 1046,395	953,195	111,996 112,168 111,299	111,821	-	-	-	-

Table 8: Various measured values of the 3D samples without the notch - ρ is the density, ρ^* is the relative density, E_f is the Young´s modulus, σ_{fY} is the bending strength, $(E_f/E_s)_t$ is the relative Young´s modulus, $(\sigma_{fY}/\sigma_{sY})$is the relative bending strength, index a are averaged values, index t are values calculated using Gibson-Ashby theoretical models, index s are values of the solid

	sample	ρ [g·cm^{-3}]	ρ_a [g·cm^{-3}]	ρ^* []	$(E_f/E_s)_t$ []	$(\sigma_{fY}/\sigma_{sY})_t$ []	E_f [MPa]	$E_{f,a}$ [MPa]	σ_{fY} [MPa]	$\sigma_{fY,a}$ [MPa]	E_f/E_s []	σ_{fY}/σ_{sY} []
solid	1	1,121	1,111	-	-	-	2494,76	2433,39	74,016	74,040	-	-
	2	1,100					2310,56		73,726			
	3	1,110					2494,86		74,379			
Gradient 1	1	0,860	0,887	0,7985	-	-	2102,61	2128,47	21,458	21,001	0,8747	0,2836
	2	0,887					2198,23		21,660			
	3	0,914					2084,57		19,887			
Gradient 2	1	0,768	0,773	0,6962	-	-	2179,35	2098,47	13,512	12,523	0,8624	0,1691
	2	0,802					2120,93		12,646			
	3	0,749					1995,14		11,410			
Gradient 3	1	0,862	0,875	0,7875	-	-	2271,10	2320,20	19,793	21,068	0,9535	0,2846
	2	0,882					2304,94		21,776			
	3	0,880					2384,56		21,636			
Infill 80%	1	1,034	1,023	0,9208	0,8479	0,1591	2405,09	2338,83	59,744	60,094	0,9611	0,8116
	2	1,007					2295,10		60,147			
	3	1,027					2316,31		60,390			
Infill 60%	1	0,917	0,916	0,8246	0,6799	0,1348	2047,27	2029,74	50,914	50,510	0,8341	0,6822
	2	0,909					2060,45		50,795			
	3	0,921					1981,49		49,821			
Infill 40%	1	0,844	0,842	0,7578	0,5742	0,1187	1921,77	1940,33	49,650	49,710	0,7974	0,6714
	2	0,849					2010,54		50,112			
	3	0,832					1888,68		49,369			
Infill 20%	1	0,708	0,722	0,6501	0,4226	0,0943	1824,180	1889,21	45,32	44,376	0,7764	0,5993
	2	0,726					1902,271		44,72			
	3	0,731					1941,181		43,09			

Table 9: Various measured values of the 3D samples with the notch - ρ is the density, ρ^* is the relative density, E_f is the Young´s modulus, σ_{fY} is the bending strength, $(E_f/E_s)_t$ is the relative Young´s modulus, $(\sigma_{fY}/\sigma_{sY})$is the relative bending strength, index a are averaged values, index t are values calculated using Gibson-Ashby theoretical models, index s are values of the solid

	sample	ρ [g·cm^{-3}]	ρ^* []	$(E_f/E_s)_t$ []	$(\sigma_{fY}/\sigma_{sY})_t$ []	E_f [MPa]	$E_{f,a}$ [MPa]	σ_{fY} [MPa]	$\sigma_{fY,a}$ [MPa]	E_f/E_s []	σ_{fY}/σ_{sY} []
solid	1	1,111	-	-	-	1743,748	1699,745	25,705	25,967	-	-
	2					1746,980		26,277			
	3					1608,506		25,921			
Gradient 1	1	0,887	0,7985	-	-	1147,553	1171,250	9,186	9,756	0,6891	0,3757
	2					1132,003		9,626			
	3					1234,194		10,457			
Gradient 2	1	0,773	0,6962	-	-	836,333	859,684	8,677	9,000	0,5058	0,3466
	2					835,754		8,678			
	3					906,964		9,646			
Gradient 3	1	0,875	0,7875	-	-	1202,470	1209,594	9,698	10,530	0,7116	0,4055
	2					1186,988		9,612			
	3					1239,324		12,278			
Infill 80%	1	1,023	0,9208	0,8479	0,1591	1609,378	1542,409	20,948	20,928	0,9074	0,8059
	2					1476,704		19,925			
	3					1541,145		21,911			
Infill 60%	1	0,916	0,8246	0,6799	0,1348	1443,010	1497,453	16,880	16,941	0,8810	0,6524
	2					1499,937		16,758			
	3					1549,412		17,186			
Infill 40%	1	0,842	0,7578	0,5742	0,1187	1385,324	1344,121	15,816	15,392	0,7908	0,5928
	2					1378,675		15,590			
	3					1268,363		14,771			
Infill 20%	1	0,722	0,6501	0,4226	0,0943	1242,399	1250,034	15,364	15,188	0,7354	0,5849
	2					1219,439		14,445			
	3					1288,263		15,754			

Table 10: The results of the fracture toughness of the 3D printed samples tested with the notch – σ_{fs} is the stress at the rupture, K^*_{IC} is the fracture toughness, l is the size of the cell, index t are values calculated using Gibson-Ashby theoretical model

	sample	σ_{fs} [MPa]	K^*_{IC} [MPa·m$^{1/2}$]	$K^*_{IC}/(\sigma_{fs}\cdot\sqrt{\pi l})$ []	$K^*_{IC}/(\sigma_{fs}\cdot\sqrt{\pi l})_t$ []
solid	1 2 3	5,420	0,5764	-	-
Gradient 1	1 2 3	2,986	0,3176	1,6732	-
Gradient 2	1 2 3	2,638	0,2806	1,2659	-
Gradient 3	1 2 3	3,361	0,3574	2,0336	-
Infill 80%	1 2 3	3,957	0,4208	2,6833	0,5743
Infill 60%	1 2 3	3,419	0,3636	1,8974	0,5696
Infill 40%	1 2 3	2,648	0,2816	1,3416	0,5018
Infill 20%	1 2 3	4,129	0,4391	0,9487	0,3987

Table 11: The values of the cells´ sizes of the gradient structures – l is the cell size, Gradient 1, 2, and 3 are the number of the cells, l_a is the weight average of the cells´ sizes

l [mm]	0,25	0,5	0,75	1	1,5	l_a [mm]
Gradient 1	86	10		18		0,3904
Gradient 2	42	13		18	4	0,5325
Gradient 3	90	24	6		1	0,3347